THE UNIVERSITY OF CHICAGO

TESTS OF LORENTZ INVARIANCE AT THE SUDBURY NEUTRINO OBSERVATORY

A DISSERTATION SUBMITTED TO
THE FACULTY OF THE DIVISION OF THE PHYSICAL SCIENCES
IN CANDIDACY FOR THE DEGREE OF
DOCTOR OF PHILOSOPHY

DEPARTMENT OF PHYSICS

BY
KEVIN RUSSELL LABE

CHICAGO, ILLINOIS
DECEMBER 2017

To my parents

Truth is wrought out by many minds working together freely

J H Newman

TABLE OF CONTENTS

LIST OF FIGURES

LIST OF TABLES

ACKNOWLEDGMENTS

The research reflected in this dissertation was partially supported by the Graduate Assistance in Areas of National Need program, by a SNO analysis fellowship, and by the National Science Foundation. Many thanks to the wider SNO and SNO+ collaborations without whom this project could not have come to fruition.

ABSTRACT

Lorentz symmetry is among the most fundamental assumptions in physics. Experimental tests that this symmetry is respected in systems of all types are therefore critically important. Seven years of data from the Sudbury Neutrino Observatory, a kiloton-scale heavy water Cerenkov detector, are analyzed for possible violations of Lorentz symmetry in the neutrino sector. Such violations would appear as one of eight possible signal types in the detector: six seasonal variations in the solar electron neutrino survival probability with different energy and time dependences, and two shape changes to the oscillated energy spectrum. No evidence for such signals is observed, and limits on the size of such effects are established in the framework of the Standard Model Extension, including 40 limits on previously unconstrained operators and improved limits on 15 additional parameters. Limits on all leading-order operators in the neutrino sector are now available for the first time.

CHAPTER 1

INTRODUCTION

Central to physics as a discipline is the description of symmetries in nature and their consequences in conservation laws. The justly celebrated Noether theorem formalizes this connection. Perhaps the most fundamental such symmetry is Lorentz symmetry, which reflects the inertial frame invariance of natural law, the fact that physics is the same in all directions and at all relative velocities. Lorentz symmetry undergirds the conservation of angular momentum. The mathematical representation of Lorentz symmetry was developed as part of relativistic mechanics in the early twentieth century and has since become a foundational assumption in many areas of physics, including quantum field theories. Nevertheless, the reality of this symmetry is an experimental question accessible to experimental tests. It is precisely because of its foundational importance that this assumption should be tested as carefully as possible. This thesis describes such a test in the neutrino sector.

Although it is clear from its great success in many areas that Lorentz symmetry is at least approximately respected, the same could have been said in the past for many other symmetries that were subsequently found to be broken. In fact, history has shown that most of the symmetries of nature that have been considered fundamental are in fact merely approximately respected under the most general conditions. The first such example was the unraveling of Galilean symmetry in the era around 1900 and its eventual replacement with Lorentz symmetry. Maxwell's development of a unified theory of electromagnetism [1] prompted a search for the so-called luminiferous aether that was then thought to permeate the vacuum to support electromagnetic waves. Michelson's famous null result [2] in searching for the aether wind exacerbated existing problems in trying to understand the application of frame invariance to electromagnetic phenomena. Several physicists, including Larmor [3] and Poincaré [4], were working on resolving these contradictions in the 1890s and 1900s. They partially anticipated the result first presented by Lorentz in 1904 [5] that restored frame invariance to electromagnetism through the introduction of a new set of frame transforma-

tions. This was later provided with a firm conceptual interpretation in relativistic mechanics by Einstein in 1905 [6].

There are also important examples of this pattern in the history of the discrete symmetries of particle physics: charge conjugation (C), parity (P), and time reversal (T). These were originally believed to be separately conserved, until the discovery in the 1950s by Dalitz of apparently identical particles that could decay to parity odd or to parity even states, later understood as two decay modes of the kaon [7]. This led to the realization by Lee and Yang [8] in 1956 that there was no evidence to support the conservation of parity by the weak force, since only parity-invariant quantities had been investigated. They suggested a test to search for a coupling of a nuclear spin to the beta momentum, since unlike momenta, spins are unchanged by parity. This suggestion was quickly followed by a number of groups, first by Wu in 1957, who observed parity violation in the decay of spin-polarized ^{60}Co [9]. The combined CP symmetry was then believed to be conserved until the observation of the CP violating decay $K_2^0 \to \pi^+\pi^-$ in 1964 [10]. The violation of these discrete symmetries are particularly relevant to tests of Lorentz symmetry, since any violation of CPT symmetry would imply a violation of Lorentz symmetry as well (although Lorentz invariance violations are a more general class of possibilities) [11].

Violations of Lorentz invariance are expected in many high-energy theories, including string theory, noncommutative field theories, random dynamics, and other approaches to quantum gravity [12]. A test of Lorentz symmetry like the one described in this dissertation can serve two purposes. Should a violation be observed, it would be a critically important clue toward the physics that lies beyond the Standard Model. Should no violation be observed, it provides a constraint on the same kinds of models.

When exploring these non-standard effects, a consistent phenomenological framework provides an invaluable utility. In this study, that role is filled by the so-called Standard Model Extension (SME) [13, 14], which classifies all possible violations of Lorentz symmetry in particle physics subject to certain desiderata which will be discussed in detail in Chapter

3. This framework includes a very large number of independent Lorentz symmetry violating operators, each controlled by a separate coefficient governing the strength of the violation. In general, these can vary according to the particle species involved, the spatial direction selected, and the particular effect observed. Separate tests must be carried out to look for each of these effects individually. Some effects, particularly in the photon sector, have been studied to extreme precision, while others have not been studied at all. Among those effects heretofore poorly tested are some of those in the neutrino sector. The extremely weak interactions of neutrinos make such tests challenging, but their tiny masses make them excellent probes of such effects.

The conceptual basis of the test described here is quite similar to the test for the aether wind carried out by Michelson. The idea is to leverage the non-inertial orbital motion of the Earth to look for variations in particle behavior at different times of year. The neutrinos studied in this analysis originated in the Sun, which generates an enormous flux of neutrinos through its nuclear reactions. These solar neutrinos were detected in an experiment called the Sudbury Neutrino Observatory (SNO) [15], which is discussed in detail in Chapter 4. As the Earth orbits the Sun, the direction of propagation of solar neutrinos reaching the Earth varies in the inertial frame of the Sun. Thus if there were direction-dependent effects on the propagation of neutrinos, this would be detected as annual variations in the behavior of neutrinos detected in SNO. We derive the specific form of this signal in Chapter 5. The practical details of the analysis are discussed in Chapter 6, and the results presented in Chapter 7. Chapter 8 concludes.

CHAPTER 2

NEUTRINO PHYSICS

Neutrinos are electrically neutral fundamental particles. They arise most commonly as a byproduct of nuclear beta decay, in which a neutron decays into a proton, an electron, and a neutrino. The neutrino interacts so weakly that it was not observed in early studies of beta decay. This made it appear that conservation of energy was being violated, since the energy carried off by the neutrino was not being accounted for. Pauli predicted the existence of the neutrino as a solution to this problem in 1930 [16]. Direct observation of the neutrino was not achieved until 1956 when Reines and Cowan used recently developed nuclear reactors as an intense neutrino source [17]. Neutrinos are produced in coincidence with charged leptons (for example, electrons in beta decay), which allows their "flavor" to be tagged. It is now known that there are three distinct neutrino flavors (electron, muon, and tau), one corresponding to each of the charged leptons [18].

The correct fermion model describing neutrinos remains unknown. Pauli originally assumed that the neutrino was massless since no kinematic effects were visible in the beta decay spectrum. We now know from experiments including SNO that they are massive, albeit with unknown and very tiny masses (at least five orders of magnitude smaller than the electron [19]). There are two possible descriptions of massive fermions, known after their originators as Dirac and Majorana fermions. Only neutral particles can be described as Majorana fermions, since such states are preserved under charge conjugation. Dirac and Majorana fermions would obtain their masses through quite different means, with Dirac masses coming from the Higgs mechanism, while Majorana masses result from higher-dimension operators [20]. This explains in part why neutrinos are particularly attractive as probes of Lorentz symmetry violations. Lorentz violations would likely derive from new physics at high energy scales, and are therefore suppressed relative to known physics at electroweak scales. However, in the neutrino sector, it may be that the only known physics with which Lorentz violations would have to compete likewise derive from physics at high energy scales, and

could therefore plausibly appear at a similar level.

The search for evidence of Majorana neutrinos has led to a broad program of experiments trying to observe neutrinoless double beta decay (one of the experimental signatures of Majorana masses), including the SNO+ experiment that is a successor to the SNO experiment described herein. However, for the purposes of understanding the leading-order interactions of the neutrino, the distinction between Dirac and Majorana neutrinos is irrelevant because of the chiral nature of the weak interaction.

2.1 Neutrino Interactions

The interactions of neutrinos are described as part of the Standard Model of particle physics, a quantum field theory with its field content and allowed interactions specified to be consistent with all available evidence about the behavior of fundamental particles. The fields of the Standard Model, shown in Figure 2.1, are categorized into three types: quarks, leptons, and gauge bosons. Quarks and leptons are fermions, the matter content of the model. There are three generations of these fermions, which are identical in all respects apart from their masses. In addition to the matter fields there are the $W^{\pm}$ and Z bosons which mediate weak nuclear forces, the photon which mediates the electromagnetic force, gluons which mediate strong nuclear forces, and the Higgs boson, which gives rise to fundamental masses through its interactions.

The coupling of these forces to the matter fields are governed by charges: the electrical charge for the electromagnetic force, the weak charge for the weak nuclear forces, and color charges for the strong nuclear force. Neutrinos are electrically neutral and colorless, and therefore couple to other forms of matter only through the weak interaction. For the energies relevant at SNO (notably below the muon mass), neutrinos can interact in three distinct ways: scattering off an electron (Figure 2.2), or undergoing an interaction with a nucleon, which can be mediated by either a charged current or a neutral current (Figure 2.3).

Although neutrinos are observed in the flavor basis, there is no reason that these states

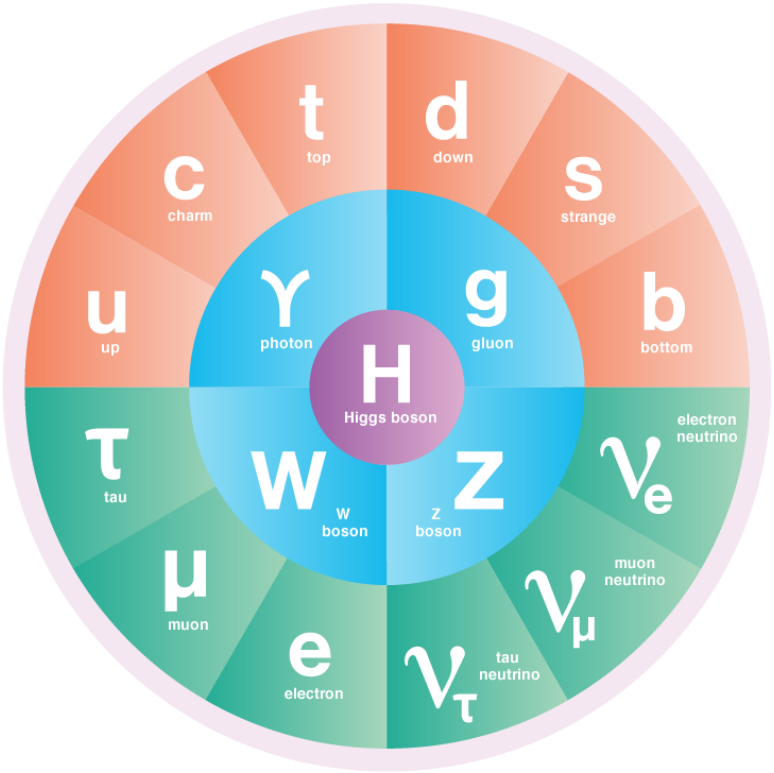

Figure 2.1: Particle content of the standard model. The quarks are shown in orange, the leptons in green, the gauge bosons in blue, and the Higgs in purple [21].

Figure 2.2: Two contributions to the elastic scattering of an electron by a neutrino. Because the diagram on the left exists only for ν_e while the diagram on the right is flavor-agnostic, this interaction is sensitive to a different linear combination of flavor content than either the charged or neutral current interactions.

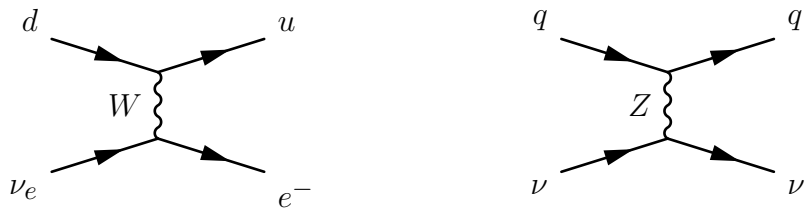

Figure 2.3: (left) Charged current interaction, accessible only to electron neutrinos at the energies of solar neutrinos; (right) Neutral current interaction.

must be energy eigenstates of the neutrino system. Indeed, it turns out that under ordinary circumstances, the flavor states are not eigenstates of motion. This results in the phenomenon known as *neutrino oscillation*, in which neutrinos initially produced in one flavor state may be observed in a different flavor state at a later time.

The neutrino Hamiltonian is given by

$$H = \frac{1}{2E}(M^2 + A)\,, \tag{2.1}$$

where M is the mass matrix of the neutrinos (which in general can contain a combination of both Dirac and Majorana masses) and A is an effective potential due to interactions of the neutrinos with matter. The matrix M in general need not be diagonal in the flavor basis, and indeed it is not, just like in the case of the quark sector. It is diagonalized by a matrix U called the Pontecorvo-Maki-Nakagawa-Sakata (PMNS) matrix [22, 23], which is typically parameterized [19] in terms of three mixing angles and a complex phase δ as:

$$U = \begin{pmatrix} c_{12}c_{13} & s_{12}c_{13} & s_{13}e^{-i\delta} \\ -s_{12}c_{23} - c_{12}s_{23}s_{13}e^{i\delta} & c_{12}c_{23} - s_{12}s_{23}s_{13}e^{i\delta} & s_{23}c_{13} \\ s_{12}s_{23} - c_{12}c_{23}s_{13}e^{i\delta} & c_{12}s_{23} - s_{12}s_{23} - s_{12}c_{23}s_{13}e^{i\delta} & c_{23}c_{13} \end{pmatrix}. \tag{2.2}$$

(Here $c_{ij} \equiv \cos\theta_{ij}$ and $s_{ij} \equiv \sin\theta_{ij}$.) Nonzero δ would lead to CP violation in the neutrino sector, but its value is currently unknown. The truly complete form of the PMNS matrix also includes two Majorana phases; however, these do not enter into the physics of any existing or projected experiment. We will discuss the origin and impact of the potential term in more detail in the next section, focusing here on the behavior in vacuum.

The nondiagonal form of the Hamiltonian gives rise to a time dependence in the neutrino flavor state, called an oscillation because the flavor fractions change back and forth in time. The physics of oscillation in the simplest case of a two-flavor system in a vacuum can be easily understood, and the more realistic cases are merely variations on the same idea. Suppose

we begin with a neutrino in the electron flavor, $|\nu_e\rangle$. We can time-evolve this state easily if we rewrite it in the energy basis. In a two-state system, unitarity guarantees that we can write any state as $|\psi\rangle = \sin\theta\,|E_1\rangle + \cos\theta\,|E_2\rangle$ for some choice of θ. We can therefore write:

$$\begin{aligned} |\nu(t)\rangle &= \sum_n e^{-iE_n t/\hbar}\,|\nu_n(0)\rangle \\ &= \sin\theta e^{-iE_1 t/\hbar}\,|\nu_1\rangle + \cos\theta e^{-iE_2 t/\hbar}\,|\nu_2\rangle\ . \end{aligned} \tag{2.3}$$

Since neutrinos have such small masses, they are usually found in ultrarelativistic states, in which the energies can be estimated to be $E_n = \sqrt{p^2 + m_n^2} \approx p + m_n^2/2E$. Substituting this and factoring out the common phase $e^{-ipt/\hbar}$, we have

$$|\nu(t)\rangle = \sin\theta e^{-im_1^2 t/2E\hbar}\,|\nu_1\rangle + \cos\theta e^{-im_2^2 t/2E\hbar}\,|\nu_2\rangle\ . \tag{2.4}$$

The "survival probability" P of finding the neutrino in the electron state at a later time is therefore

$$\begin{aligned} P = |\langle\nu_e|\nu(t)\rangle|^2 &= \left|\sin^2\theta e^{-im_1^2 t/2E\hbar} + \cos^2\theta e^{-im_2^2 t/2E\hbar}\right|^2 \\ &= 1 - \sin^2 2\theta \sin^2(\Delta m_{12}^2 t/4E\hbar)\,. \end{aligned} \tag{2.5}$$

We can rewrite this in a more concrete form by noting that $t = L/c$ for a realistic neutrino, and plugging in the constants to find

$$P = 1 - \sin^2 2\theta \sin^2\left(1.27\frac{\Delta m_{12}^2[\mathrm{eV}^2]L[\mathrm{km}]}{E[\mathrm{GeV}]}\right)\ . \tag{2.6}$$

From this, one can see that the experimentally accessible quantities are the mixing angles and the mass-squared differences. In a typical experiment the distance to the source L is fixed and the parameters are fit as a function of the neutrino energy. The quantity $4\pi E/\Delta m^2$ is called the oscillation length since it determines the representative distance scale over which flavor changes can be observed.

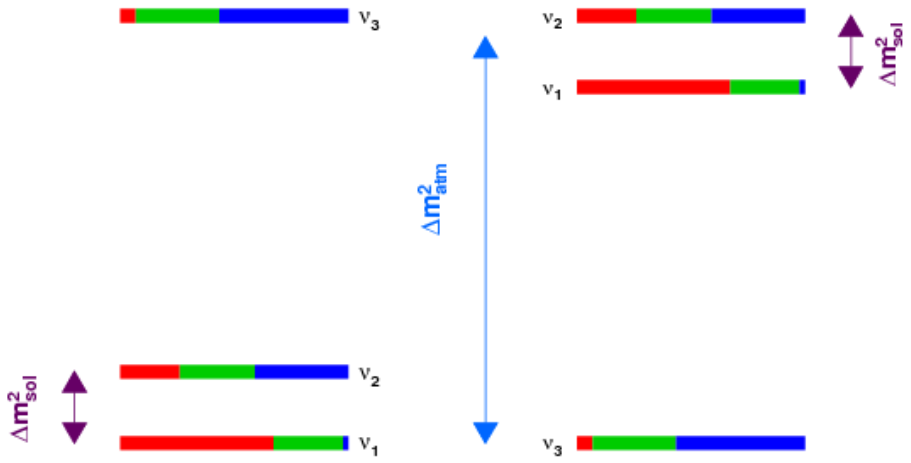

Figure 2.4: Flavor content of the neutrino mass states [24]. The normal hierarchy is shown on the left, and the inverted hierarchy on the right. Red is electron flavor, green muon flavor, and blue tau flavor.

Since only the mass squared differences appear in the survival probability, the masses themselves and the matrix M remain completely unknown. We do not even know whether $m_3 > m_1$ or vice versa. These two possibilities are called the normal and inverted mass hierarchy, respectively, by analogy with the situation in the charged lepton sector. In contrast, the diagonalizing matrix U is known to reasonable precision thanks to a widespread program over the last twenty years to determine these mixing parameters. The mixing matrix can be visualized in terms of the flavor content of the various mass states. This is illustrated in Figure 2.4.

Because of the large separation of scales between the two mass squared splittings, it has largely been possible to measure these parameters individually in different systems. The parameters have therefore acquired names indicating the system in which they were first measured. θ_{12} (the "solar angle") and Δm^2_{21} have been measured through the study of solar neutrinos in heavy water (by SNO), in light water (by Super Kamiokande [25]), and in scintillator (by KamLAND [26]). θ_{13} (the "reactor angle") has been measured through the study of reactor neutrinos by Daya Bay [27], Double Chooz [28], and RENO [29]. θ_{23}

Quantity	Normal Hierarchy		Inverted Hierarchy	
	Best Fit	3σ range	Best Fit	3σ range
Δm^2_{21} (10^{-5} eV^2)	7.37	6.93 - 7.97	7.37	6.93 - 7.97
Δm^2_{23} (10^{-3} eV^2)	2.50	2.37 - 2.63	2.46	2.33 - 2.60
$\sin^2\theta_{12}$	0.297	0.250 - 0.354	0.297	0.250 - 0.354
$\sin^2\theta_{23}$	0.437	0.379 - 0.616	0.569	0.383 - 0.637
$\sin^2\theta_{13}$	0.0214	0.0185 - 0.0246	0.0218	0.0186 - 0.0248
δ	1.35π	0 - 2π	1.32π	0 - 2π

Table 2.1: Current knowledge of neutrino mixing parameters based on a simultaneous fit of all available data [19]. It is not known whether the mass hierarchy is normal or inverted.

(the "atmospheric angle") has been measured through the study of atmospheric neutrinos (by IceCube [30]), accelerator neutrinos (by NOνA [31] and T2K [32]) or both (by MINOS [33]). Reactor, accelerator, and atmospheric experiments all have sensitivity to the remaining parameter, Δm^2_{32}. The results from all of these experiments can be combined into a global analysis [34] to produce the best understanding of the mixing parameters. These results are summarized in Table 2.1.

2.2 Solar Neutrino Oscillations

The neutrinos studied in SNO originate in the Sun, and a number of special features are relevant to understanding this system, which we discuss here. The Sun is powered by nuclear reactions that produce electron neutrinos as a byproduct. There are several different sources of solar neutrinos, classified according to their parent nucleus, which differ in their energy distributions. These include both broadband and line sources with energies generally between 0.1 and 20 MeV. The composite solar neutrino spectrum is shown in Figure 2.5. Because SNO could only reliably detect neutrinos with energies of at least 3.5 MeV, the only solar neutrino source of relevance for this analysis is the ^{8}B neutrino, which has a broad spectrum of up to 12 MeV. (SNO was also sensitive to higher-energy *hep* neutrinos, but these have such a small flux that they could not be unambiguously identified in SNO [35]).

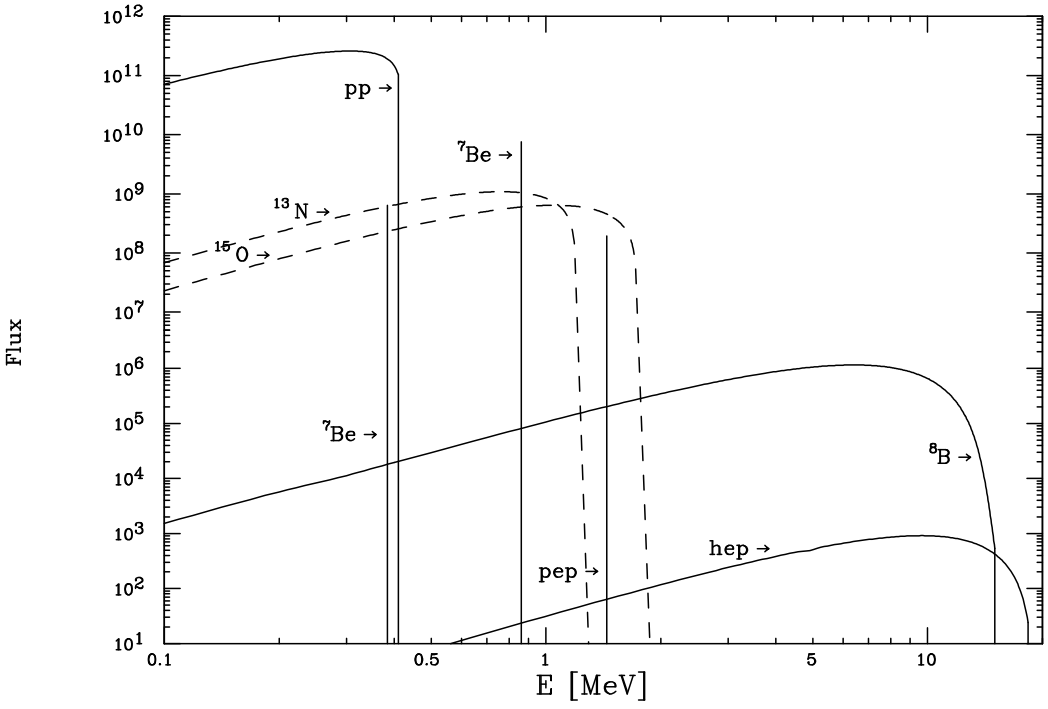

Figure 2.5: Energy spectrum of solar neutrinos. Figure from reference [36].

The solar neutrino spectrum and fluxes can be estimated from the Standard Solar Model that describes the workings of the Sun [37]. These estimates have been broadly supported by measurements from SNO and Borexino [38]. In this analysis we do not make assumptions about the normalization of the solar neutrino flux, although we do use the well-established shape of the ^{8}B energy spectrum (which is just the complement of the β spectrum of ^{8}B).

Solar neutrinos are among the more complicated neutrino systems to be experimentally probed and do not obey the straightforward vacuum oscillation equation derived above. In fact, contrary to popular belief, solar neutrinos do not oscillate during their propagation between the Sun and the Earth, but instead are adiabatically converted from an electron flavor state into a mass state as they pass out of the Sun due to the Mikheyev-Smirnov-Wolfenstein (MSW or matter) effect [39, 40]. We will here discuss the physics of this process.

Coherent forward scattering of neutrinos by electrons introduces a term in the neutrino Hamiltonian that depends on the local electron number density. The fact that a scattering process can give rise to a local property (a potential) is entirely analogous to an optical index of refraction. In both cases, scattering in a medium causes the wavepacket to accumulate an additional phase [7] in proportion to the distance d it traverses in the medium and its wavenumber k:

$$\Delta\Psi = k(n-1)d\,. \tag{2.7}$$

In optics, such an effect is typically described as a refractive index n, which can be expressed [41] as a function of the forward scattering amplitude $f(0)$ as

$$n = 1 + \frac{2\pi}{E^2} N_e f(0)\,, \tag{2.8}$$

where N_e is the number density of scatterers (electrons in this case). For charged current electron-neutrino scattering, $f(0) = G_F E/\sqrt{2}\pi$. In principle, there is a similar effect arising from the scattering of neutrinos of all flavors off of neutrons, but since this is flavor-independent, it has no effect on the dynamics of neutrino mixing and can be neglected.

Since we are more interested in a Hamiltonian approach to the problem, it is more convenient to interpret the additional phase as an effective potential. It is easy to see that since $k \propto p \approx E$ for ultrarelativistic neutrinos, this scattering phase is equivalent to changing the Hamiltonian by a potential of the form

$$V = E(n-1) = \sqrt{2} N_e G_F \,. \tag{2.9}$$

From the definition of A in the Hamiltonian (equation 2.1), we then see that $A = 2EV = 2\sqrt{2} E G_F N_e$. Although G_F is very small, this term can still have an impact because the mass squared values of the neutrinos are also very small. In fact, this matter effect dominates solar neutrino oscillations in certain energy regimes.

The presence of this matter potential causes the energy eigenstates within the Sun to differ from the vacuum eigenstates. Since computations are typically done in terms of mixing angles, it is useful to define matter-perturbed mixing angles. For a two-flavor system, this can be defined [20]

$$\sin^2 \theta_m = \frac{1}{2} + \frac{-\Delta m^2 \cos 2\theta + A}{2\sqrt{\left(\Delta m^2\right)^2 - 2\Delta m^2 A \cos 2\theta + A^2}} \,. \tag{2.10}$$

There is likewise a matter-perturbed mass-splitting,

$$\Delta m^2_m = \sqrt{\left(\Delta m^2 \cos 2\theta - A\right)^2 + \left(\Delta m^2 \sin 2\theta\right)^2} \,. \tag{2.11}$$

In a completely general three-flavor model, these matter-perturbed quantities become extremely complicated, but thankfully the scale separation between the different neutrinos means that for solar neutrinos, to first order the above expressions apply with the matter potential reduced by a factor $\cos^2 \theta_{13}$, or about 2% [20]. We will discuss a more detailed approach below.

Now that we have introduced the necessary concepts connected to the matter effect, we

can return to our discussion of the dynamics of solar neutrinos. Neutrinos are produced in nuclear reactions in the Sun exclusively in the electron flavor state; however, its projection onto mass states is different deep within the Sun because of the high electron density. In the case of ^{8}B neutrinos, it just so happens that the electron flavor state is almost identical to the ν_2 mass state for the electron number densities found near the center of the Sun, which is where such neutrinos are produced ($V \approx 2 \times 10^{-8}$ meV).

To determine how this state evolves on its way to the Earth, the first question to consider is how the neutrino evolves on its way out of the Sun. Because the scales on which the electron density vary inside the Sun are macroscopic and enormous in comparison to the size of a neutrino wavepacket, the Hamiltonian experienced by a neutrino evolves very smoothly, and the adiabatic approximation can be applied. In the adiabatic approximation, level crossing is forbidden, so states transition smoothly from their initial energy eigenstate mixture into an equal mixture of final energy eigenstates.

In the case of ^{8}B neutrinos, this causes a nearly complete transition into the ν_2 vacuum eigenstate since its initial state is nearly a mass-perturbed ν_2 state. Since the neutrinos thus escape the Sun in an energy eigenstate (to a very good approximation), they then propagate without oscillating to the Earth, where they are detected in the flavor basis. Thus to a first approximation the electron neutrino survival probability, P_{ee}, for solar neutrinos is simply $\sin^2\theta_{12}$ ($|U_{e2}|^2$ with the approximation that $\sin\theta_{13} = 0$).

This can be made more precise by including the small contributions from the other energy eigenstates. Let $\hat{U}$ represent the mixing matrix at the position in the Sun where the neutrino was created. In practice, $\hat{U}$ depends on the radial position within the Sun (since it is electron density dependent) as well as the energy of the neutrino in question. $\hat{U}$ can be computed by replacing the vacuum mixing angles with those in matter.

In this general approach, vacuum oscillations do take place once the neutrino escapes the Sun. However, the phase $\Delta m^2 L/E$ acquired by the neutrinos is essentially random since the neutrino energy cannot be resolved on a scale at all comparable to the number of oscillation

lengths travelled from the Sun. These vacuum oscillations are therefore averaged over in a real experiment.

We can calculate the survival probability in a way that captures all these effects as follows. Let the adiabatic propagator within the Sun be $\hat{P}_1 = \delta_{ij}$ in the energy basis, and the vacuum oscillation propagator be $\hat{P}_2 = e^{im^2 L/2E}$. Then the oscillation probability is given by

$$\begin{aligned} P_{ba} &= \left| \left\langle \nu_a | \hat{P}_2 \hat{P}_1 | \nu_b \right\rangle \right|^2 \\ &= \left| \left\langle \nu_a | e^{-im^2 L/2E} I | \nu_b \right\rangle \right|^2 \\ &= \left| \sum_{ij} \left\langle \nu_i | U^*_{ai} e^{-im^2 L/2E} \hat{U}_{bj} | \nu_j \right\rangle \right|^2 . \end{aligned} \tag{2.12}$$

Here we have followed the usual convention in defining

$$|\nu_l\rangle = \sum_i U_{li} \, |\nu_i\rangle \ , \tag{2.13}$$

where the l states represent flavors and the i states represent mass eigenstates.

The vacuum propagator acts trivially in the mass basis, so this simplifies to:

$$\begin{aligned} P_{ba} &= \left| \sum_{ij} U^*_{ai} e^{-im_i^2 L/2E} \delta_{ij} \hat{U}_{bj} \right|^2 \\ &= \sum_{ij} U^*_{ai} U_{aj} \hat{U}_{bi} \hat{U}^*_{bj} e^{i\Delta m^2_{ij} L/2E} \\ &= \sum_i \left| U_{ai} \hat{U}_{bi} \right|^2 . \end{aligned} \tag{2.14}$$

The last step follows because the oscillatory term will average to zero unless $i = j$ (again, since the phase will vary enormously between neutrinos).

Although the abstract representation of the solar neutrino survival probability in equation (2.14) is less intuitive than the usual expression in terms of mixing angles, it will be helpful in calculating the perturbative effects we will study in Chapter 5.

CHAPTER 3

STANDARD MODEL EXTENSION

Lorentz symmetry is so deeply entwined in our physical models that it can be difficult to think clearly about the kinds of effects that could be possible in its absence. Any test of Lorentz symmetry therefore benefits from a framework for categorizing the possible unconventional effects that must be considered once that assumption is dropped. The benefits are threefold: it allows comparison between experiments that may be sensitive to the same effects, it provides a complete list of effects to consider, and it ensures that the effects are logically consistent and independent [42]. Such a framework has been developed in depth for the field content of the Standard Model by Kostelecky and his collaborators, and is called the *Standard Model Extension* (SME) [13, 14]. It considers all Lorentz symmetry violating interactions of the Standard Model fields. This framework will be used to determine the physical signals of Lorentz violation to which SNO is sensitive, and will also provide a standardized way to report the results. Before discussing the SME in enough detail to explain the origin of the effects for which we will search, we will review the physical basis of Lorentz symmetry.

3.1 Lorentz Symmetry

Lorentz symmetry reflects the invariance of physical law under changes of inertial frame. This idea has deep roots in mechanics [43]. One can arguably trace the first conception of this idea to the Copernican Principle that the Earth is not a privileged frame of reference. Galileo had something like the modern viewpoint in mind by 1632 when he articulated the idea that it is only possible to perceive relative and not absolute motion. He used this fact to explain why we cannot perceive the rapid orbital motion of the Earth.

Galilean symmetry later came to refer to a specific form of frame invariance that derived from the assumption within Newtonian mechanics that time is measured identically by all observers, in which case the coordinate measurements of two observers moving with relative

velocity $\vec{v}$ can be related by

$$\vec{x}' = \vec{x} - \vec{v}t\,, \tag{3.1}$$

assuming that the spatial origins of the two observers coincide at $t = 0$. It was the specific form of this transformation, and not the idea of the equivalence of inertial frames, that had to be replaced after the revolution of relativity. The discovery that the frequency and not the velocity of light depends on the relative velocity of its source and an observer demanded a new transformation law. The Galilean transformation (equation 3.1) was replaced by the Lorentz transformation, under which coordinate measurements of two observers moving with relative velocity $\vec{v} = v\hat{x}$ can be related by

$$\begin{aligned} x' &= \gamma(x - vt) \\ t' &= \gamma(t - vx/c^2) \end{aligned} \tag{3.2}$$

where

$$\gamma = \frac{c}{\sqrt{c^2 - v^2}}\,. \tag{3.3}$$

That is, spatial and time coordinates are mixed under boosts in a Lorentz transformation.

The Lorentz transformations form a group in the sense that the subsequent operation of two Lorentz transformations is also a Lorentz transformation. The group is generated by six operators: rotations about three orthogonal axes, and boosts along the same. Together with the group of spatial translations, they form the Poincare group. In addition to its roots in relativistic mechanics, Lorentz symmetry plays a critical role in theories of fundamental particles. In Quantum Field Theory, the allowed particle models (for example, the scalar, spinor, and vector fields) reflect different representations of the Lorentz group.

Lorentz symmetry is also closely related to the discrete symmetries of particle physics: charge conjugation (C), parity (P), and time reversal (T). Greenberg established in 2002 that CPT violations necessarily imply Lorentz violations (the converse is not true) [11]. This means that every possible CPT violation is included in the SME. Thus a search for

Lorentz violations would also be sensitive to CPT violations, should they exist.

3.2 SME Framework

The Standard Model Extension (SME) was introduced by Kostelecky et al. [13, 14]. It provides a coherent description of particle physics that includes all possible Lorentz violating operators that could arise from the spontaneous breaking of Lorentz symmetry while preserving the Standard Model gauge invariance.

To give a somewhat concrete motivation for this class of theories, consider a UV completion of the Standard Model given in terms of strings. The theoretical considerations that guarantee CPT symmetry fail in the case of strings. One might therefore generically expect CPT symmetry to be broken in such a theory, which, in light of the CPT theorem, would suggest that Lorentz symmetry may be broken in its low-energy effective theory. Furthermore, any model in more than four spacetime dimensions (as would be the case for strings) is expected to contain spontaneous breaking of Lorentz symmetry, which, assuming this extends into the conventional dimensions, may be observable as a vacuum expectation value of Lorentz tensors [13].

The requirement that the theory can be generated through spontaneous symmetry breaking ensures that it would maintain many of the attractive features of Lorentz symmetry, such as causality, by virtue of the Lorentz invariance of the underlying theory. Assuming that the vacuum expectation value is position independent, such properties as energy and momentum conservation would also be retained. Lastly, coordinate independence (or invariance under observer boosts) is also ensured, in spite of the fact that invariance under particle boosts is not.

Since this fact is quite counterintuitive, it is worth explaining how this can be possible in more detail. It is useful firstly to distinguish between observer Lorentz transformations and particle Lorentz transformations [13]. An observer transformation meets the traditional definition already discussed: it gives the rule for converting between coordinate measurements

made by observers in different frames. One might also consider how to relate measurements made by an observer in one frame of particles moving with different spins or momenta. This we will call a particle transformation. As long as the symmetry group is preserved, these two types of transformations are degenerate.

However, when the symmetry is broken, the two types of transformations no longer behave identically. Consider the familiar example of birefringence. We know that light can propagate with different speeds depending on the orientation of its polarization in a birefringent material. Consider a rotational observer transformation. A second observer in a rotated frame would measure both the optical axis of the crystal as well as the polarization vector of the light to be changed in the same way, and so measures the same index of refraction. Thus observer transformations are preserved. However, the first observer would measure a beam of light with a different polarization direction to have an entirely different index of refraction, and thus particle transformations are not preserved. When such an effect is present only in the presence of a special material like a crystal, we consider it a local or effective breaking of the symmetry. However, if the same behavior were observed under all conditions, if the vacuum itself exhibited such properties, we would consider it a fundamental symmetry violation and could describe it by a term in the SME.

The SME includes a large number of Lorentz non-invariant effective operators, each controlled by a distinct coefficient determining the size of that effect. These effects typically manifest in terms of annual or sidereal variations, as the Earth rotates and orbits the Sun, but there are also isotropic effects that have no directional dependence.

This framework has been widely adopted by experimentalists in reporting the limits established in a variety of areas. The results are collected into tables updated annually [44]. Most analyses in this area assume that only one Lorentz violation coefficient is nonzero, because searching for the fully general linear combination of many effects is prohibitively complicated. For this analysis, we will assume that only coefficients of one class are nonzero, and report both the full linear combination to which we are sensitive, as well as limits on

the individual components assuming the other components are zero.

Although observer independence guarantees that results can be translated between frames, the specific components measured will depend on the frame, analogously to the mixing of electric and magnetic fields under changes of frame in ordinary electrodynamics. To avoid this complication, it is convenient to adopt a standardized inertial frame for reporting SME results. The conventional choice is the solar (celestial-equatorial) inertial frame, which is particularly convenient for the case of solar neutrinos discussed here.

The frame is defined to be centered on the Sun, with z axis parallel to the Earth's rotational axis, the x axis pointing from the Earth to the Sun at the vernal equinox (March 20, 2000), and the y axis selected to complete a right-handed system. $T = 0$ is likewise defined by the vernal equinox of 2000. The frame is inertial on time scales of thousands of years [45]. An illustration is shown in Figure 3.1.

3.3 SME Neutrino Sector

The specific operators present in the SME vary according to particle type, and only those in the neutrino sector are relevant to this analysis. An explication of the SME framework in the neutrino sector is given in references [46, 47]. This section and section 5.1 extend the discussion of the prediction of the SME for solar neutrinos given in reference [48] to operators of arbitrary dimension, and update the discussion to use the spherical harmonic decomposition introduced after it was written.

In the SME, the Lagrangian for the neutrino sector can be written as [47]

$$\mathcal{L} = \frac{1}{2}\overline{\Psi}_A(\gamma^\mu i\partial_\mu\delta_{AB} - M_{AB} + Q_{AB})\Psi_B + \text{h.c.}\,. \tag{3.4}$$

Here Ψ is a six component spinor multiplet of the three neutrino fields and their conjugates, with A and B flavor indices. The first and second terms are the usual kinetic and mass terms for neutrinos, while the third term is an entirely general operator, 4 by 4 in spinor space and

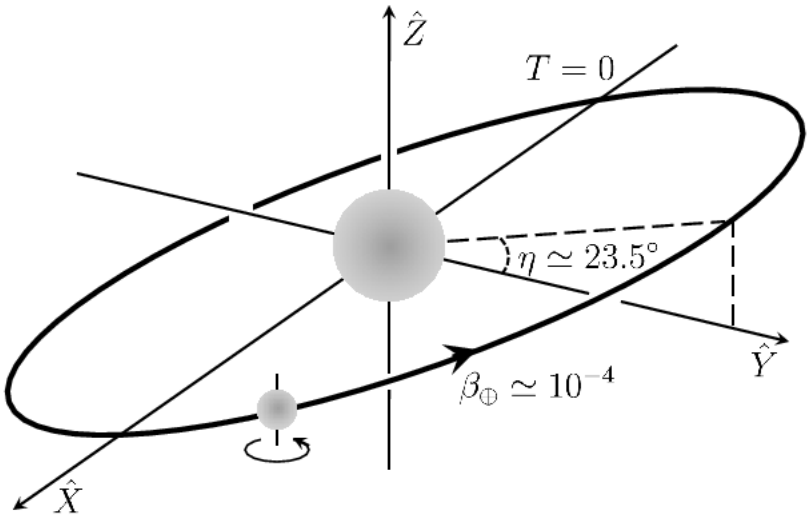

Figure 3.1: Standard solar reference frame used for reporting SME coefficients, taken from [45]. $\eta = 23.5°$ is the inclination of the Earth's orbit. The label $T = 0$ indicates the spatial position of the Earth at the time origin. β is the orbital speed of the Earth, not relevant for this measurement.

6 by 6 in flavor space, and in general involving derivatives $i\partial_\mu$. No matter the origin and form of the new interactions contained in Q, it must be possible to expand it in the basis of γ matrices:

$$\begin{aligned} Q_{AB} = &-a^\mu_{AB}\gamma_\mu - b^\mu_{AB}\gamma_5\gamma_\mu + c^{\mu\nu}_{AB}\gamma_\mu p_\nu + d^{\mu\nu}_{AB}\gamma_5\gamma_\mu p_\nu \\ &+e^\nu_{AB}p_\nu + if^\nu_{AB}\gamma_5 p_\nu + \frac{1}{2}g^{\lambda\mu\nu}_{AB}\sigma_{\lambda\mu}p_\nu - \frac{1}{2}H^{\mu\nu}_{AB}\sigma_{\mu\nu}\,. \end{aligned} \tag{3.5}$$

The coefficients c, d, and H are CPT conserving but Lorentz violating, while a, b, e, f, and g violate both CPT and Lorentz symmetry. These coefficients are labeled by a pair of flavor indices, by mass dimension d (suppressed above), and by direction indices. The direction can be expressed in any coordinate system, but it is particularly convenient for us to employ a spherical coordinate system to reflect the (approximate) symmetry of the Earth's orbit. In this system, the direction information is encoded in j and m indices that reflect the spherical harmonic decomposition of the fields.

There are also relationships between different coefficients, which arise from imposing a hermiticity condition on the theory [46]. This leads to the coefficients being Hermitian in flavor space [49], and reduces the total number of independent degrees of freedom. For a and c coefficients, results are typically presented in terms of the real and imaginary parts of the coefficients with non-negative m. Since the $m = 0$ term is real, this is a total of $2j + 1$ degrees of freedom.

More useful from a computational point of view is the effective Hamiltonian for the system, which can be determined under the assumption that the Lorentz-violating contribution is a small perturbation to the usual dynamics [46]. The full Hamiltonian is $H = H^{(0)} + \delta H$, where the Lorentz conserving Hamiltonian $H^{(0)}$ is given by equation (2.1) and the Lorentz violating perturbing Hamiltonian is given by

$$\delta H = \frac{1}{|p|}\begin{pmatrix} a_{\text{eff}} - c_{\text{eff}} & -g_{\text{eff}} + H_{\text{eff}} \\ -g^\dagger_{\text{eff}} + H^\dagger_{\text{eff}} & -a^T_{\text{eff}} - c^T_{\text{eff}} \end{pmatrix}, \tag{3.6}$$

where

$$a_{\text{eff}} = p_\mu a_L^\mu - e_l + 2i\epsilon_\mu \epsilon_\nu^* g_l^{\mu\nu} \,, \tag{3.7}$$

$$c_{\text{eff}} = p_\mu c_L^\mu - m_l + 2i\epsilon_\mu \epsilon_\nu^* H_l^{\mu\nu} \,, \tag{3.8}$$

$$g_{\text{eff}} = i\sqrt{2} p_\mu \epsilon_\nu g_{M+}^{\mu\nu} + \sqrt{2}\epsilon_\mu a_l^\mu \,, \tag{3.9}$$

and

$$H_{\text{eff}} = i\sqrt{2} p_\mu \epsilon_\nu H_{M+}^{\mu\nu} + \sqrt{2}\epsilon_\mu c_l^\mu \,. \tag{3.10}$$

This expression is written in a block matrix form, with a, c, g, and H standing for 3×3 matrices that determine the size of the Lorentz violating effects. p is the momentum and ϵ is a polarization vector orthogonal to the momentum. The upper three coordinates are for the three flavors of neutrinos and the lower three coordinates are for the antineutrinos. a_L, c_L, g_{M+} and H_{M+} are combinations of the underlying a, b, c ... operators that respect the Standard Model gauge symmetry and are therefore the physically observable combinations. The coefficients a_l, c_l, e_l, g_l, H_l, and m_l are second-order effects induced by neutrino masses. As such, their contributions are suppressed relative to the first-order terms roughly by the ratio of the neutrino mass to the neutrino energy, approximately nine orders of magnitude for solar neutrinos. Since this analysis is based on many fewer than 10^9 events, such effects are negligibly small.

The a_{eff} and c_{eff} coefficients determine the anomalous mixing of neutrinos in a Lorentz violating situation, while g_{eff} and H_{eff} would induce neutrino-antineutrino mixing. (Because of the degeneracy in mass between the neutrino and antineutrino states, this mixing has qualitatively different features than mixing among neutrinos or antineutrinos.) Because it is expected that a and c type operators and g and H type operators would arise from different underlying physics, and because SNO is sensitive to these terms at widely different levels, it is reasonable to perform an analysis for each of these types of terms separately. For the purposes of this analysis, we will assume that g_{eff} and H_{eff} are negligible.

coefficient	j	number
$(a_{\text{eff}}^{(3)})_{jm}$	0, 1, 2	81
$(c_{\text{eff}}^{(2)})_{jm}$	1	27
$(c_{\text{eff}}^{(4)})_{jm}$	0, 1, 2	81
$(g_{\text{eff}}^{(2)})_{jm}$	1	36
$(g_{\text{eff}}^{(4)})_{jm}$	1, 2	96
$(H_{\text{eff}}^{(3)})_{jm}$	1, 2	48

Table 3.1: Renormalizable SME effects in neutrino sector. In each case m can take values from $-j$ to j. Adapted from reference [47].

In the most general case, each of these terms can be expanded in a series of operators of increasing mass dimension [47]. For example,

$$a_{\text{eff}}^{ab} = \sum_{djm} |p|^{d-2}\, Y_{jm}(\hat{p}) \left(a_{\text{eff}}^{(d)}\right)_{jm}^{ab} . \tag{3.11}$$

Here Y_{jm} are the usual spherical harmonic functions. This makes it clear that there are in principle an infinite number of possible effects to consider. We therefore need some criterion for selecting which ones to examine. A particularly straight-forward if slightly arbitrary choice is to consider only renormalizable terms, since the list of these is relatively modest. Renormalizable operators are often preferred in field theories because they have well-controlled behavior at arbitrarily high scales. Insofar as we think of theories as effective models, this is not a critical requirement, but there is also another reason to prefer renormalizable terms. They are also the lowest-dimension operators, which would generically be expected to be the most important, with operators of increasingly higher mass dimension suppressed by additional powers of some high energy scale [47]. The list of allowed renormalizable terms is reproduced here in Table 3.1.

In fact, we will consider only a subset of even these renormalizable terms. We have already explained that we will not consider any neutrino-antineutrino mixing effects, which eliminates the g_{eff} and H_{eff} terms. In addition, we will not search for any signals for which

the leading-order contribution comes with the mass-suppression due to helicity flips. This includes the $c_{\text{eff}}^{(2)}$, $g_{\text{eff}}^{(2)}$, and $\left(a_{\text{eff}}^{(3)}\right)_{2m}$ modes [47]. This leaves the three modes of $c_{\text{eff}}^{(4)}$ and two modes of $a_{\text{eff}}^{(3)}$ to be considered in this analysis. The correction to the neutrino Hamiltonian that we will use is therefore

$$\delta H = \frac{1}{|p|} \sum_{jm} |p| \, Y_{jm}(\hat{p}) (a_{\text{eff}}^{(3)})_{jm} - \frac{1}{|p|} \sum_{jm} |p|^2 \, Y_{jm}(\hat{p}) (c_{\text{eff}}^{(4)})_{jm} \,, \tag{3.12}$$

where j is 0 or 1 for the a term and 0, 1, or 2 for the c term.

The coefficients a_{eff} and c_{eff} have mass dimension $4 - d$ [47], so the $d = 3$ terms have dimensions of GeV while the $d = 4$ terms are dimensionless. One can see that this gives the two terms in the Hamiltonian (equation 3.12) the correct dimensions.

We will use this correction to the Hamiltonian in Chapter 5 to derive the specific signals to search for in the analysis, but let us stop at this point and discuss in qualitative terms the kinds of effects to which this Hamiltonian gives rise. The fact that we are adding a new term δH to the neutrino mass matrix means that we will perturb the neutrino mixing parameters, in much the same way that a matter potential does. However, in our case, this perturbation is not constant, but depends on the neutrino momentum p. Since we are studying solar neutrinos, the momentum is determined by geometrical considerations: it must point from the Sun to the Earth, rotating over the course of the year. The time dependence of the signal thus derives from the spherical harmonic terms in equation (3.12). Since j is 0, 1, or 2 for the terms of interest, the changes to the mixing angles will vary either once or twice per year, or will be constant in time (these are examples of the isotropic effects already mentioned). The effects can also be classified according to the energy dependence of the change, which differ for a and c terms.

CHAPTER 4

SNO DETECTOR

The Solar Neutrino Problem was a longstanding difficulty in neutrino physics. The problem began in 1968 with the initial result [50] of Ray Davis's solar neutrino detector located in Homestake mine, which found the flux of solar neutrinos to be significantly lower than what was predicted by the Standard Solar Model of the day [51]. The Davis detector relied on the inverse beta decay interaction on Chlorine:

$$\nu_e + {}^{37}\mathrm{Cl} \rightarrow {}^{37}\mathrm{Ar} + e^- \,. \tag{4.1}$$

The ^{37}Ar created in this reaction is radioactive with a month-long half-life, which allowed Davis to measure its rate of production by extracting the Argon from his detector and counting its decay rate. The initial result found roughly half the number of neutrino interactions expected by theory, with the discrepancy growing to about a factor of three after many years of additional running [52] and refinements to theory [53].

This large discrepancy showed that at least one of the experiment, the solar model, or the neutrino model were incorrect. A number of modified solar models were proposed [54] that predicted a lower temperature in the solar core to reduce the ^{8}B production rate appropriately. Another possibility was that the neutrinos produced in the Sun are lost either through a decay process or a flavor change before they reach the detector. The idea of neutrino oscillation had been raised by Pontecorvo in 1967 [23], but there was no experimental evidence in its favor and the neutrino was still widely assumed to be massless, although interest in oscillation was growing as a result of the incorrect measurement of the neutrino mass at 20 eV in 1980 [55].

A number of experiments were proposed to check the Homestake result with different detection techniques and by looking at different pieces of the solar neutrino energy spectrum in an attempt to further constrain the Standard Solar Model. By the 1990s, Kamiokande

[56] had measured solar neutrinos at higher energies, and SAGE [57] and GALLEX [58] at lower energies. All reported results inconsistent with the solar model.

These experiments relied on the same charged current interaction measured at Homestake, or, in the case of Kamiokande, on the elastic scattering interaction that provides only weak information about the non-electron flavor neutrino content. To decisively address the fundamental question of whether a flavor change was taking place, it would be necessary to measure the inclusive active neutrino flux from the Sun. Herb Chen in 1984 originated the idea [59] that separate measurements of the neutral current and charged current interactions of solar neutrinos would disentangle the issues of the solar flux and possible neutrino oscillation. Measuring the neutral current would allow for a test of the Standard Solar Model irrespective of neutrino oscillations, while a comparison of the ratio of the two rates would be able to test for neutrino oscillations regardless of whether the Standard Solar Model was correct. Since solar neutrinos have little energy to impart via the neutral current, its detection is challenging, but Chen knew that it had been observed with reactor neutrinos through the dissociation of deuterium in 1979 [60]. He therefore proposed a kiloton scale heavy water Cerenkov detector modeled on the recently constructed IMB detector.

This idea was realized in the Sudbury Neutrino Observatory, which decisively resolved the Solar Neutrino Problem with data collected between 1999 and 2006 [15]. Through its neutral current measurement, it found the flux of active neutrinos to be consistent with that predicted by the Standard Solar Model, while its measurement of the charged current was also consistent with the Homestake result. This demonstrated clearly that flavor change was responsible for the observed deficit of electron neutrinos. Art McDonald was awarded the Nobel prize in physics in 2015 for this work, along with Takaaki Kajita for observing oscillations in atmospheric neutrinos at Kamiokande. In this chapter we will discuss the design, calibration, and simulation of the SNO detector, and the physics to which it was sensitive.

4.1 Detector Design

The SNO detector is built underground in an active nickel mine in Sudbury, Ontario at a depth of 6800 feet. This depth dramatically reduces the flux of cosmic rays and helps to maintain the radiopurity of the detector, which in turn allows for an unusually low energy threshold by the standard of water Cerenkov detectors. The detector is suspended in a barrel-shaped cavity excavated from the rock, illustrated in Figure 4.1.

The SNO detector [61] consists of several nested volumes. The innermost target volume is held inside a 12 m diameter spherical acrylic vessel (AV). About 2.5 m beyond the AV is a geodesic sphere (PSUP) designed to support the 9800 8-inch inward looking photomultiplier tubes (PMTs). In a PMT, a photon incident on the cathode generates a photoelectron through the photoelectric effect. The photoelectron is then accelerated through a dynode stack to create an amplifying cascade of electrons that can be detected as a macroscopic current. Essentially all the data in the experiment are collected with these PMTs viewing the target volume. To enhance the PMT coverage achieved, each PMT was fitted with a "concentrator" or mirrored bowl designed to steer as much incident light as possible onto the phototube surface [62]. Including the concentrators increased the coverage of the detector from 31% to 54% [15].

The space between the PMTs and the AV, and also from the PMTs outward to the walls of the cavity, is filled with ultrapure water which serves as shielding to radiation coming from the PMT glass and from the rock walls of the cavity. This is necessary in spite of the precautions taken to produce clean glass for the PMTs and to reduce the radioactivity originating in the rock by five orders of magnitude by applying ten layers of urylon [15].

Since the target was filled with heavy water, it would tend to sink in the surrounding light water, and was therefore suspended from above by a set of hold-up ropes anchored to the deck over the cavity. In addition to the inward looking tubes, there are a small number of outward looking (OWL) tubes used to help veto cosmic backgrounds. The volume inside the PSUP is optically isolated from the exterior with tarping.

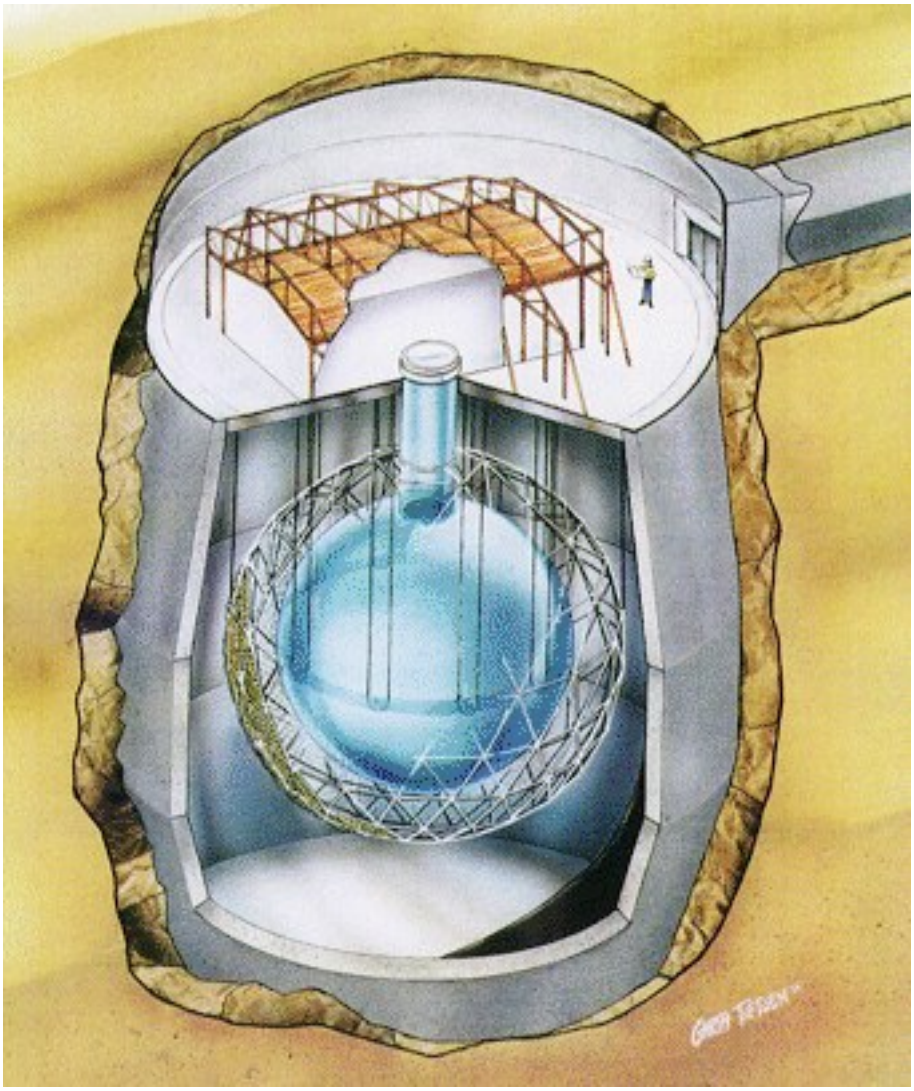

Figure 4.1: The SNO detector. In blue, the acrylic (target) vessel, with hold-up ropes in black. PMT support structure shown as geodesic sphere. At top, the deck with electronics and DAQ.

The collection efficiency of a PMT depends on the presence of any externally applied magnetic field, since these will change the path traversed by electrons in the tube. In order to achieve the best possible operating conditions for the PMTs, it is necessary to cancel the magnetic field of the Earth within the detector. This is achieved with Helmholtz ("compensation") coils built into the walls of the cavity which were tuned to achieve cancellation by about a factor of 3. This was estimated to increase the PMT collection efficiency by about 10% [63].

The PMTs are powered and read out through individual cables that extend from the PSUP to the deck above the cavity. The PMT waveforms are not digitized. Instead, each channel has a discriminator, typically set to trigger on the signal from a single photoelectron, and when the discriminator fires, the signals are integrated over three different time and sensitivity scales and held in analogue memory along with the trigger time. When a so-called Global Trigger is issued, these integrated values are digitized and read out to disk.

SNO uses an analogue trigger system to identify interesting time periods for which to record data. There are a number of different trigger types that can be selected independently. The most fundamental of these for the physics analyses is the so-called "nhit" trigger, which selects periods of phototube signal coincidences. If enough of the channel descriminators record threshold crossings within a rolling 93 ns window, a Global Trigger is sent to read out the detector. Other triggers include the Esum trigger which fires on the total charge observed in the phototubes, a pulser that fires triggers at a fixed frequency, as well as triggers for the OWL tubes, and external triggers.

SNO was calibrated using a number of different known sources. These were generally held in a decay chamber and deployed into the detector on ropes from the deck. A manipulator system could be used to pull the sources off the central axis of the detector to measure position-dependent effects. Key for this analysis was the ^{16}N source which provided the primary energy calibration [64]. This source provides a 6.13 MeV γ which is tagged by its associated β decay. The β is observed directly in the source chamber with a plastic

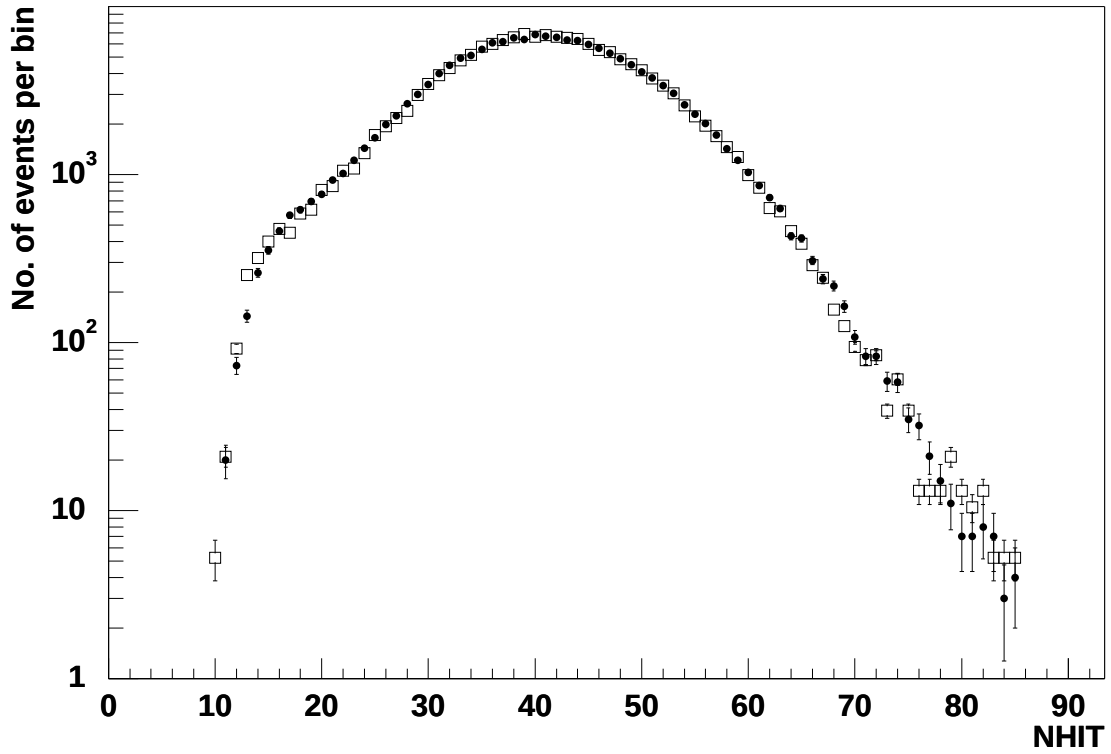

Figure 4.2: ^{16}N energy calibration data shown in black, with white points indicating prediction of (tuned) Monte Carlo simulation. Figure from reference [64].

scintillator detector. This allows a characterization of the energy response of the detector in the energy range relevant for solar ^{8}B neutrino interactions. The detector response to this source is illustrated in Figure 4.2. The source was also used to determine position reconstruction resolution. The energy scale at higher energy was verified with a ^{8}Li source with an endpoint of 13.0 MeV that roughly matches the ^{8}B neutrino energy spectrum [65]. 19.8 MeV γs from a ^{3}H source were also used in D2O phase [66]. The neutron response was calibrated with a ^{252}Cf source [67] and a ^{241}AmBe source.

The optical calibration was performed with light injection, using a laser ball deployed in the detector to diffuse light generated externally at wavelengths between 337 and 620 nm [68]. By investigating the likelihood of detecting light in a particular PMT as a function of the position of the laserball, the attenuation lengths of the light and heavy water and the angular response of the PMTs were determined [69].

In addition, the readout electronics also require calibration, to determine the charge and time scales of the digitizers, and to set the discriminator thresholds. This is achieved through a sequence of signal injection tests that are run periodically on the detector.

Since the solar neutrino interactions take place at energies within the range of natural radioactivity, extreme measures had to be taken to ensure the radiopurity of the detector. Reducing the number of γs was particularly critical for preventing a large background from the photodissociation of deuterium which could mimic the neutral current interaction. This partially motivated the deep location selected for the experiment, since the low rate of cosmic rays ensures little cosmogenic activation. In addition, the light and heavy water had to be purified extensively, and special materials were used in both the plastic lining of the cavity and the PMT glass to reduce overall background levels. Assays showed that the radioactivity in the heavy water reached a level of 5×10^{-16}g/g for U and 8×10^{-16}g/g for Th [70], well below the target levels, with modestly higher levels for the light water.

4.2 Observable Processes

SNO is a water Cerenkov detector. It can detect light coming from the passage of charged particles above the Cerenkov threshold of heavy water, which in practice means electrons, including electrons scattered by gammas. Events are reconstructed in terms of electron equivalent energy.

For neutrino events, there are three distinct kinds of events that can be observed. Although they cannot be distinguished on an event-by-event basis, their individual contributions can be statistically separated. The three processes are elastic scattering (ES), the neutral current (NC), and the charged current (CC):

$$\begin{aligned} \nu_e + d &\rightarrow p + p + e^- - 1.44 \text{ MeV (CC)}, \\ \nu + d &\rightarrow p + n + \nu - 2.22 \text{ MeV (NC)}, \\ \nu + e^- &\rightarrow \nu + e^- \text{(ES)}\,. \end{aligned} \tag{4.2}$$

The neutral current process is accessible to neutrinos of any flavor, and was used in SNO to determine the total solar neutrino flux. The Feynman diagram representation of the interaction is shown in Figure 2.3. Obviously the quark is not free in the detector, but is rather confined in a nucleon. In most cases, this momentum transfer to a bound quark would not produce a signal in the detector, but neutrinos with energies of at least 2.2 MeV can scatter against a deuteron in the heavy water with enough force to dissociate the proton and neutron. The proton is below Cerenkov threshold and cannot be observed, but the neutron will eventually capture, in turn producing gammas which will Compton scatter electrons which are finally observed through their Cerenkov radiation.

In the initial D2O phase, neutron capture was typically on deuterium, which is not particularly efficient, and many neutrons were lost, eventually capturing in the acrylic or light water. This inefficiency provided the motivation for the two subsequent phases of the experiment. The details of neutron capture in each phase will be discussed in the next section.

The charged current process involves the conversion of a neutrino into a charged lepton. The Feynman diagram representation is shown in Figure 2.3. Because ^{8}B neutrinos have a maximum energy far less than the mass of a muon, only electron-flavor neutrinos can participate in this interaction, and the interaction therefore provides a direct measure of the electron flavor survival probability. The resulting electron is observed through its Cerenkov radiation.

The last relevant neutrino interaction in the SNO detector is the elastic scattering of electrons. The Feynman diagram is shown in Figure 2.2. Neutrinos of any flavor can participate in this interaction, but electron neutrinos preferentially couple because of the crossed diagram. The rate of this interaction can thus provide a third constraint on the two parameters of interest (the ν_e flux and the ν_x flux).

4.3 Experimental Phases

The SNO experiment proceeded in three phases, each of which are represented roughly equally in the data set. The first, called the "d2o" phase, lasted from 1999 until 2001. During this phase, the acrylic vessel was filled with pure heavy water (^2H_2O or D_2O). This phase generated the purest data sample as the radiobackgrounds were very low and the optics of the concentrators were still ideal.

Following this came the second "salt" phase, when the heavy water was doped with NaCl, table salt. The purpose of this step was to take advantage of the significantly higher neutron capture cross section on chlorine in comparison to deuterium to increase the number of neutral current events observed. It also improved signal to background discrimination because of the higher energy γs released in neutron capture on chlorine in comparison to deuterium. However, inclusion of the salt also introduced some Na specific backgrounds and worsened the detector resolution because of increased scattering. The salt phase lasted from 2001 until 2003.

Finally, in the third ("NCD") phase, neutron counting devices (NCDs) were deployed in the detector to provide an independent measurement of the neutral current event rate. Data was taken with the NCDs present between 2004 and 2006. In the first two phases, the data consisted exclusively of PMT hit times and charges. The NCD phase introduced a new type of data, which was the energy detected in the NCDs themselves.

The neutron counting devices were proportional counters filled with an 85:15 partial pressure mixture of ^{3}He and CF_4, deployed in the detector on strings over a square-meter area of the inner detector volume [71]. ^{3}He has a very large neutron cross section, which produces two charged ions (p and T), which produce an electromagnetic shower in the gas. The charge is collected on an anode wire. The NCDs had two readout systems, a high-speed (shaper ADC) path that was intended to allow the collection of timing information in the case of a supernova neutrino burst, and a low-speed multiplexed discriminator (MUX) path that could distinguish between neutron candidates and other background signals, most

prominently alpha decay.

In addition to the Cf and AmBe calibration sources used in the other phases, the neutron detection efficiency of the NCDs was studied by mixing ^{24}Na into the heavy water as an isotropic source. This showed an efficiency of 26 $\pm$ 1 %. This calibration was performed only twice since it incurred significant loss of livetime in waiting for the Na to decay away (half-life 15 hours) [71].

4.4 Monte Carlo Simulation

SNO developed a highly detailed Monte Carlo simulation of their detector, called SNO Monte Carlo and Analysis (SNOMAN) [61]. The simulation is a detailed microphysical model built from the EGS4 [72] package for electron and γ propagation, MCNP [73] for neutron capture, LEPTO [74] for muons, and FLUKA [75] and GCALOR [76] for hadrons [77]. The simulation was tuned in detail to match the results of calibration runs.

Each experimental run was modeled in SNOMAN using the exact conditions present in the real detector. For example, the list of active channels and trigger settings could be set to reflect the real running conditions. In this way, detector effects could be studied in detail. Samples of all the signal and background events are available with statistics equivalent to many years of livetime. These Monte Carlo simulations are used extensively in this analysis to model both the signal and background in the parameter space of interest.

4.5 Data and its Interpretation

The SNO data consist of events, which are time periods (400 ns in length) selected by the trigger system already described. Each event contains a clock time, information on which triggers fired, and one or more PMT "hits", which represent PMTs whose signals crossed their discriminator thresholds. As has already been discussed, the data recorded for each hit is an estimate for the time of the hit relative to the trigger time and four integrated PMT

charges, differing in the gain and time period of integration.

From these elements we must reconstruct what happened in the event. Determining the energy, position, and direction of the particles with the best possible resolution is a challenging problem; SNO developed a number of different algorithms for this with differing strengths and weaknesses. However, there are a few simple principles that can provide some useful intuition in thinking about the data.

The first is the principle that the energy of the event is roughly proportional to the number of PMTs hit. We are detecting primarily the Cerenkov emission of electrons as they slow down and are stopped through ionization collisions in the water. For electrons in the relevant energy regime of 2 to 20 MeV, the time to stopping, and thus the number of photons emitted, is approximately proportional to the initial energy. The number of photons actually detected is Poisson distributed, which sets a lower bound on the possible energy resolution of the detector. In practice, SNO detected roughly 7 photons per MeV of initial electron energy.

The second is that position reconstruction is possible from the light arrival times and the known positions of the PMTs. This is essentially a geometry problem. The light originated in a relatively small region of the detector, perhaps a few centimeters in radius at most. The light mostly travels on straight paths to the PMTs; of course some light is scattered or reflected along the way, but for the most part this light arrives sufficiently late relative to the prompt light that the two types can be distinguished. The problem is then one of tracing back hypothetical lightcones from the points of observation to try to find a point of intersection that can explain most of the hits in the detector.

Although Cerenkov threshold for an electron in heavy water is only about 0.4 MeV, in practice, SNO could not reliably detect signals below 3.5 MeV. In part this was due to instrumental backgrounds at low energies and inefficiencies in the trigger, but the main limiting factor was the ability to read out the large volume of data generated at low energies.

CHAPTER 5

LORENTZ VIOLATION SIGNAL

In order to perform an analysis searching for effects generated by the Lorentz symmetry violating operators introduced in Chapter 3, we must determine the way in which those operators would change the signal we observe in SNO. We have already described this in general: there will be an energy-dependent seasonal variation in the neutrino mixing angles. In SNO, the signal would consist of seasonal variations in the charged current event rate, while the flux, and therefore the neutral current event rate, would remain fixed. In this chapter, we will derive the details of such a signal. We will also consider all other non-exotic seasonal changes to the neutrino signal that can be expected, such as those stemming from the orbital eccentricity of the Earth, and from seasonal variations in the nighttime electron neutrino regeneration in the Earth.

5.1 Signal Derivation

The Lorentz symmetry violating operators discussed in Chapter 3 could give rise to a huge variety of signals, particularly if they are large compared to the conventional mass term [78]. However, the massive three-neutrino model is a good description of neutrino behavior in a variety of experiments spanning many decades of energy, so it seems safe to assume that any Lorentz violation effects, should they exist, are small perturbations on that model. We specifically assume here, as was discussed in Chapter 3, that g and H are zero, and we consider only the leading-order corrections. The Hamiltonian can then be written

$$H = H^0 + \delta H\,, \tag{5.1}$$

where H^0 contains the conventional mass and matter effects, and δH is

$$\delta H = \sum_{jm} Y_{jm}(\hat{p}) \left((a_{\text{eff}}^{(3)})_{jm} - E(c_{\text{eff}}^{(4)})_{jm} \right) . \tag{5.2}$$

This is the expression that was derived in equation (3.12) after making the identification $|p| = E$, which is valid for any neutrino we might detect. The full Hamiltonian H will be diagonalized by a perturbed mixing matrix U, which can be written $U = U^{(0)} + \delta U$. We define for convenience

$$U = (1 + \Delta)U^{(0)} , \tag{5.3}$$

so that

$$\delta U = \Delta U^{(0)} . \tag{5.4}$$

Then recognizing that $(I + \Delta)$ diagonalizes $U^{(0)}\delta H U^{(0)\dagger}$, we can use ordinary perturbation theory to conclude that, to first order, the matrix elements of Δ are given by the corrections to the eigenstates of $H^{(0)}$. For offdiagonal terms,

$$\Delta_{kj} = \frac{\left(U^{(0)}\delta H U^{(0)\dagger} \right)_{kj}}{E_j - E_k} = \sum_{a,b} \frac{U_{ja}^{(0)} U_{kb}^{(0)*}}{E_j - E_k} \delta H_{ab} , \tag{5.5}$$

where E_i is the energy of the i^{th} unperturbed mass state, and a and b are flavor indices. For the diagonal entries $\Delta_{jj} = 0$ since corrections to the norms of the eigenvectors first appear at second order. In this section, a, b, c, and d will represent flavor indices, with i, j, k, and l used for mass state indices.

Combining this expression with equation (5.4) we see

$$\delta U_{ic} = \sum_j \Delta_{ij} U_{jc} = \sum_{abj} \frac{U_{ja}^{(0)} U_{ib}^{(0)*} U_{jc}^{(0)}}{E_j - E_i} \delta H_{ab} . \tag{5.6}$$

In this and subsequent expressions, it should be understood that the sum does not extend

over diagonal entries (i.e., $j \neq i$).

We can use this corrected mixing matrix to compute the corrections to the survival probability. To first order, the transition probabilities will be (following equation 2.14)

$$\begin{aligned} P_{ba} &= \sum_i \left| \left(U^{(0)} + \delta U \right)_{ia} \left(\hat{U}^{(0)} + \delta \hat{U} \right)_{ib} \right|^2 \\ &= P_{ba}^{(0)} + 2 \sum_i \left(\left| U_{ia}^{(0)} \right|^2 \mathfrak{Re} \left(\hat{U}_{ib}^{(0)} \delta \hat{U}_{ib}^* \right) + \left| \hat{U}_{ib}^{(0)} \right|^2 \mathfrak{Re} \left(U_{ia}^{(0)} \delta U_{ia}^* \right) \right) . \end{aligned} \tag{5.7}$$

Plugging in our expression for δU, we obtain the correction to the probability:

$$\begin{aligned} \delta P_{ba}^{(1)} = 2 \sum_{cdkl} \Bigg\{ & \left| U_{ka}^{(0)} \right|^2 \mathfrak{Re} \left(\hat{U}_{kb}^{(0)} \frac{\hat{U}_{lc}^{(0)*} \hat{U}_{kd}^{(0)} \hat{U}_{lb}^{(0)*}}{\hat{E}_l - \hat{E}_k} \delta H_{cd} \right) \\ & + \left| \hat{U}_{kb}^{(0)} \right|^2 \mathfrak{Re} \left(U_{ka}^{(0)} \frac{U_{lc}^{(0)*} U_{kd}^{(0)} U_{la}^{(0)*}}{E_l - E_k} \delta H_{cd} \right) \Bigg\} . \end{aligned} \tag{5.8}$$

Finally, we substitute equation (5.2) to get our final expression for the changes to the oscillation probabilities:

$$\begin{aligned} \delta P_{ba}^{(1)} = 2 \sum_{Jm} \mathfrak{Re} \Bigg\{ & Y_{Jm}(\hat{p}) \sum_{cd} \left(\left(a_{\text{eff}}^{(3)} \right)_{Jm}^{cd} - E \left(c_{\text{eff}}^{(4)} \right)_{Jm}^{cd} \right) \times \\ & \sum_{kl} \left(\left| U_{ka}^{(0)} \right|^2 \hat{U}_{kb}^{(0)} \frac{\hat{U}_{lc}^{(0)*} \hat{U}_{kd}^{(0)} \hat{U}_{lb}^{(0)*}}{\hat{E}_l - \hat{E}_k} + \left| \hat{U}_{kb}^{(0)} \right|^2 U_{ka}^{(0)} \frac{U_{lc}^{(0)*} U_{kd}^{(0)} U_{la}^{(0)*}}{E_l - E_k} \right) \Bigg\} . \end{aligned} \tag{5.9}$$

The final sum over kl is just a function of energy that depends on the neutrino mixing matrix in both vacuum and in the Sun. However, it is *independent* of the size of the Lorentz-violating effects and the direction of propagation. As such, it can be calculated once and for all. This specifies the (energy-dependent) linear combination of Lorentz-violating fields to which the experiment is sensitive. After factoring out the dominant linear energy dependence, we denote this by w_{cd}:

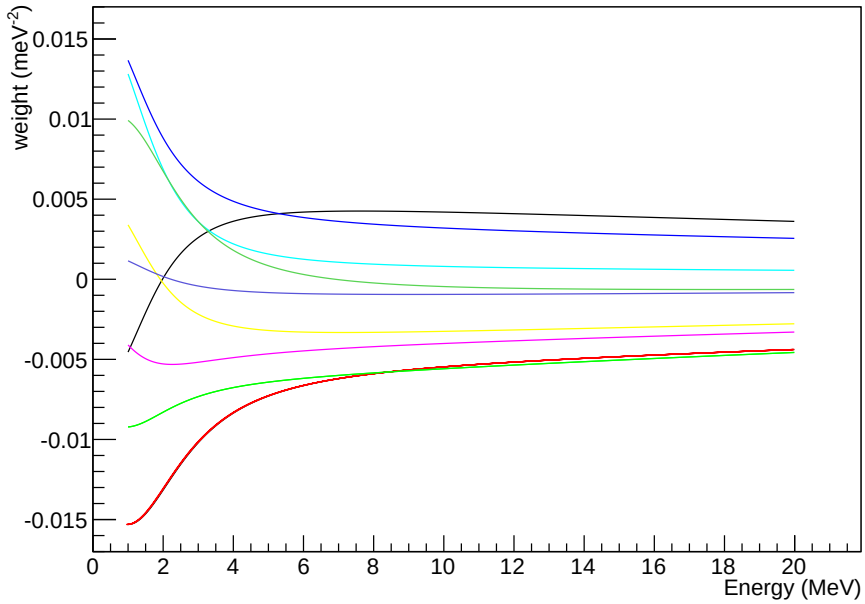

Figure 5.1: Weight functions w_{jk}^{ee} for the nine flavor combinations as a function of energy.

$$w_{cd}^{ba} \equiv \frac{2}{E} \sum_{kl} \left(\left| U_{ka}^{(0)} \right|^2 \left(\hat{U}_{kb}^{(0)} \frac{\hat{U}_{lc}^{(0)*} \hat{U}_{kd}^{(0)} \hat{U}_{lb}^{(0)*}}{\hat{E}_l - \hat{E}_k} \right) + \left| \hat{U}_{kb}^{(0)} \right|^2 \left(U_{ka}^{(0)} \frac{U_{lc}^{(0)*} U_{kd}^{(0)} U_{la}^{(0)*}}{E_l - E_k} \right) \right) . \tag{5.10}$$

With this definition, the survival probability can then be written compactly as

$$P_{ba}^{(1)} = \mathfrak{Re} \sum_{Jm} Y_{Jm}(\hat{p}) \sum_{cd} w_{cd}^{ba} \left(E \left(a_{\text{eff}}^{(3)} \right)_{Jm}^{cd} - E^2 \left(c_{\text{eff}}^{(4)} \right)_{Jm}^{cd} \right) . \tag{5.11}$$

The Lorentz-violating effects come in groups of nine labelled by pairs of flavor indices, weighted by the weight functions w_{cd}^{ee}. I have computed these electron neutrino survival weights over the energy range relevant for solar neutrinos, namely 1 - 20 MeV. The shape of the weight functions is shown in Figure 5.1. It can be seen that the different contributions become relatively constant at energies above 6 MeV, after the MSW transition has saturated. The effects in each group of nine are therefore highly degenerate.

There are two possible approaches to handling this near-degeneracy. Either we restrict ourselves to a domain in which the signals are truly degenerate, compute the linear combination of coefficients to which we are sensitive, and set a single limit on that combination, or we keep all nine signals distinct and try to fit for them simultaneously.

SNO has never included data below 3.5 MeV in published analyses, because the data there is dominated by backgrounds, and energy resolution and instrumental effects make efforts to lower the energy threshold increasingly difficult. It is clear from Figure 5.1 that the shapes of the different weights are not very different above 3.5 MeV. To quantify whether there is any chance of disentangling these components, I performed a rough sensitivity study.

I assumed a best case scenario in which SNO is sensitive to the neutrino energy spectrum itself (without the smearing from interactions present in practice), with perfect energy resolution, and without background. I randomly drew ten thousand ^{8}B events with energies above 3.5 MeV and distributed them randomly throughout a three year period. No Lorentz-violating effects were imposed. I then fit the data with my model for a group of nine effects to determine to what extent the different behaviors could be distinguished. I selected the group of effects I expected to be most easily distinguished – those with annual modulation frequency and linear gross energy dependence.

In spite of these optimistic choices, I found that the global correlation of each parameter was at least 0.985. This confirmed that there is no power to distinguish the different effects. It is therefore necessary for the analysis to take the other approach, namely to search for the single linear combination of these effects to which the detector is sensitive. For this analysis, we will apply a lower energy threshold of 7 MeV. This puts the analysis firmly in the regime where the weights have no energy dependence, and also reduces the risk of contamination from backgrounds.

To zeroth order, the linear combination of weights to which SNO is sensitive can be read off of Figure 5.1, but a more detailed treatment, taking into account the Standard Solar Model (see next section) and the detector efficiency, is appropriate. To do this, we model the

contribution to the signal from each of the components through the Monte Carlo simulation of the detector. For each event, we randomly select an origin point in the Sun according to the distribution shown in Figure 5.3 and use this to calculate the survival probability.

For setting limits, the SNO weight combination will be computed using the fit result for each mode separately. The final results are reported in Chapter 7. To give some impression of what the combination will be like, we report here the result as determined by the mixing parameters from the global neutrino fit:

$$\begin{aligned} c^{(4)}_{\rm SNO} = 10^{-2}{\rm meV}^{-2}\times \Big(&0.38c^{(4)ee}_{\rm eff} - 0.64c^{(4)e\mu}_{\rm eff} - 0.59c^{(4)e\tau}_{\rm eff} \\ &+ 0.39c^{(4)\mu e}_{\rm eff} - 0.30c^{(4)\mu\mu}_{\rm eff} - 0.42c^{(4)\mu\tau}_{\rm eff} \\ &+0.14c^{(4)\tau e}_{\rm eff} + 0.04c^{(4)\tau\mu}_{\rm eff} - 0.08c^{(4)\tau\tau}_{\rm eff}\Big) \ . \end{aligned} \tag{5.12}$$

$a^{(3)}_{\rm SNO}$ would be defined exactly the same way, substituting $c^{(4)}_{\rm eff}$ with $a^{(3)}_{\rm eff}$ in the above expression. These definitions allow us to write the change to the survival probability in a very compact way:

$$P^{(1)}_{ee} = \mathfrak{Re}\sum_{Jm} Y_{Jm}(\hat{p})\left(E\left(a^{(3)}_{\rm SNO}\right)_{Jm} - E^2\left(c^{(4)}_{\rm SNO}\right)_{Jm}\right) \ . \tag{5.13}$$

This is the expression of pratical utility for this analysis.

An impression of what a signal of this type would look like in the detector is shown in Figure 5.2. This assumes a signal in the $\left(a^{(3)}_{\rm SNO}\right)_{10}$ mode at the level of 10 GeV^{-1}.

5.2 Solar Model

An accurate solar model is important for this analysis because the details of the matter effect in the Sun, and therefore the exact combination of effects to which the detector is sensitive, depend on the energy spectrum of the neutrinos and on their point of origin within the Sun. For this analysis, I have used the BS 2005 (AGS, OP) model, which is the most

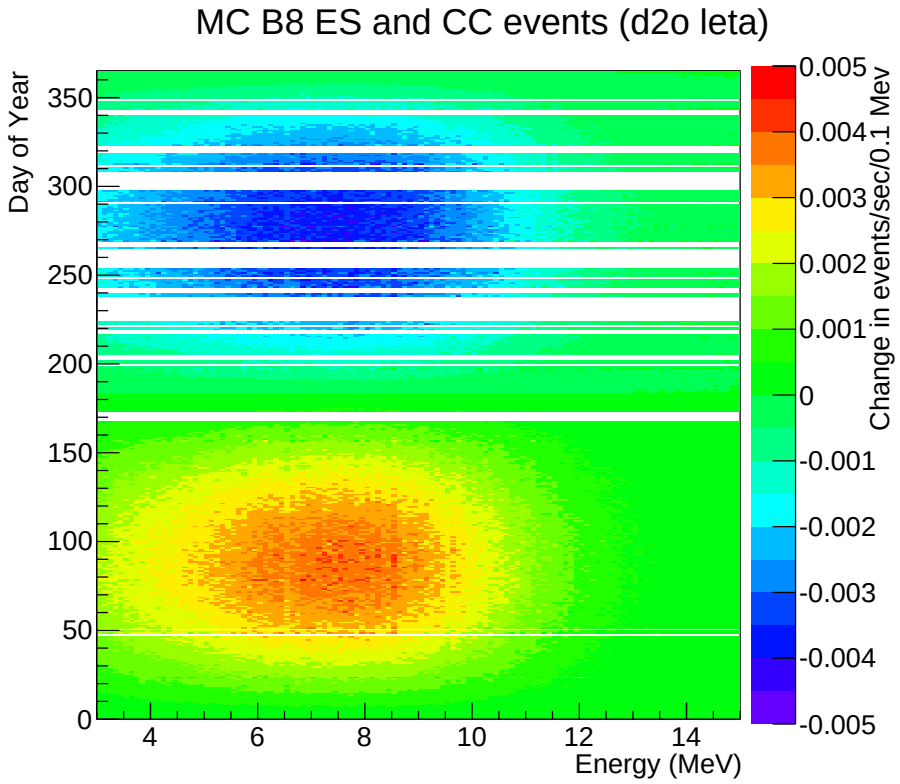

Figure 5.2: Monte Carlo simulation of the shape of the signal in the SNO detector. The vertical axis is day of year and the horizontal axis is reconstructed energy. Color indicates the change in the event rate. The normalization is assuming Lorentz violation at a level of $\left(a^{(3)}_{\mathrm{SNO}}\right)_{10} = 10\ \mathrm{GeV}^{-1}$. Simulation includes only the first two phases of the experiment. White areas are days on which there was no livetime.

Parameter	Global Fit	PDG Without SNO
$\Delta m^2_{21}/10^{-5}$ eV^2	7.37 ± 0.17	7.54 ± 0.19
$\Delta m^2_{32}/10^{-3}$ eV^2	2.48 ± 0.06	2.48 ± 0.08
$\sin^2\theta_{13}/10^{-2}$	2.16 ± 0.10	2.10 ± 0.11

Table 5.1: Best values available for mixing parameters without using data from SNO.

recent Standard Solar Model [37]. The relevant features are the energy spectrum of the ^{8}B neutrino flux, the radial distribution of ^{8}B origin points within the Sun, and the radial profile of the electron density in the Sun. (These latter two distributions are relevant because they determine the matter potential, and therefore the mass eigenstate content of the neutrino.) Plots of these two quantities are shown in Figure 5.3.

5.3 Mixing Parameters

Computation of the SNO combination and of the signal pdf more generally relies on knowledge of the neutrino mixing matrix. Since these parameters have been determined in part based on data from SNO itself, care must be taken that any external constraints applied exclude information from SNO to avoid double counting. We discuss the handling of this issue in this section.

The solar mixing angle is floated in the analysis, so we need not consider that parameter. It turns out that the other parameters have all been measured in independent experiments whose individual values and uncertainties do not differ very much from the global fits [34], so this effect does not make a large difference.

For the solar mass splitting, there is a measurement from Kamland alone [26] that is essentially identical to the PDG combined result. For the other parameters, we simply use the PDG recommended values, since these do not incorporate SNO data. The values are summarized in Table 5.1. (Note that θ_{23} is omitted because it is not relevant in the adiabatic approximation).

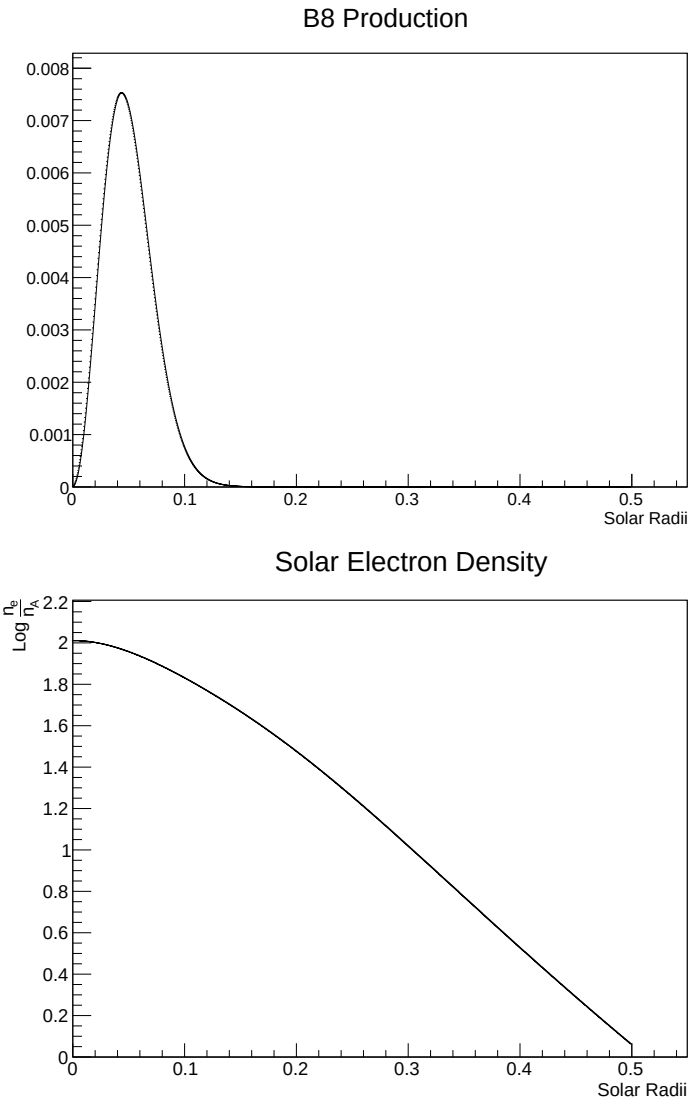

Figure 5.3: Above: Distribution of ^{8}B production radii. Below: Solar electron number density as a function of radius, plotted as Log (base 10) of n_e per cm^3 per n_A. Data taken from reference [37].

Signal	Source (Algebraic)	Source (Numeric)
E	$\sqrt{\frac{1}{4\pi}}\left(a^{(3)}_{\rm SNO}\right)_{00}$	$0.28a_{00}$
$E\sin\omega t$	$\sqrt{\frac{3}{4\pi}}\sin\Omega\left(a^{(3)}_{\rm SNO}\right)_{10}-\sqrt{\frac{3}{8\pi}}\cos\Omega\mathfrak{Im}\left(a^{(3)}_{\rm SNO}\right)_{11}$	$0.19a_{10}-0.32\mathfrak{Im}a_{11}$
$E\cos\omega t$	$-\sqrt{\frac{3}{8\pi}}\mathfrak{Re}\left(a^{(3)}_{\rm SNO}\right)_{11}$	$-0.35\mathfrak{Re}a_{11}$
E^2	$\sqrt{\frac{1}{4\pi}}\left(c^{(4)}_{\rm SNO}\right)_{00}+\sqrt{\frac{5}{16\pi}}\left(\frac{3}{2}\sin^2\Omega-1\right)\left(c^{(4)}_{\rm SNO}\right)_{20}-$ $\sqrt{\frac{15}{32\pi}}\sin\Omega\cos\Omega\mathfrak{Im}\left(c^{(4)}_{\rm SNO}\right)_{21}+$ $\sqrt{\frac{15}{64\pi}}\left(\frac{1}{2}\sin^2\Omega\right)\mathfrak{Re}\left(c^{(4)}_{\rm SNO}\right)_{22}$	$0.28c_{00}-0.08c_{20}-$ $0.14\mathfrak{Im}c_{21}+0.03\mathfrak{Re}c_{22}$
$E^2\sin\omega t$	$\sqrt{\frac{3}{4\pi}}\sin\Omega\left(c^{(4)}_{\rm SNO}\right)_{10}-\sqrt{\frac{3}{8\pi}}\cos\Omega\mathfrak{Im}\left(c^{(4)}_{\rm SNO}\right)_{11}$	$0.19c_{10}-0.32\mathfrak{Im}c_{11}$
$E^2\cos\omega t$	$-\sqrt{\frac{3}{8\pi}}\mathfrak{Re}\left(c^{(4)}_{\rm SNO}\right)_{11}$	$-0.35\mathfrak{Re}c_{11}$
$E^2\sin 2\omega t$	$\sqrt{\frac{15}{32\pi}}\cos\Omega\mathfrak{Im}\left(c^{(4)}_{\rm SNO}\right)_{22}-\sqrt{\frac{15}{32\pi}}\sin\Omega\mathfrak{Re}\left(c^{(4)}_{\rm SNO}\right)_{21}$	$0.35\mathfrak{Im}c_{22}-0.15\mathfrak{Re}c_{21}$
$E^2\cos 2\omega t$	$-\sqrt{\frac{45}{64\pi}}\sin^2\Omega\left(c^{(4)}_{\rm SNO}\right)_{20}+$ $\sqrt{\frac{15}{32\pi}}\sin\Omega\cos\Omega\mathfrak{Im}\left(c^{(4)}_{\rm SNO}\right)_{21}+$ $\sqrt{\frac{15}{32\pi}}\left(\frac{1}{2}\sin^2\Omega+\cos^2\Omega\right)\mathfrak{Re}\left(c^{(4)}_{\rm SNO}\right)_{22}$	$-0.08c_{20}+$ $0.14\mathfrak{Im}c_{21}+0.36\mathfrak{Re}c_{22}$

Table 5.2: Table of independent observables, and the terms in the theory that contribute to each.

5.4 Observables

Even after grouping the nearly-degenerate parameters into effective parameters, we are left with four parameters of dimension 3 and nine of dimension 4. Those of dimension 3 produce signals that cycle at most once per year, and grow linearly with energy. Those of dimension 4 grow quadratically with energy (and are therefore independent of the dimension 3 operators), and have signals that cycle at most twice per year. Simple considerations from Fourier analysis show that there can be at most three and five independent observables in these two cases. We therefore decompose the signals into their Fourier modes and summarize these combinations in Table 5.2. These are the signals for which we will search directly in this analysis.

For the purpose of providing intuition about what these signals would look like in the SNO detector, it is necessary to propagate the changes to the survival probability through the nuclear interactions and detector effects. This can be achieved by reweighting the SNOMAN Monte Carlo data.

The charged current events must be modified by the total change to the survival probability, while the elastic scattering events are modified by a reduced amount (roughly 5/6). There is no change to the neutral current events, since these are flavor-independent.

For each SNOMAN ^{8}B event, I randomly sampled a solar origin point according to the Standard Solar Model, and used this to calculate its survival probability. The set of all eight signals is shown in Figure 5.4. These templates are meant only for illustration, and are not used explicitly in the final fit. The fit instead uses pdfs for solar events that include both the Standard Model and Lorentz violating effects together, but these pdfs are calculated using the same SNOMAN files and the Lorentz violating effects are the same as those calculated here. One difference between the pdfs used in the fit and the templates shown here is that in the fit, the details of the Standard Solar Model are not folded in. It is not necessary to include these effects in the fit because they do not change the shape of the signal, but only impact our interpretation of the signal in terms of the linar combination of effects they reflect.

We have now finished our derivation of the signal that would be produced in SNO by Lorentz violation. Before we can move on to develop an analysis to look for these signals, we must first consider whether there are any conventional effects that would also produce a similar signal that must be controlled for. In fact there are two conventional effects that give rise to seasonal variations in the number of solar electron neutrinos detected in SNO: the eccentricity of the Earth's orbit, and the matter effect in the Earth. We address these issues in the next two sections.

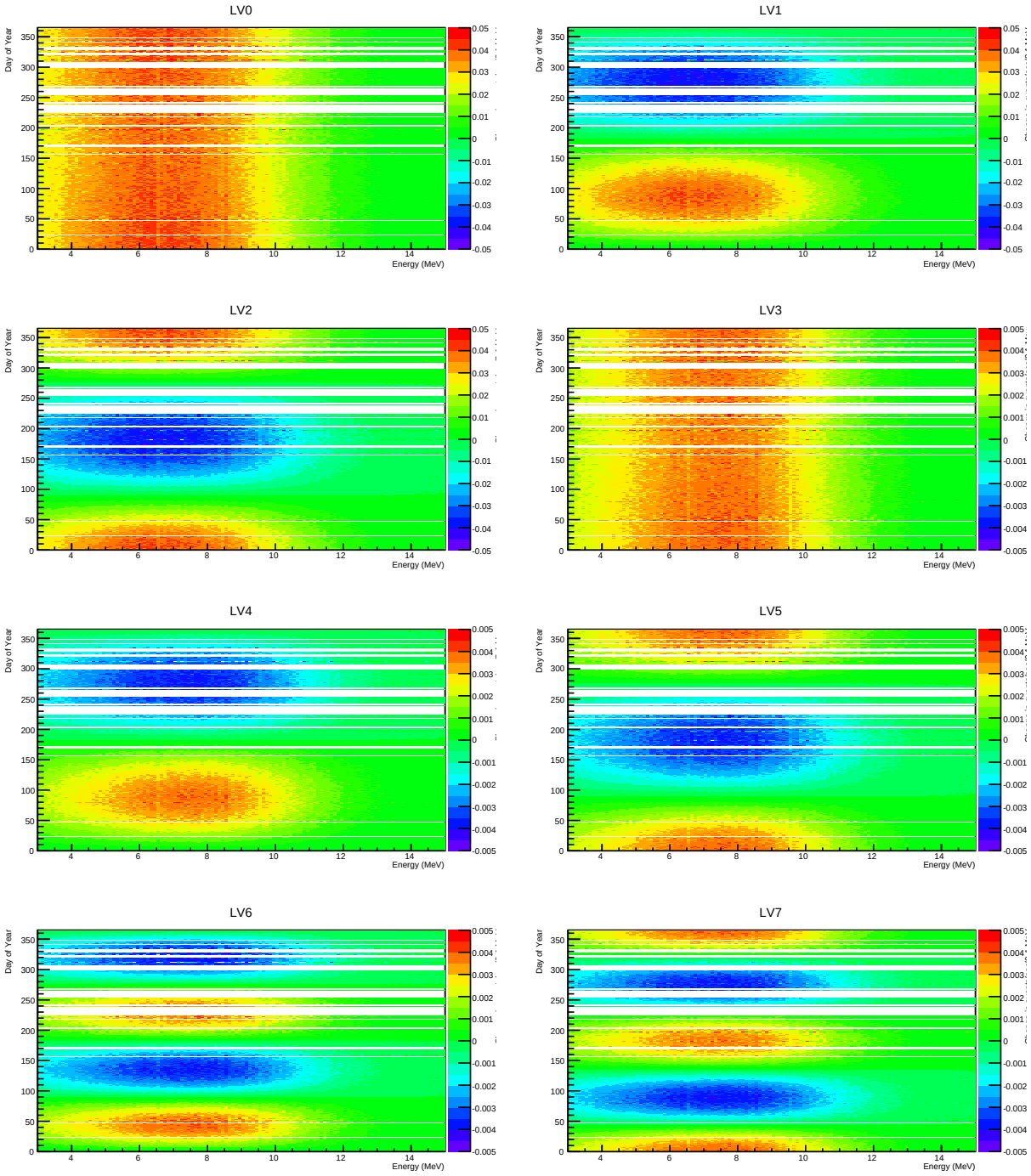

Figure 5.4: The eight independent Lorentz violating observables as they would appear in the first two phases of the experiment. L0, L1, and L2 are proportional to E, while the other signals are proportional to E^2, and can therefore be seen to be shifted slightly toward higher energies.

5.5 Day-Night Effect

During the day, solar neutrinos impact SNO from above, while during the night, they traverse the Earth and enter from below. Although this does not reduce the neutrino flux at night, the presence of electrons in the Earth has an effect on neutrino mixing just as it has in the Sun. Because the density of the Earth is much lower than in the solar core, the effect is considerably weaker, but it does push the ν_2 state back toward ν_e. The effect is therefore called electron neutrino regeneration [20].

This Earth matter effect therefore leads to a difference in the electron neutrino survival probability between day and night. The leading-order consequence of this fact is that there will be more electron flavor neutrinos during the winter when the night is longer than during the summer. Since this is a seasonal variation in the effective survival probability, it is important that we control for this effect.

There is also a second-order effect stemming from the fact that the amount of regeneration itself varies depending on the exact path through the Earth taken by the solar neutrinos. We will show below that this effect has little impact on the analysis.

Estimates for both the instantaneous and the year-averaged nighttime survival probability were taken from reference [79]. It turns out that the year-averaged effect depends only on the local electron number density in the vicinity of the detector. This can be understood as a stationary phase approximation for the rapidly oscillating phase accumulated by the neutrinos along different paths through the Earth. The correction factor can be expressed as $p_{\text{night}} = p_{\text{day}} \left(\frac{1+\delta}{1-\delta}\right)$, where

$$\delta = \frac{-\cos 2\theta_m \sin^2 2\theta}{1 + \cos 2\theta_m \cos 2\theta} \frac{EV}{\Delta m^2} \,. \tag{5.14}$$

As before, V is the effective matter potential, this time reflecting the electron number density in the vicinity of the detector. In reference [79], it is shown that using the range $V = (1.1 \pm 0.1) \times 10^{-10}$ meV more than covers any errors between the exact result and this

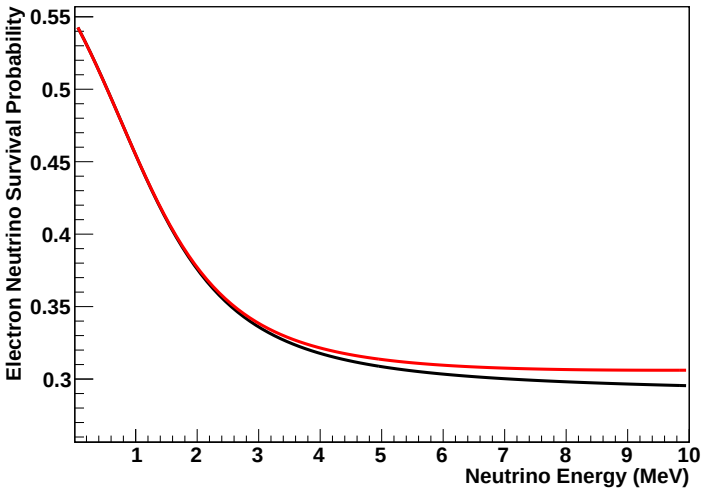

Figure 5.5: Year-averaged survival probability in day (black) and night (red).

approximation. The shape of the effect is shown in Figure 5.5. Averaged over the year, the survival probability is about 0.9% higher at night than during the day for the events selected for analysis. The energy-dependent nighttime correction is explicitly applied in the analysis.

To investigate the time variation of the regeneration effect, I have used another approximation introduced in reference [79] to compute the effect:

$$P = \frac{1}{2} + \frac{1}{2}\cos 2\theta_{\rm Sun}\cos 2\theta_{\rm Sudbury} + \cos 2\theta_{\rm Sun}\sin 2\theta \sum_{j=1}^{n-1} \Delta\theta_j \cos(dE_j L_j)\,. \tag{5.15}$$

Here

$$dE_i = \sqrt{\left(\frac{\Delta m^2}{2E}\right)^2 - 2\left(\frac{\Delta m^2}{2E}\right) V_i \cos 2\theta + V_i^2}\,, \tag{5.16}$$

where V_i is the matter potential in each layer, L_i is the pathlength traveled in each layer, $\theta_{\rm Sun}$ and $\theta_{\rm Sudbury}$ are the matter-perturbed mixing angle θ_{12} at the electron densities found in the Sun and in Sudbury, respectively, and $\Delta\theta_i \equiv \theta_{i+1} - \theta_i$, where θ_i solves

$$\sin 2\theta_i = \frac{\Delta m^2 \sin 2\theta}{4EdE_i}\,. \tag{5.17}$$

Layer	Outer Radius (km)	Mean Density	Inner Density	Outer Density
		Electron Density (mol/cm^3)		
Inner Core	1221	6.0	-	5.95
Outer Core	3480	5.0	5.7	4.5
Lower Mantle	5700	2.4	2.8	2.1
Upper Mantle	6370	1.8	2.0	-

Table 5.3: Earth model parameters

To apply this estimate, I designed a model of Earth consisting of four layers of constant density, with different densities at the layer interfaces to ensure a more accurate contribution to $\Delta\theta_i$. This model was based on the Preliminary Reference Earth Model [80], but simplified the density profile for computational ease. The parameters of my model are given in Table 5.3.

As noted in reference [81], the size of the effect depends on both the time and day of year, with the largest effects being concentrated in the hours about midnight and the weeks around the summer and winter solstices, again because of a stationary phase effect. To verify that the calculation made with the simplified Earth model could reproduce the more detailed computation, I reproduced the energy dependence of the day-night asymmetry averaged over different seasonal periods. The result, shown in Figure 5.6, corresponded with the published plots at the level of 10%, and some degree of difference is expected from the fact that my calculation is made for the latitude of Sudbury, which is different from the latitudes shown in the paper.

We use this model to calculate the day-by-day effect on the solar neutrinos observed in SNO. As a worst case scenario, we present in Figure 5.7 the day-by-day survival probability at midnight. The effect is as large as 10%.

In practice, the effect is much reduced because (i) there is kinematic smearing of the neutrino energy during interactions, (ii) the energy resolution of the detector is considerably worse than the scale of the effect, (iii) averaging over other times of the night tends to

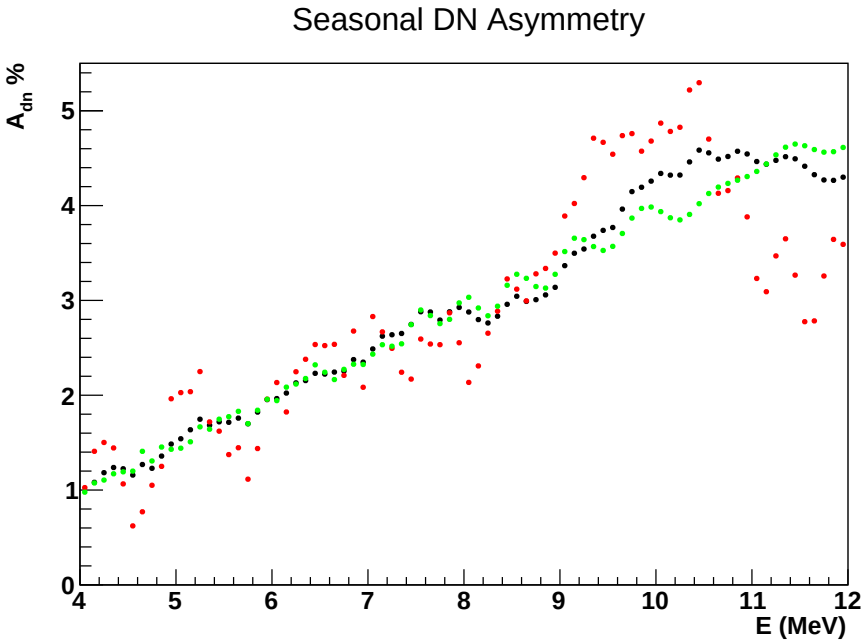

Figure 5.6: Day Night Asymmetry ($A_{dn} \equiv 2(\text{night-day})/(\text{night+day})$) as a function of energy averaged over different seasonal periods. Black points are the full-year average, red is the last twenty days of the year, and green are the six summer months. Compare to Figure 5 in reference [81].

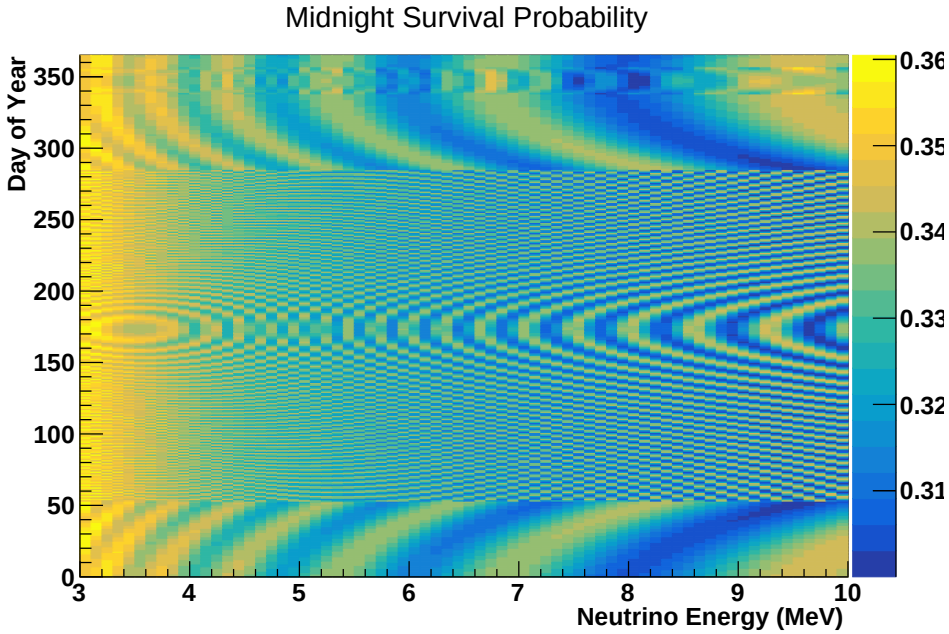

Figure 5.7: Survival probability including Earth matter effect at midnight.

reduce the effect, and (iv) day-to-day variations are mostly washed out on the seasonal scales relevant for this anaylsis.

The effect is reduced to about 3% after convolving with the detector response, which is illustrated in Figure 5.8. Because of the fine scale of this effect, it was considered inappropriate to include this model in the fit, since small changes to the density profile could completely change the value of the effect on each day because of the rapid oscillations. Instead, we treated it as a systematic uncertainty. The data from Figure 5.8 were used to draw fake data samples to evaluate the size of the systematic uncertainty introduced by neglecting this effect. From this exercise, we learned that the effect on the Lorentz violating parameters is negligibly small (3 - 9% of the statistical uncertainty), and that a small bias is introduced to the mixing parameters (about 3% for the solar flux, and about 1% for the survival probability). This can be understood from the fact that since the data are not sampled exactly uniformly throughout the year, the nighttime survival probability in practice is not the year-averaged nighttime survival probability. Again, it seems dangerous to try to correct for this given that our model for the Earth's interior is not perfect, so we will live with this small uncertainty.

In practice, for each day we calculate the fraction of livetime taken during day and night and compute a day-average survival probability based on the year-averaged nighttime survival probability.

5.6 Orbital Eccentricity

Another known source of seasonal changes to the solar neutrino flux is the eccentricity of the Earth's orbit. We must be careful to account for this seasonal change in the Sun to Earth distance. This also affects the rate at which the solar direction changes over time. The Earth's orbital characteristics are well known, with eccentricity $\epsilon = 0.0167$ and perihelion on January 3 [82]. Since flux falls with the inverse square of the distance, this leads to a roughly 3% annual modulation in the solar neutrino flux.

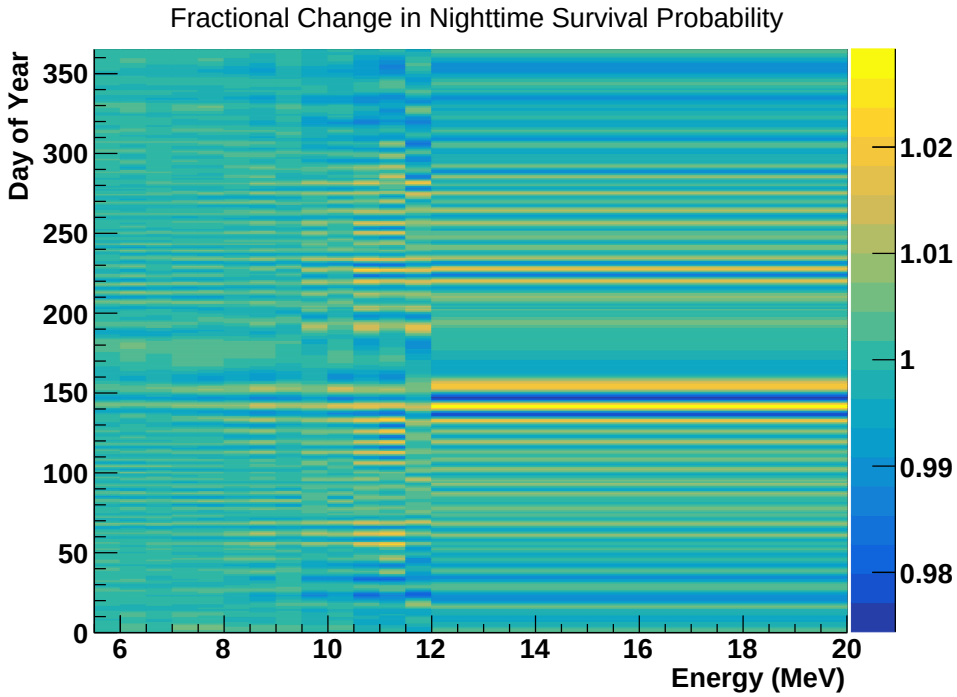

Figure 5.8: Seasonal Day Night Effect after convolving with the detector response function.

Keplerian motion is conveniently described [82] in terms of a variable called the eccentric anomaly, E, which evolves monotonically in time and is related roughly to the angular position of the Earth around its orbit. The eccentric anomaly is computed numerically by solving Kepler's equation:

$$E = M - \epsilon \sin(E) \tag{5.18}$$

where M is a timelike coordinate that evolves from 0 to 2π over an orbital period.

Using the eccentric anomaly, the angle of the Earth around its orbit and its distance from the Sun can be calculated analytically:

$$\begin{aligned} \phi &= 2 \arctan\left(\sqrt{\frac{1+\epsilon}{1-\epsilon}} \tan(E/2)\right) \\ r &= a(1 - \epsilon \cos(E)) \,. \end{aligned} \tag{5.19}$$

Here a is the semimajor axis of Earth's orbit (1 AU or 1.50×10^{11} m).

To convert this angle to the ϕ and θ of the Sun-centered frame defined earlier, we project along the axis of the Earth's inclination ($\Omega = 23.5^\circ$):

$$\begin{aligned} \Phi &= \arctan(\tan\phi\cos\Omega) \\ \Theta &= \arccos(\sin\phi\sin\Omega)\,. \end{aligned} \tag{5.20}$$

The change in flux due to the Earth's orbital eccentricity is already handled in the SNOMAN Monte Carlo, but this effect must also be explicitly included when calculating the signal.

CHAPTER 6

ANALYSIS

We now come to a description of the analysis technique. In general, the problem to address is how to evaluate the likelihood of various physical models in light of experimental evidence. Often, the models can be specified as a function of a number of physical parameters (for example the neutrino mixing angles), the values of which we wish to constrain. The fitting technique used in this analysis is based on the principle of maximum likelihood [83]. The likelihood approach can be most clearly understood in a Bayesian framework, in which the likelihood can be considered the posterior distribution of the parameters of interest after applying the experimental data to a flat prior. The formal definition of the likelihood is the probability of observing the data given particular physical parameters values, $L = P(\text{data}|\text{theory})$. We can then relate the probability of the data to the quantity of interest (the probability of the parameter values) using Bayes theorem:

$$P(\text{theory}|\text{data}) = \frac{P(\text{data}|\text{theory})P(\text{theory})}{P(\text{data})} \propto L\,, \tag{6.1}$$

where the last equality holds if we assume a flat prior for our physical parameter values ($P(\text{theory})$).

Results are typically reported in terms of the values that maximize this likelihood function (the values of the parameters that would make the experimental result more likely than any other choice of parameters would). The estimation of uncertainties is particularly straightforward once the likelihood function can be evaluated, since proper coverage is ensured by finding the points at which the likelihood has decreased by a specific amount relative to its maximum [83].

In general the likelihood function can take any number of forms, but one of the more common approaches, which is applied here, is to bin the data into a historgram and compute the probability of observing the particular number of counts observed in each bin. Assuming

independent observations, the probabilities of the individual bins factor so $L = \prod_{i=1}^{N_{bins}} L_i$. Since this product is computationally cumbersome, in practice its logarithm is used:

$$\ln L = \ln \prod_{i=1}^{N_{bins}} L_i = \sum_{i=1}^{N_{bins}} \ln(L_i)\,. \tag{6.2}$$

For Poisson-distributed data like ours, the likelihood of observing a particular number n events in a particular bin depends only on the number ν expected due to the model [19],

$$\begin{aligned} \ln L &= \sum_{i=1}^{N_{bins}} \ln\left(\frac{\nu_i^{n_i}}{n_i!}e^{-\nu_i}\right) \\ &= \sum_{i=1}^{N_{bins}} \ln\left(\nu_i^{n_i}\right) - \ln\left(n_i!\right) + \ln\left(e^{-\nu_i}\right) \\ &= \sum_{i=1}^{N_{bins}} n_i \ln(\nu_i) - \nu_i\,, \end{aligned} \tag{6.3}$$

where the term $\sum_{i=1}^{N_{bins}} \ln(n_i!)$ is dropped at the end because it is a constant (does not depend on the parameters).

For our test of Lorentz invariance, we developed a binned likelihood fit in five observable parameters: time, energy, radial position, direction relative to the Sun, and an isotropy parameter used to discriminate against backgrounds. The solar mixing angle, solar neutrino flux, and a Lorentz violation parameter are allowed to float. Although there are eight signals to consider (see Table 5.2), these are handled one at a time, assuming the others are zero. The negative log likelihood is minimized using MINUIT and confidence intervals are calculated using MINOS [84].

This analysis is built upon the previous work of the SNO collaboration. In particular, it is closely modeled on the three phase analysis [85], which represented the final ^{8}B neutrino result from SNO. This in turn combined the results of the low energy threshold analysis [86] of the first two phases with a higher energy threshold analysis of the last NCD phase [87].

For this analysis, we will be examining data only above 7 MeV. This allows lower-energy data used in previous studies of backgrounds to be included as external constraints.

In this chapter we begin by discussing which data are included in the analysis. We then cover the fit itself in more detail, including the information incorporated as constraints, and the systematic uncertainties that have been considered.

6.1 Data Selection

Data in SNO were segmented into hours-long periods called runs. The highest level of data selection is the choice of which runs to keep and which to reject. This analysis uses the run selection first finalized for the three phase analysis of the SNO dataset. The run selection required the detector to be operating in a stable state with compensation coils and the trigger system active, with the full collection of digitizers powered on, and with few of the tubes offline. It also rejected calibration runs, very short runs, and runs in which the data were very bursty. The shift reports were also reviewed to ensure that no unsual conditions were noted by the detector operators.

Within a given run, there is a further reduction of the data on an event-by-event basis. The event selection proceeds in several steps. Events are first reconstructed spatially and in energy, and corrections derived from the detector calibration are applied. Each event is evaluated on the basis of a number of data cleaning cuts intended to eliminate instrumental backgrounds. Finally, analysis cuts in radius and energy are applied to select events for analysis.

For the first two phases, the reconstruction algorithm used in this analysis is the Path Fitter ("FTP") [88]. This algorithm uses a maximum likelihood technique that considers the different possible "paths" that a photon could take in propagating from the reconstructed vertex to the PMT (direct, scattered, reflected, etc.). This was the best estimate to the ideal pdf that could be calculated on reasonable timescales. A different fitter ("FTN") [89] was needed for the NCD phase to account for the shadowing of the PMTs caused by the

Cut Name	Description
Retrigger	Any event within 5 μs of its predecessor
QVT	Events led by anomalously high charge hit
Q/nhit	Events with too many low charge hits
Crate isotropy	Events concentrated in single crates and cards
AMB	Events with anomalous charge shapes
FTS	Events with nonphysical hit times
OWL	Events with light in the external water
Junk	Orphans, ECA, and events with repeated hits
Neck	Events with light in the neck
Esum	Events triggering only esum
QCluster	Events with lonely hits with odd charges
Muon follower short	All events for 20 s after a muon
In time channel	Events with a large number of early or late hits
Flasher geometry	Rejects flashers
Nhit burst	6 non-retrigger large events within 4 s
Owl trigger	Events with high charge in the external water
Muon follower blindness	Blind version of muon follower short, where applied
Missed muon follower short	Events within 250 ms of a large event

Table 6.1: Low-level data cleaning cuts applied in the analysis for all phases.

Cut Name	Description
Shaper burst	At least 4 NCD events within 100 ms
Mux burst	At least 4 signal-like NCD events within 100 ms
Run boundary	Events within 1.1 s of run boundaries
Shaper overflow	Events within 5 ms of an NCD shaper ADC overflow

Table 6.2: Low-level data cleaning cuts applied in the analysis for the NCD phase.

NCD strings. FTN used a more robust algorithm that did not explicitly distinguish between different "path" hypotheses for individual hits.

The major instrumental backgrounds are so-called "flasher" events, which are believed to be caused by electrostatic discharge in the phototubes producing real light in the detector. Such events can be rather easily cut by their unique time-and-charge structure.

A number of low level data cleaning cuts were applied to data from all phases, which are summarized in Table 6.1. There were additional cuts that are applied only in the NCD phase, listed in Table 6.2. More detail on these cuts can be found in [90].

There is also a list of 66 events which were excluded from the LETA analysis (and are likewise excluded here) because they came as part of a burst (see [91]).

After applying these data cleaning cuts and corrections, a number of high-level cuts are used [92] to reduce the final dataset used in the fit:

- -0.12 $< \beta_{14} <$ 0.95
- ITR $>$ 0.55 for NCD phase
- Qptnhit $>$ 0 and 0.74 - ITR $< \frac{1.16}{\sqrt{\text{Qptnhit}}}$
- $0.89 < \theta_{ij} < 1.60$
- $Q_{ij} > 0.4$

β_{14} is a discriminant used to distinguish between signal and background events on the basis of the isotropy of the detected light. β_{14} is defined $\beta_{14} = \beta_1 + 4\beta_4$ where

$$\beta_l = \frac{2}{N(N-1)} \sum_{ij} P_l \left(\cos\theta_{ij}\right) \ . \tag{6.4}$$

The sum here runs over all unique pairs of hit PMTs, with θ_{ij} the angle between them, and P_l the Legendre polynomial of the l^{th} degree.

Finally the following analysis cuts are imposed:

- 7.0 MeV $<$ E $<$ 20.0 MeV
- r $<$ 5.5 m

These cuts are used to significantly suppress the number of physical background events in the sample, by restricting the analysis to the cleanest inner volume of the detector, and by looking at energies well above the natural radioactivity present in trace amounts in the detector.

Threshold	Systematic 10^{-23} GeV	Statistical 10^{-23} GeV	Total 10^{-23} GeV
5.5 MeV	3.2	6.0	6.8
6.0 MeV	2.6	6.2	6.8
6.5 MeV	2.1	6.4	6.7
7.0 MeV	1.7	6.5	6.7
7.5 MeV	1.3	6.8	6.9
8.0 MeV	0.9	7.0	7.0

Table 6.3: Estimated statistical and systematic uncertainties as a function of lower energy threshold for a coefficients. Results for c coefficients had a similar energy dependence.

	Phase		
Dataset	D2O	Salt	NCD
All events	128421085	114974237	175121813
Physics	8771553	4245798	16415321
Analysis	1167	2297	1537

Table 6.4: Data reduction by phase. Physics shows the number of events passing both the data cleaning and high-level cuts; Analysis are those that additionally reconstruct within the fiducial volume at energies above 7 MeV.

The 7 MeV lower energy threshold was selected to optimize the total sensitivity of the measurement, balancing the loss of signal against the reduction in systematic uncertainty coming from possible background fluctuations (since backgrounds are heavily weighted toward lower energies). The interplay between these contributions is shown in Table 6.3.

To give some impression of the data reduction involved, in Table 6.4 we show the number of events in each phase after various stages of data cleaning.

6.2 Fit Framework

The fit uses a binned maximum likelihood approach. The prediction of the model for each bin is calculated on the basis of probability density functions (pdfs) describing the shapes of the various signals and backgrounds across the bins. These pdfs are estimated using Monte Carlo data from SNOMAN on a phase-by-phase basis that incorporates changes in the optics

Phase	Variable	Binning
D2O and Salt	Time	2540 daily bins
	Energy	10 bins from 7.0 to 12.0 MeV
		1 bin from 12.0 to 20.0 MeV
	Cos Direction	8 bins from -1 to +1
	Volume-weighted radius	5 bins from 0 to 5.5 m
	β_{14}	15 bins from -0.12 to 0.95
NCD	Time	1380 daily bins
	Energy	10 bins from 7.0 to 12.0 MeV
		1 bin from 12.0 to 20.0 MeV
	Cos Direction	25 bins from -1 to +1
	Volume-weighted radius	10 bins from 0 to 5.5 m

Table 6.5: Binning used in fit for each phase

and the event rates. The observables and binning varies in different phases based on earlier work [85, 86, 87], summarized in Table 6.5.

The contributions within the analysis region from signal and background events (assuming nominal values for the fit parameters) are shown in Figure 6.1. The fit itself uses fully three- or four-dimensional pdfs, but to visualize this, the plot shows the projections along each of the axes.

The data from the NCDs are included in the form of a constraint of 1114.6 ± 79 neutron events detected in the NCDs during the third phase of the experiment. This result comes from the pulse shape analysis of the NCD data [85], a highly detailed analysis of the data that was largely able to discriminate the neutrons from the alpha backgrounds present in those detectors.

The background levels are fixed in the fit, with uncertainties on their normalizations entering as systematic uncertainties. This is because the background levels are so low that there is no power to measure them in the analysis sample. The uncertainty contributed by this approach is insigificant to the total uncertainty budget (see Table 6.7). This will also be cross-checked by one of the sideband analyses discussed in Section 6.5.

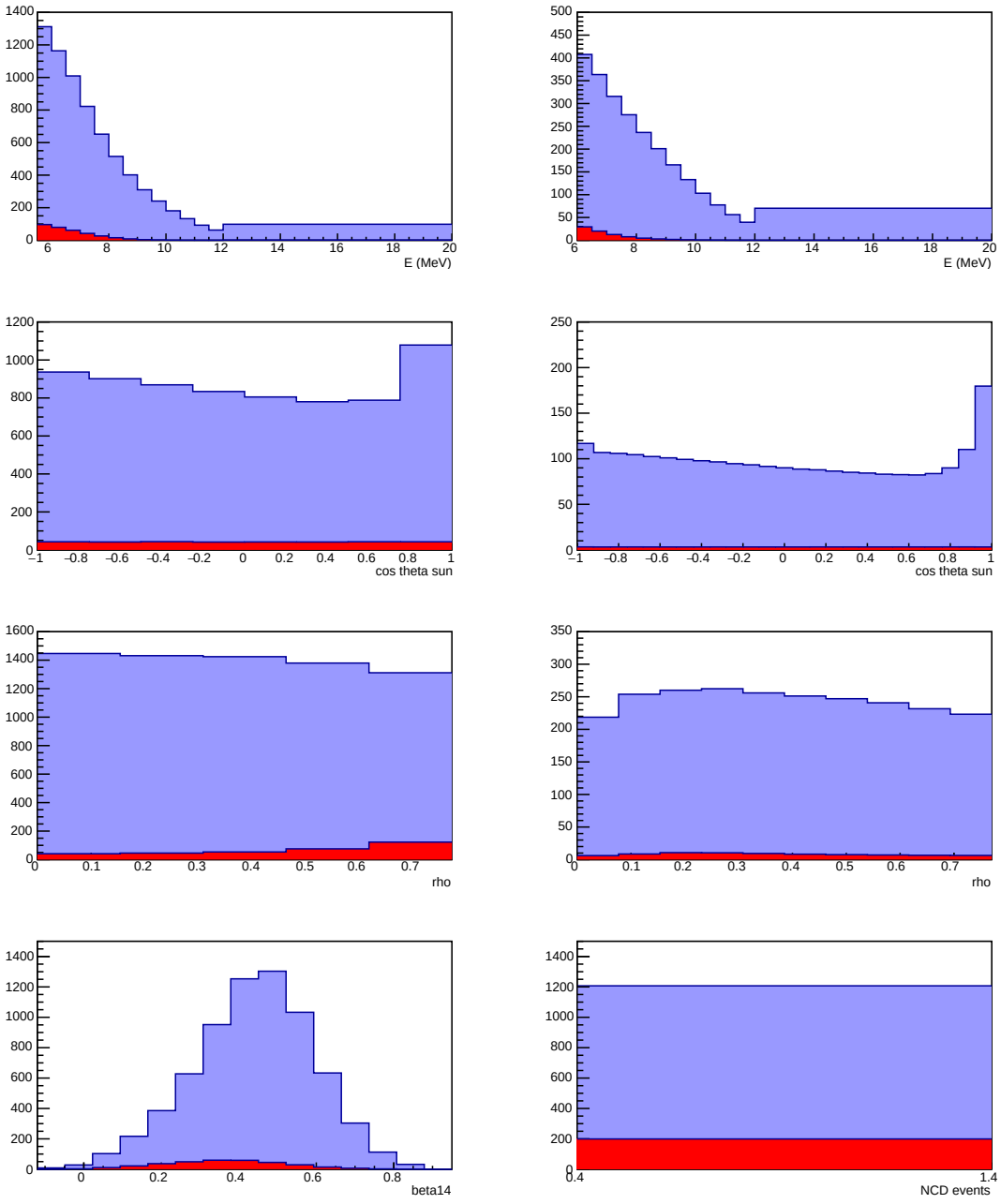

Figure 6.1: Estimated contributions from signal (blue) and background (red) events within the analysis region, assuming nominal fit parameters. The distributions are taken from Monte Carlo. The left column is a sum of d2o and salt phases, with panels (from top) showing energy, solar angle, radius, and β_{14}. The right column is NCD phase with panels (from top) showing energy, solar angle, radius, and NCD data.

6.2.1 Fake data generation

I developed two different routines for generating fake data samples, which were used for testing the fit routine and for estimating the size of the bias introduced by various systematic effects. The same Monte Carlo data used to generate the pdfs of the fit were sampled with various systematic changes applied. The shifted pdfs could then be randomly sampled to produce statistical samples, or a mean distribution could be extracted to determine biases.

To verify that the fit routine is unbiased, I used this fake data generator to make two ensembles of 100 statistical samples, one with no systematic variations applied, and one in which Lorentz violating effects were present at roughly the 1σ level.

The fit was run on these samples and the results collected as shown in Figures 6.2 – 6.4 for the sample with Lorentz violations present (the results are similar for the sample without Lorentz violations imposed). We found the results to be completely consistent with an unbiased result. Furthermore, the pulls have appropriate widths, verifying that the error estimates returned by the fit are also accurate.

6.3 Backgrounds and Constraints

In this analysis, we benefit from the extensive studies performed by the SNO collaboration in the past to estimate background levels. We use previously published constraints that were established outside of the analysis window used in this study for each of the different sources of backgrounds. These constraints are summarized in Table 6.6.

In the D2O phase, the detector had very good energy resolution that helped to reduce backgrounds at high energies. The main background for this analysis is the irreducible atmospheric neutrino background. There are additional contributions from residual radioactivity in both the heavy water (internal) and light water (external), as well as the acrylic vessel. In the two latter categories, backgrounds either travelled into the fiducial volume or were misreconstructed there.

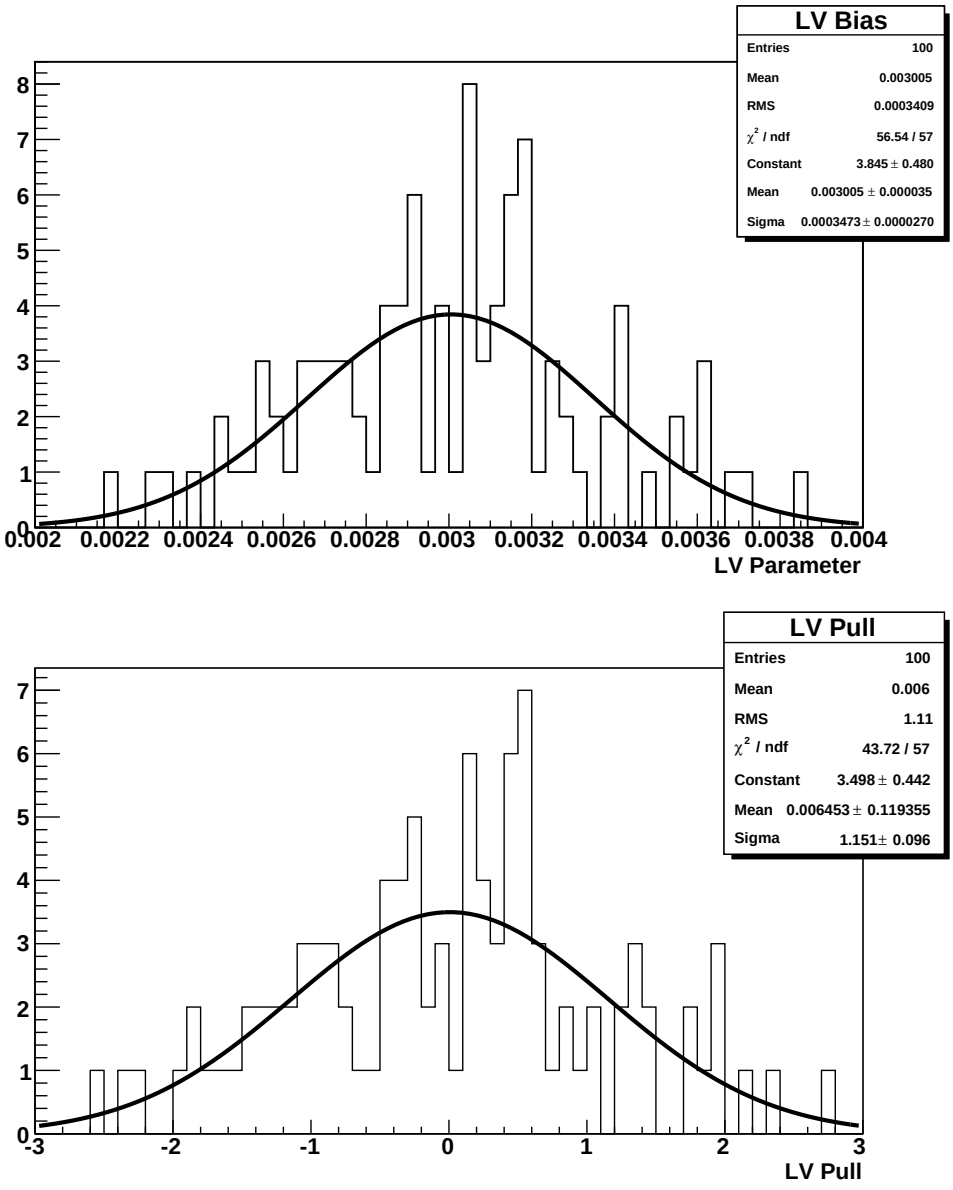

Figure 6.2: Bias and pull in Lorentz violation parameter in ensemble of 100 fake data samples generated with the parameter at 0.003.

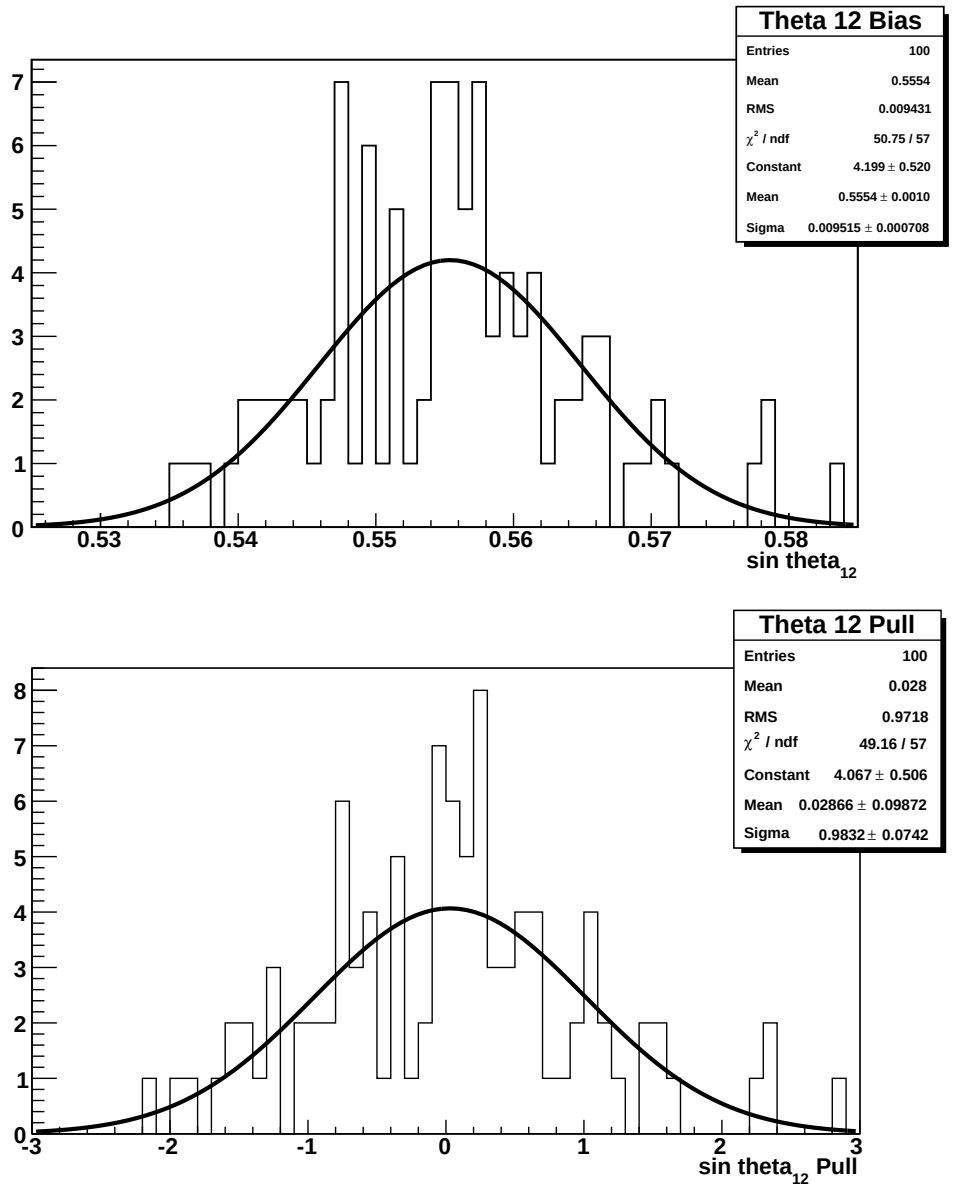

Figure 6.3: Bias and pull in $\sin\theta_{12}$ in ensemble of 100 fake data samples generated with $\sin\theta_{12} = 0.555$.

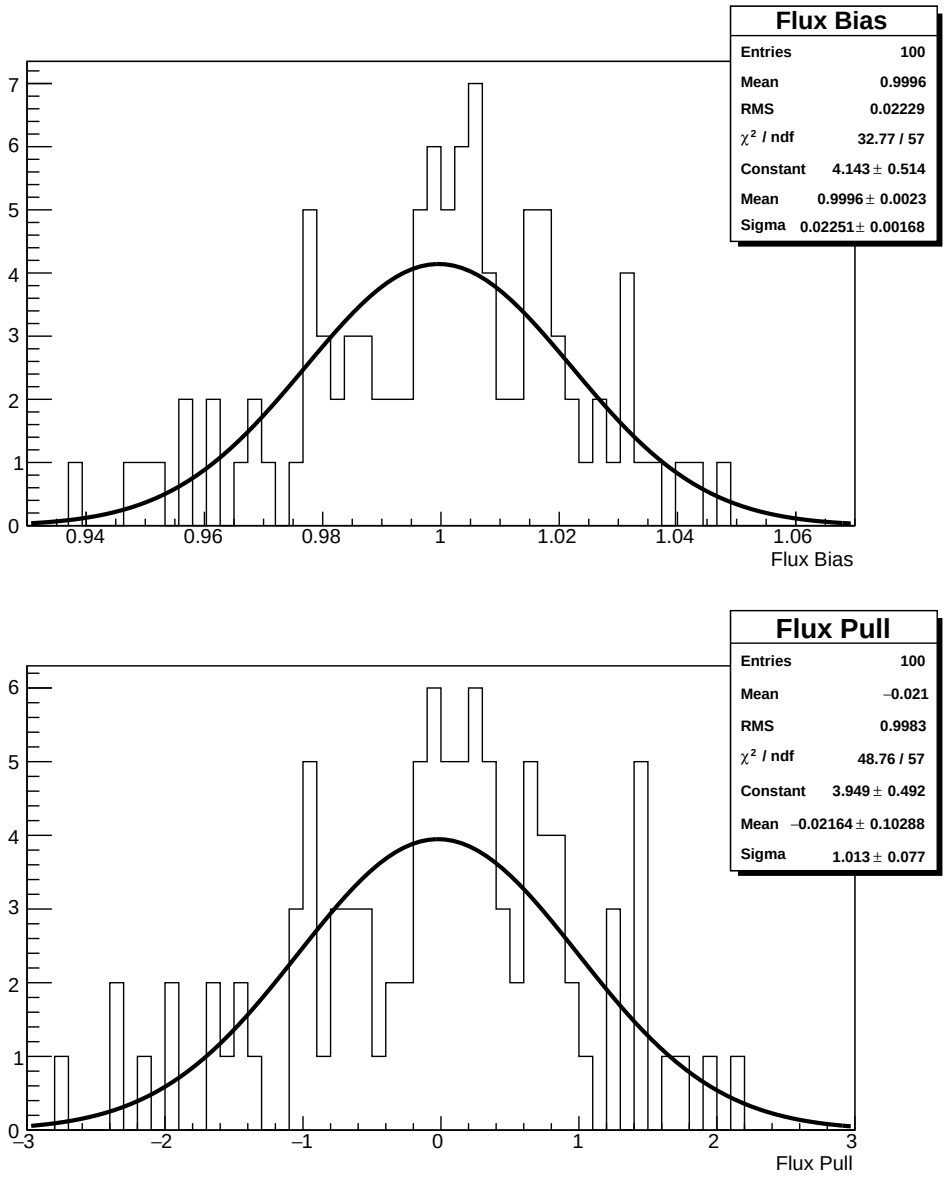

Figure 6.4: Bias and pull in the solar neutrino flux in ensemble of 100 fake data samples generated with solar flux parameter at 1.0.

Background	Phase	Constraint	Source
AV neutrons	I	1.63 ± 0.48	[93]
Internal Tl	I	1.67 ± 0.76	[85]
Internal Bi	I	0.91 ± 0.30	[85]
Atmospherics	I	5.51 ± 1.03	[85]
External Tl	I	0.46 ± 0.15	[85]
External Bi	I	0.00 ± 0.01	[85]
AV Tl	I	0.50 ± 0.50	
AV Bi	I	0.08 ± 0.08	
AV neutrons	II	27.21 ± 9.39	[94]
Internal Tl	II	22.89 ± 13.20	[85]
Internal Bi	II	16.22 ± 9.57	[94]
Atmospherics	II	7.62 ± 1.46	[85]
External Tl	II	3.70 ± 1.15	[85]
External Bi	II	1.54 ± 0.37	[85]
AV Tl	II	6.62 ± 6.62	
AV Bi	II	1.85 ± 1.85	
Na24	II	2.58 ± 0.63	[85]
Atmospherics	III	6.25 ± 1.24	[85]
External n	III	4.47 ± 2.25	[85]
K2	III	2.97 ± 0.48	[85]
K5	III	3.61 ± 0.66	[85]
D2O pd	III	2.10 ± 0.32	[85]
NCD pd	III	1.79 ± 0.61	[85]
Atmospherics	IIIb	13.6 ± 2.70	[85]
External n	IIIb	40.90 ± 20.60	[85]
K2	IIIb	32.80 ± 5.30	[85]
K5	IIIb	45.50 ± 8.40	[85]
D2O pd	IIIb	31.00 ± 4.70	[85]
NCD pd	IIIb	35.60 ± 12.17	[85]

Table 6.6: Background levels and constraints. The levels are scaled according to Monte Carlo from the rates estimated in [95]. The constraints come from a variety of other studies; care has been taken to ensure that they do not rely on data in included in this analysis. For the previously unconstrained AV backgrounds we have assumed 100% normalization uncertainties. Phase IIIb corresponds to the NCD data.

In the Salt phase, the backgrounds from radioactivity were considerably elevated, mainly because the slightly reduced energy resolution increased the number of events misreconstructed at higher energies. The salt itself also contributed an additional background through decays of ^{24}Na.

In the NCD phase, there were additional sources of substantial background. There were a number of hotspots present on the NCD ropes, the most prominent of which are denoted as K2 and K5 after their positions on the ropes. There were additionally photodissociation backgrounds.

In total, above 7 MeV, only 120 $\pm$ 20 background events are expected in the sample of 5001 events, or about 2%.

6.4 Systematic Effects

The effect of many possible systematic uncertainties were considered. A rough estimate for the size of these effects was garnered by determining the bias introduced by fitting the Monte Carlo data with shifted pdfs. This procedure allowed us to determine whether any effects were so severe that they needed to be floated in the fit, and also provided a basis for estimating the total sensitivity of the analysis as a function of the energy threshold, which was used to select the threshold.

The systematics can be classified into three groups: pdf normalizations, pdf shape uncertainties, and time variations. The contributions (estimated in Monte Carlo) from each of the studied effects are given in Tables 6.13 – 6.15. The total contribution from each of the three categories is summarized in Table 6.7. Details of the specific implementation of each of these effects can be found in Appendix A.

We found that most of the systematics considered, for example, the uncertainty on the various background normalizations, had minimal impact on the Lorentz violation fit, because any effect that is constant in time will not mimic a signal. The most serious effects to consider, then, are time variations. The uncertainty estimates given here were computed

Category	Uncertainty
Normalization	1%
Shapes	3%
Time Variations	27%

Table 6.7: Summary of systematic uncertainties (estimated as a fraction of expected statistical uncertainty).

using the shifted Monte Carlo data as described previously.

To evaluate the full systematic uncertainty of the final fit, we calculate empirically the rms deviation of the fit results performed with an ensemble of pdfs perturbed away from their central values. This is convenient because it automatically captures correlations between various systematics.

6.5 Background Stability

As was already mentioned, systematics arising from time variations are most dangerous to this analysis. In particular, we need to rule out the possibility that a fake signal could be produced by background rates changing over time. Time stability of background event rates in SNO had not been studied in detail in the past, so sideband analyses were undertaken to establish limits on such effects.

Only certain of the possible types of background events pose a serious concern in this regard because several of the backgrounds had no physical means by which to vary. For example, the background sources trapped in the PMT glass or the AV had no means of entry or exit from the detector, and have sufficiently long half-lives so that their decay rate did not change appreciably during the duration of data collection. Seasonal variation in atmospheric backgrounds are also believed to be negligible at the relevant energy scale [96]. The two main backgrounds of concern were therefore the internal and external radioactive backgrounds that could plausibly have varied in time because the water in the detector was recirculated to achieve the high radiopurity levels needed, and to keep the detector cool.

To address this concern, two different sidebands were defined to capture the rate of these two backgrounds. A radial sideband was used to study the stability of external backgrounds, while an energy sideband was used to look at internal backgrounds.

The radial sideband in the D2O and Salt phases is defined by:

- 6.19 m $< r <$ 7.02 m
- U·R > 0
- 3.5 MeV $<$ E $<$ 20 MeV
- other cuts as in main analysis .

The radial cut accepts events only in the region outside but relatively near the acrylic vessel, where good calibrations are available. The second cut selects only outward-going events (U is the velocity vector), which selects against PMT backgrounds. The resulting sample is roughly 90% light water radioactivity, with the remaining 10% split between AV and PMT backgrounds [91] that are expected to be constant in time.

Events passing this selection were binned by day and normalized by the day-by-day livetime. These normalized event rates were then fit to a model of a constant background plus a time varying component, according to

$$y = A(1 + p\sin(\omega t + \phi))\,. \tag{6.5}$$

The overall normalization A and the fractional power p in the particular mode in question were allowed to float. ω was set for either once- or twice-annual variations, and ϕ was either 0 or $\pi/2$. The best fit for p is taken to represent the estimate for the limit on time variation in the mode in question. The data are shown in Figure 6.5, with a summary of the best fit results in Table 6.8.

For the NCD phase, the analysis was complicated by the fact that the FTN energy reconstruction algorithm was never tuned for events that reconstructed outside the fiducial

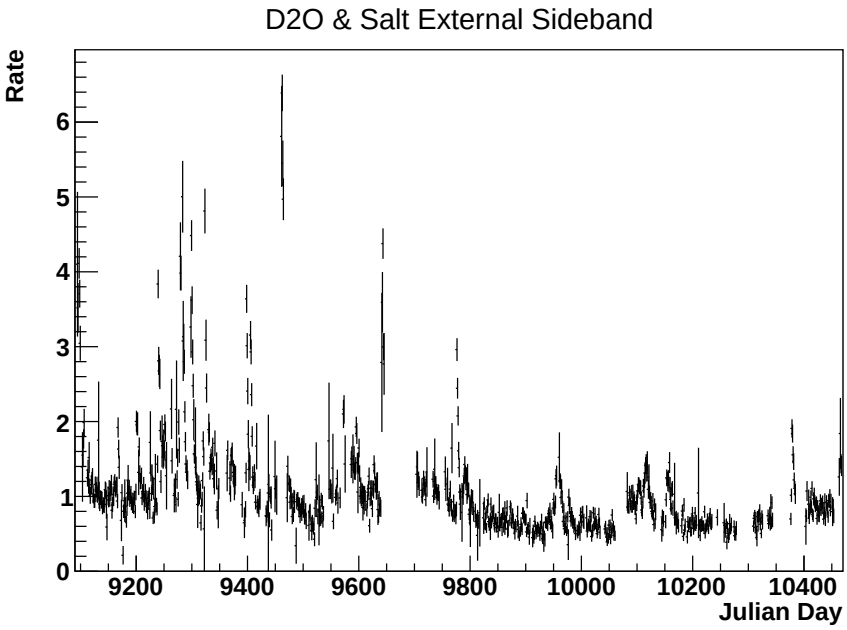

Figure 6.5: External Sideband, D2O and salt phases. Julian day counts solar days, in this case since January 1, 1975.

Mode	Best Fit
$\sin \omega t$	-9.2% ± 0.5%
$\cos \omega t$	-12.3% ± 0.5%
$\sin 2\omega t$	-12.5% ± 0.5%
$\cos 2\omega t$	-4.5% ± 0.5%

Table 6.8: Best fit for variations in relevant Fourier modes for external background rates in D2O and salt phases.

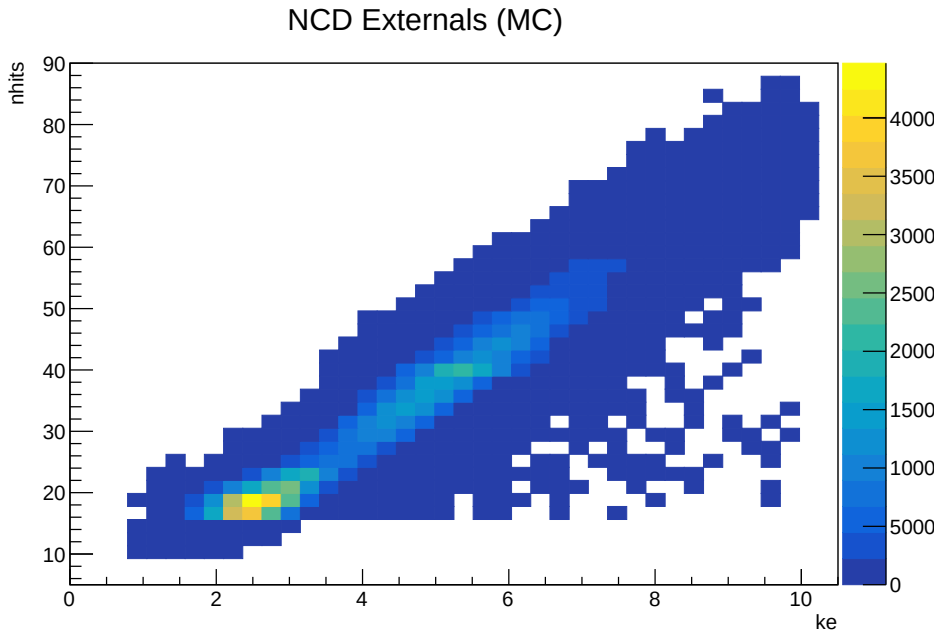

Figure 6.6: Monte Carlo simulation of the nhit distribution of external events during NCD phase as a function of reconstructed energy.

volume. As a proxy for this, we instead employed an nhit cut (at 24). Monte Carlo simulation of events in the external region during the NCD phase was used to determine the appropriate cut point (see Figure 6.6), and data from the internal sideband showed that there was no need to allow this cut to vary with time (see Figure 6.7). The data with this nhit selection applied are shown in Figure 6.8, with best fit results in Table 6.9. Additionally, the results were found to be robust to the particular nhit cut applied (see Table 6.10).

The internal sideband is defined by:

- 3.5 MeV $<$ E $<$ 5.5 MeV
- r $<$ 5.0 m
- all other cuts as in main analysis .

The data are handled in the same way described for the external sideband: binned by day and normalized to livetime. Plots of the results are shown in Figures 6.9 and 6.10, with the best fit results shown in Tables 6.11 and 6.12.

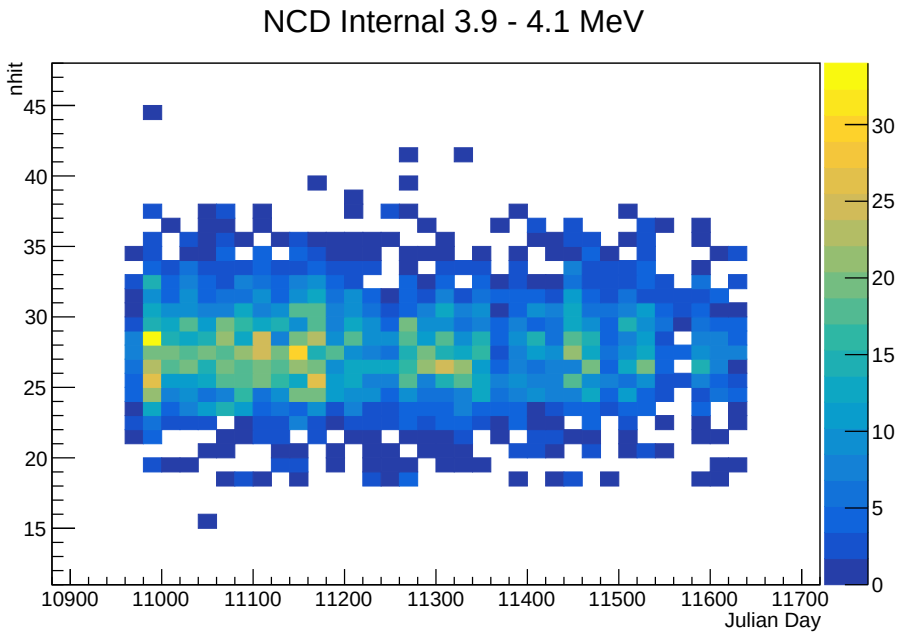

Figure 6.7: Nhit distribution of NCD internal events with energies reconstructing between 3.9 and 4.1 MeV as a function of time. Note that this remains quite stable over the length of the NCD phase.

This internal sideband is significantly enriched in the event type of interest, but it is still only roughly 50% internal radioactivity, with large contributions from externals, AV backgrounds, and solar neutrino events. Therefore, in order to set a meaningful limit on the contribution to variation coming from internal radioactivity, we fit the resulting data rates with a model that incorporated the expected background rates and the variation in solar event rates due to the eccentricity of the Earth's orbit. In this fit, the background levels were allowed to float according to equation (6.5), while the solar neutrino flux was fixed at the Standard Solar Model rate, unlike in the main analysis.

For the D2O and Salt phases, Monte Carlo data at low energies were available because of the low energy threshold analysis that was performed on these data. This allowed a comparison of the fitted background rate with the rate expected from external constraints, which is shown in Table 6.11. The agreement is very good given (i) the uncertainty on the background levels being used as a systematic uncertainty is significantly higher than the 8%

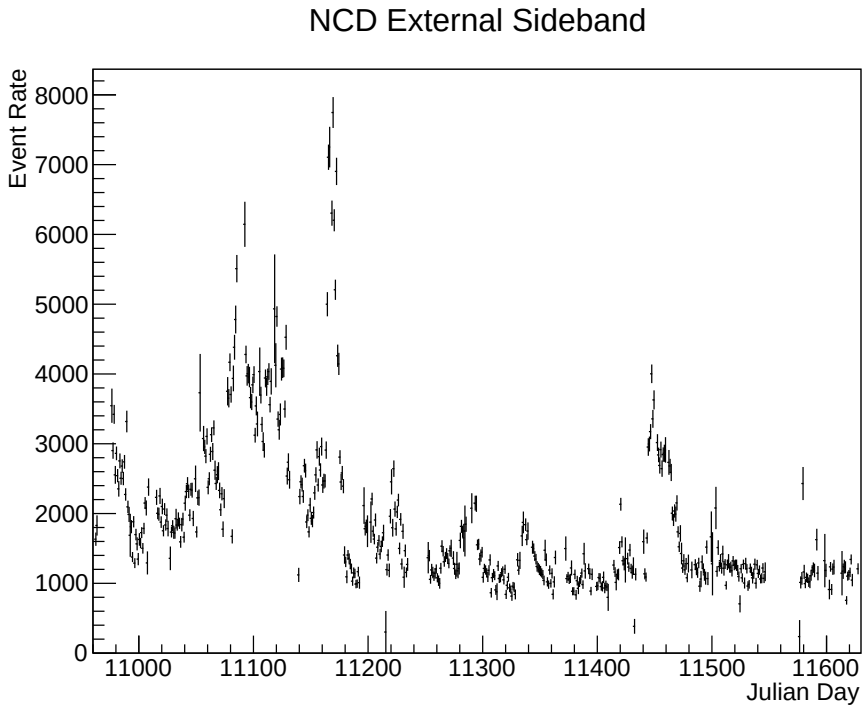

Figure 6.8: External Sideband, NCD phase

Mode	Best Fit
$\sin \omega t$	34.9 ± 0.3%
$\cos \omega t$	-49.4 ± 0.3%
$\sin 2\omega t$	3.7 ± 0.3%
$\cos 2\omega t$	7.5 ± 0.3%

Table 6.9: Best fit for variations in relevant Fourier modes for external background rates in NCD phase.

	Nhit Cut		
Mode	22	24	26
$\sin \omega t$	35.0	34.9	35.3
$\cos \omega t$	-49.2	-49.4	-49.7
$\sin 2\omega t$	3.6	3.7	3.5
$\cos 2\omega t$	7.1	7.5	7.3

Table 6.10: Fit results for variation in NCD phase light water backgrounds were robust to changes in the nhit cut threshold.

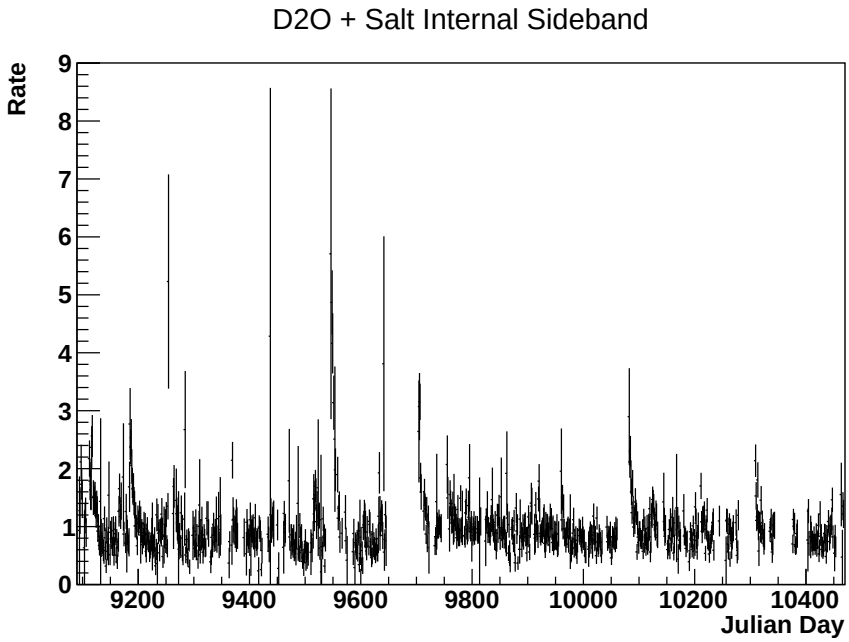

Figure 6.9: Internal Sideband for D2O and Salt phases

Mode	Background Variation	Background Normalization
$\sin\omega t$	0.9 ± 0.9%	91.9 ± 0.8%
$\cos\omega t$	-4.7 ± 0.9%	91.6 ± 0.9%
$\sin 2\omega t$	-5.8 ± 0.9%	91.5 ± 0.9%
$\cos 2\omega t$	3.9 ± 0.9%	91.7 ± 0.8%

Table 6.11: Best fit results for variations in the relevant Fourier modes for internal background rates in D2O and salt phases.

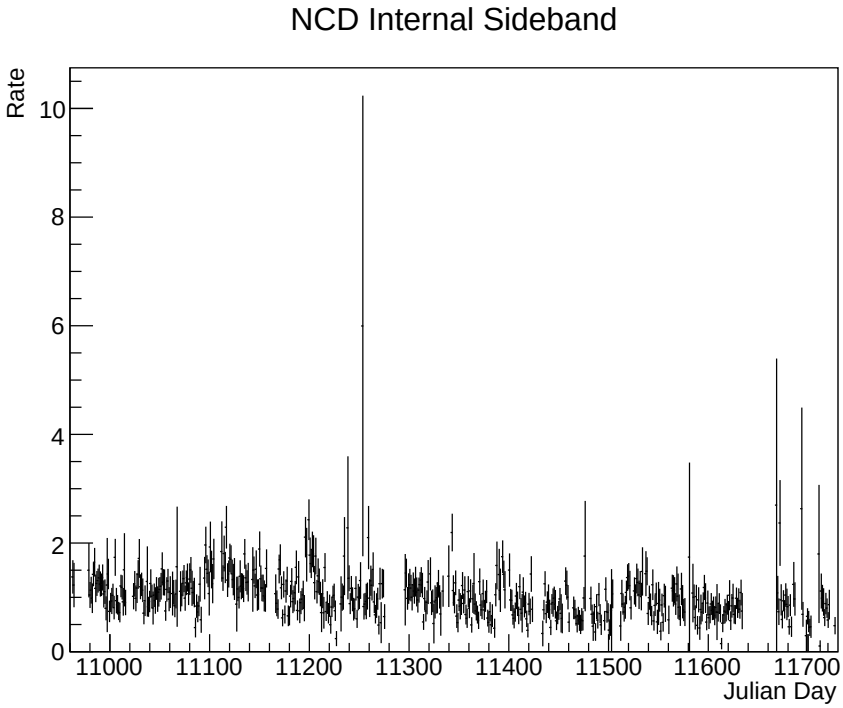

Figure 6.10: Internal Sideband for NCD phase

Mode	Best Fit
$\sin \omega t$	-9.2 $\pm$ 0.5%
$\cos \omega t$	-12.3 $\pm$ 0.5%
$\sin 2\omega t$	-12.5 $\pm$ 0.5%
$\cos 2\omega t$	-4.5 $\pm$ 0.5%

Table 6.12: Best fit results for variations in the relevant Fourier modes for internal background rates in NCD phase.

discrepancy observed, and (ii) the solar flux was not allowed to float. This estimate of the background levels is not independent of the previous external constraints, but it does serve as a useful cross-check that this analysis is consistent with previous work.

Among all the sidebands investigated, it is the external backgrounds during NCD phase that show the largest variation at annual frequencies. To ensure that these dramatic variations are covered in our systematic uncertainty, we take the power observed in that sideband, namely 50% (see Table 6.9), as our constraint. This figure was used in generating a fake data set to estimate the contribution to the uncertainty deriving from these variations. We found this effect to contribute an error 30% of the size of the statistical sensitivity of the measurement.

Background	Phase	Constraint	Uncertainty (E mode)	Uncertainty (E^2 mode)
Bi D2O	I	0.333	0.001	0.003
Tl D2O	I	0.467	0.001	0.003
Bi H2O	I	0.200	0.001	0.000
Tl H2O	I	0.333	0.001	0.000
AV n	I	0.267	0.001	0.003
Bi AV	I	1.000	0.001	0.000
Tl AV	I	1.000	0.001	0.000
Atm	I	0.167	0.001	0.003
Bi D2O	II	0.590	0.003	0.003
Tl D2O	II	0.577	0.003	0.003
Bi H2O	II	0.200	0.001	0.000
Tl H2O	II	0.272	0.001	0.003
AV n	II	0.345	0.003	0.003
Bi AV	II	1.000	0.002	0.003
Tl AV	II	1.000	0.002	0.003
Atm	II	0.167	0.001	0.003
Na24	II	0.250	0.001	0.003
Atm	III	0.200	0.001	0.000
Ext n	III	0.524	0.001	0.000
K5	III	0.167	0.001	0.000
K2	III	0.111	0.001	0.000
D2O pd	III	0.125	0.001	0.000
NCD pd	III	0.667	0.001	0.000
Ext n	IIIb	0.512	0.001	0.003
NCD pd	IIIb	0.333	0.000	0.000
K2	IIIb	0.151	0.001	0.000
K5	IIIb	0.087	0.001	0.000
D2O pd	IIIb	0.161	0.001	0.000
Atm	IIIb	0.214	0.001	0.000

Table 6.13: Estimated systematic uncertainties arising from unknown background normalizations. The constraint column shows the fractional uncertainty in the normalization of each source of background. The two uncertainty columns show the estimated contribution to the systematic uncertainty, expressed as a fraction of the expected statistical uncertainty, for the signals with linear and quadratic energy dependence. Phase IIIb refers to NCD backgrounds.

Source	Constraint	Uncertainty (E mode)	Uncertainty (E^2 mode)
E Scale (3 phases)	0.0041	0.004	0.006
E Scale (D2O)	0.0039	0.007	0.003
E Scale (Salt)	0.0034	0.008	0.003
E Scale (NCD)	0.0081	0.005	0.011
E Nonlinearity (3 phases)	0.0069	0.002	0.006
E Resolution (D2O)	0.041	0.006	0.003
E Resolution (e, Salt)	0.041	0.006	0.003
E Resolution (n, Salt)	0.018	0.006	0.003
β_{14} Scale (D2O)	0.0042	0.006	0.003
β_{14} Scale (e, Salt)	0.0024	0.006	0.003
β_{14} Scale (n, Salt)	0.0038	0.006	0.003
Direction Scale	0.12	0.006	0.003
n efficiency (ncd pmt)	0.028	0.006	0.003
n efficiency (ncd ncd)	0.024	0.006	0.003
Δm^2_{12}	0.024	0.007	0.003
Δm^2_{23}	0.036	0.007	0.003
Neutrino Hierarchy		0.006	0.003
Earth Matter Potential	0.1	0.006	0.003

Table 6.14: Estimated systematic uncertainties arising from unknown pdf shapes. The constraint column shows the 1 σ uncertainty in each parameter. (Expressions relating these parameters to the expected number of events are given in Appendix A.) The two uncertainty columns show the estimated systematic uncertainty, expressed as a fraction of the expected statistical uncertainty, for the signals with linear and quadratic energy dependence.

Source	Constraint	Uncertainty (ωt mode)	Uncertainty ($2\omega t$ mode)
Background time variation	0.5	0.255	0.255
Seasonal Day-Night effect		0.030	0.086

Table 6.15: Estimated systematic uncertainties arising from time variations. For the variation in the rate of background events, we have applied a 1 σ constraint corresponding to 50% variations, based on the sideband analyses described in section 6.5. The seasonal day-night effect was discussed in section 5.5. The two uncertainty columns show the estimated systematic uncertainty, expressed as a fraction of the expected statistical uncertainty, for signals with once annual and twice annual time dependence.

CHAPTER 7

RESULTS AND INTERPRETATION

As has already been discussed, we report our results as limits on the signals in each of the relevant Fourier modes, assuming that the others are zero. Each of these signals represents a linear combination of different effects (see Tables 5.2 and 7.3). In Table 7.1, we report the results of the fit for the solar mixing angle, the solar neutrino flux, and one Lorentz violating signal for each of the eight cases. Systematic uncertainties were computed by applying an ensemble of perturbed pdfs to the data and determining the variance of the fit results.

An example of one of the fits is shown in Figure 7.1. On the left are shown the data for the D2O and Salt phases; NCD data are on the right. The different panels show projections of the data and fit results along the axes of the different observables in the fit. The blue shaded area (blue points in the bottom panels) indicate the best fit values. The overall χ^2 (11943/8765, p = 0.01) is dominated by a single event appearing in an unlikely bin. Disregarding that bin, the fit agrees with the data with a reduced χ^2 of 1.02 (8905/8764, p = 0.30).

The large statistical fluctuations in the number of events observed on a day-by-day basis obscure the bottom panels, which show the ratio of the total number of events observed to the number expected in the best fit. The data are therefore rebinned over longer time periods and presented in Figure 7.2. The figure shows that the data are quite uniform and noise-like across all three phases of the experiment. The χ^2 residuals for a flat fit are shown in Table 7.2. There is a hint of short-term variation, particularly in the data binned at 5 day intervals, possibly due to changing background levels or detector conditions, but this washes out on seasonal time scales.

We can ask whether the results seem to be consistent with a normal distribution of mean 0 and variance 1; that is, whether the data are consistent with showing no evidence of Lorentz violations. Some of the results are correlated with one another; in particular, the three pairs of fits that differ only in energy dependence are likely to return quite similar

Mode	LV Signal	Solar Flux (10^6 cm^{-2}s^{-1})	Mixing Angle $\sin\theta_{12}$
E	$(7.0^{+7.2+5.9}_{-7.5-6.7})$ GeV^{-1}	$5.22 \pm 0.27^{+0.17}_{-0.22}$	$0.497\ ^{+0.088}_{-0.098}\pm 0.078$
$E\sin\omega t$	$(0.0^{+7.2+2.1}_{-7.3-2.2}) \times 10^{-1}$ GeV^{-1}	$5.15 \pm 0.26^{+0.14}_{-0.17}$	$0.577\ ^{+0.019+0.010}_{-0.018-0.009}$
$E\cos\omega t$	$(0.2^{+7.3+2.2}_{-7.4-2.3}) \times 10^{-1}$ GeV^{-1}	$5.15 \pm 0.26^{+0.14}_{-0.17}$	$0.577\ ^{+0.019+0.010}_{-0.018-0.009}$
E^2	$(3.0^{+3.3+2.7}_{-3.4-3.1}) \times 10^{2}$ GeV^{-2}	$5.22 \pm 0.27^{+0.17}_{-0.22}$	$0.537\ ^{+0.048+0.042}_{-0.049-0.037}$
$E^2\sin\omega t$	$(0.7^{+6.4+1.7}_{-6.5-1.8}) \times 10^{1}$ GeV^{-2}	$5.15 \pm 0.26^{+0.14}_{-0.17}$	$0.577\ ^{+0.019+0.011}_{-0.018-0.008}$
$E^2\cos\omega t$	$(-0.2^{+6.5}_{-6.6} \pm 1.9) \times 10^{1}$ GeV^{-2}	$5.15 \pm 0.26^{+0.14}_{-0.17}$	$0.577\ ^{+0.019+0.010}_{-0.018-0.009}$
$E^2\sin 2\omega t$	$(5.8^{+6.5+1.6}_{-6.4-1.8}) \times 10^{1}$ GeV^{-2}	$5.15 \pm 0.26^{+0.14}_{-0.17}$	$0.577\ ^{+0.019+0.010}_{-0.018-0.009}$
$E^2\cos 2\omega t$	$(-4.4^{+6.5+1.7}_{-6.6-1.8}) \times 10^{1}$ GeV^{-2}	$5.15 \pm 0.26^{+0.14}_{-0.17}$	$0.577\ ^{+0.019+0.010}_{-0.018-0.009}$

Table 7.1: Lorentz violation best fit results. The first error is statistical and the second systematic. The signals for each mode are expressed as combinations of the SNO coefficients, see Table 5.2. To obtain limits on the individual parameters, one must divide by a geometric factor from Table 5.2 and a weight coefficient from Table 7.3.

Binning Period	χ^2/ndf	p
5 days	390 / 340	0.07
10 days	203 / 188	0.23
30 days	68 / 66	0.44

Table 7.2: χ^2/ndf for the time residuals binned on different time scales. Although there is a hint of short-period changes to the total event rate, these effects average away on seasonal scales.

results. But because the data are sampled uniformly throughout the year to a reasonable approximation, we can treat the five results with different time dependences as independent. In this approximation, the results of the five c_{eff} fits have a chi-square test statistic relative to their statistical uncertainty of 2.06 (out of 5 degrees of freedom), which corresponds to the 84th percentile.

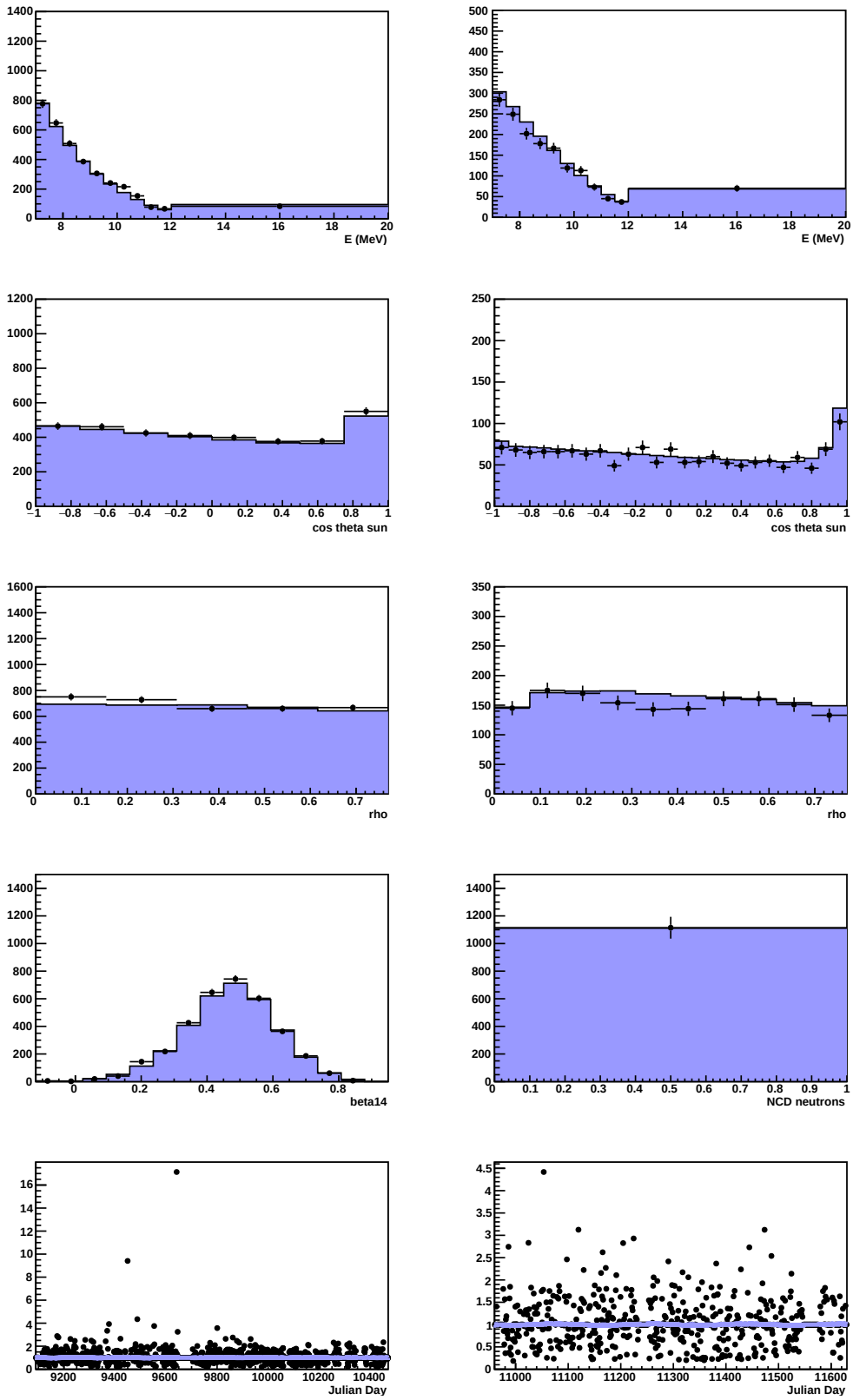

Figure 7.1: Fit for $E^2 \sin 2\omega t$ term

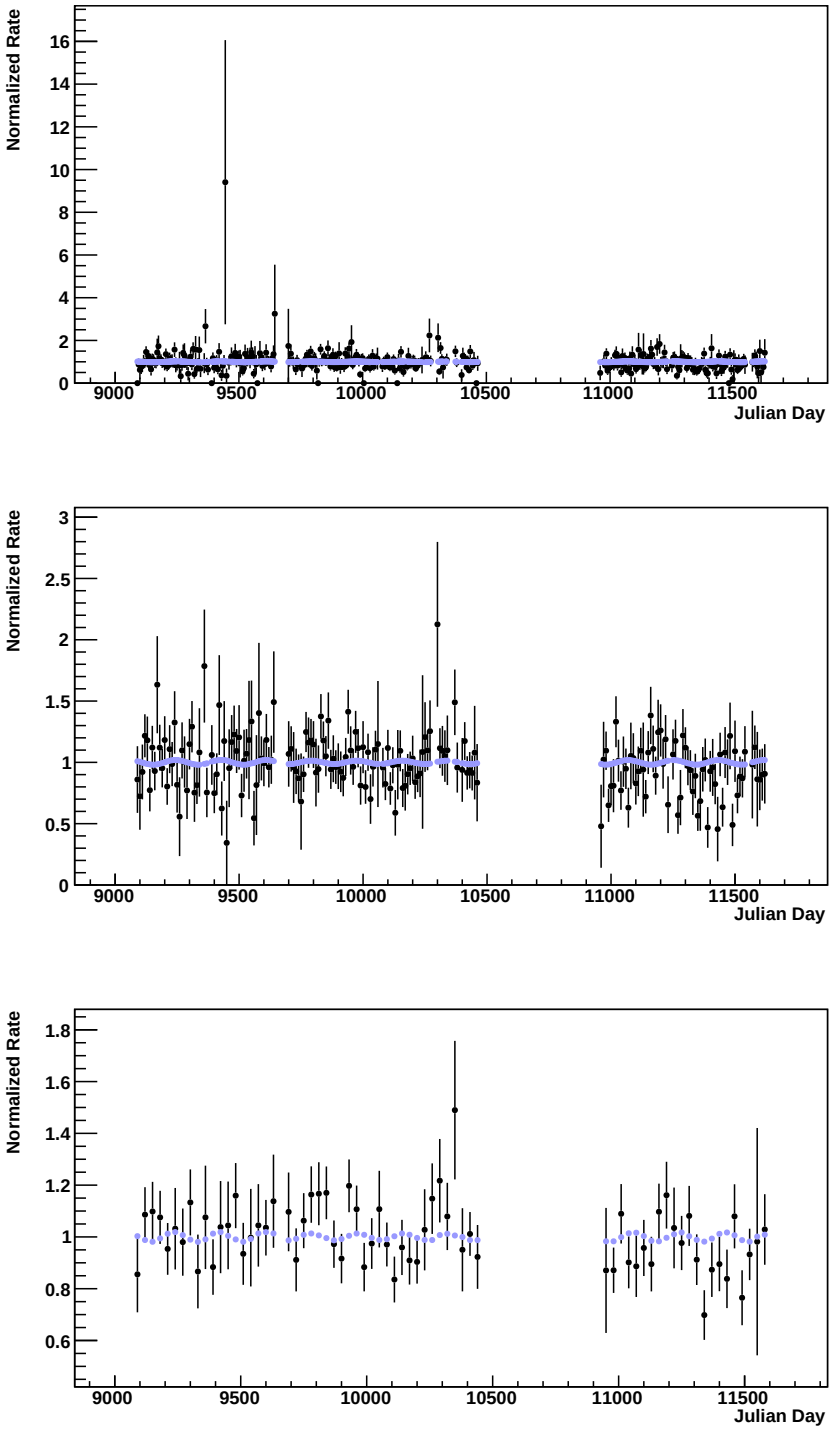

Figure 7.2: Time residuals of the $E^2 \sin 2\omega t$ fit, binned over 5 (top), 10 (middle), and 30 (bottom) day periods. The blue points indicate the shape of the signal for the best fit. This particular fit is selected so that the signal variation is visible. The signal fits at a level of 58 GeV^{-2}, roughly a 0.9σ effect, and the most significant of the eight fit results.

Flavor	Time fits	E	E^2
ee	0.289 ± 0.013 ± 0.044	0.230 ± 0.082 ± 0.038	0.261 ± 0.043 ± 0.042
eμ	-0.263 ± 0.047 ± 0.026	-0.427 ± 0.250 ± 0.045	-0.347 ± 0.138 ± 0.036
eτ	-0.393 ± 0.003 ± 0.098	-0.392 ± 0.005 ± 0.040	-0.394 ± 0.005 ± 0.039
$\mu\mu$	-0.232 ± 0.009 ± 0.038	-0.189 ± 0.059 ± 0.031	-0.212 ± 0.031 ± 0.035
$\mu\tau$	-0.257 ± 0.034 ± 0.045	-0.121 ± 0.196 ± 0.039	-0.189 ± 0.105 ± 0.042
$\tau\tau$	-0.057 ± 0.004 ± 0.007	-0.041 ± 0.023 ± 0.007	-0.042 ± 0.019 ± 0.014

Table 7.3: Estimates for the weight coefficients in units of 10^{-2} meV^{-2} (10^{22} GeV^{-2}). The first error comes from the uncertainty of the best fit result, the second error is systematic.

7.1 Comparison to Existing Limits

The most fundamental advantage to testing Lorentz symmetry in a new system is the ability to contribute a constraint on an independent linear combination of effects. In principle, with enough such measurements, one could rule out Lorentz violations in a way completely free from any assumptions. At present, the thicket of constraints is not sufficiently dense to enable such a meta-analysis, so we continue to report limits on individual coefficients assuming that the others are zero (and in this case also making the other assumptions already discussed, viz., small perturbation, g, H zero).

To set limits on the flavor components of the fields used in the SME, we must first compute the weight coefficients for our fits. These depend on the best fit for the mixing angle. Reference to Table 7.1 will show that there are only three cases to consider, because all of the fits with time-dependent signals returned identical central values and uncertainties for the solar mixing angle. The estimates for the weight parameters are shown in Table 7.3. For this purpose we have combined the weights known to control identical coefficients (due to the hermiticity of the Hamiltonian in flavor space).

The results in Table 7.3 can be combined with the limits in Table 7.1 to reach estimates for limits on the individual flavor components of the Lorentz violating operators. However, both the weights and the fit results share a number of systematic uncertainties, so to ensure the correct coverage, the limits we exhibit in Tables 7.4 - 7.6 were evaluated by calculating

the weights and the fit results simultaneously for an ensemble of systematically varied pdfs. This approach also ensures that the correlation between the Lorentz violation parameter and the solar mixing angle is handled correctly (although at roughly 2% it is a very small effect). As is usual, we assume that only one parameter contributes at a time.

Also shown in Tables 7.4 - 7.6 are the existing limits on the relevant Lorentz violating parameters. We are able to set limits on 40 operators that were previously unconstrained, and improve the existing limits on 15 additional parameters. This is one of the particular advantages of looking at solar neutrinos, which provide sensitivity to all flavor components simultaneously.

7.2 Natural Models

A major advantage of the SME framework is its categorization of all relevant effective operators, without recourse to a particular model for how these might be generated. This allows the experimentally measured constraints to be applied not just to one particular model but to any model anyone might wish to develop. However, this approach leaves one without a sense of whether a particular result has ruled out any well-motivated models. This is obviously a subjective question, but we will attempt to discuss this question in this section.

Probably the most straightforward estimate for the levels at which Lorentz violations might be expected comes from a dimensional argument, first made in reference [14]. The idea is that the new physics should be suppressed approximately in proportion to its natural energy scale, with the size of the effects given by $g\frac{m}{M}$, where g is a coupling constant, m is the electroweak scale (say 100 GeV), and M is the scale of the new physics. Assuming Lorentz violations stem from new physics at the Planck scale (say 10^{19} GeV), then we would expect a "natural" model to involve effects at the level of 10^{-17} for dimension 4 parameters and 10^{-19} GeV^{-1} for dimension 3 parameters. The question of where such a model loses its "naturalness" is entirely subjective, but one might argue roughly two orders of magnitude below these benchmarks.

Coefficient	This Work	Previous Limit	Reference
$\lvert a_{00}^{ee}\rvert$	8.8×10^{-20} GeV		
$\lvert a_{00}^{e\mu}\rvert$	9.8×10^{-20} GeV	9.2×10^{-20} GeV	[47]
$\lvert a_{00}^{e\tau}\rvert$	6.5×10^{-20} GeV	2.8×10^{-19} GeV [*]	[97]
$\lvert a_{00}^{\mu\mu}\rvert$	8.2×10^{-20} GeV	2.2×10^{-23} GeV [*]	[98]
$\lvert a_{00}^{\mu\tau}\rvert$	7.5×10^{-20} GeV	5.0×10^{-24} GeV [*]	[98]
$\lvert a_{00}^{\tau\tau}\rvert$	2.7×10^{-19} GeV	2.2×10^{-23} GeV [*]	[98]
$\lvert a_{10}^{ee}\rvert$	4.3×10^{-21} GeV		
$\lvert a_{10}^{e\mu}\rvert$	4.2×10^{-21} GeV	7.1×10^{-20} GeV	[47]
$\lvert a_{10}^{e\tau}\rvert$	2.8×10^{-21} GeV	5.5×10^{-19} GeV [*]	[97]
$\lvert a_{10}^{\mu\mu}\rvert$	5.4×10^{-21} GeV		
$\lvert a_{10}^{\mu\tau}\rvert$	5.1×10^{-21} GeV		
$\lvert a_{10}^{\tau\tau}\rvert$	2.0×10^{-20} GeV		
$\lvert\mathfrak{Re}(a_{11}^{ee})\rvert$	2.3×10^{-21} GeV		
$\lvert\mathfrak{Re}(a_{11}^{e\mu})\rvert$	2.2×10^{-21} GeV	8.1×10^{-20} GeV	[47]
$\lvert\mathfrak{Re}(a_{11}^{e\tau})\rvert$	1.5×10^{-21} GeV	1.3×10^{-19} GeV [*]	[97]
$\lvert\mathfrak{Re}(a_{11}^{\mu\mu})\rvert$	2.9×10^{-21} GeV	6.9×10^{-20} GeV [*]	[99]
$\lvert\mathfrak{Re}(a_{11}^{\mu\tau})\rvert$	2.8×10^{-21} GeV	8.8×10^{-23} GeV [*†]	[100]
$\lvert\mathfrak{Re}(a_{11}^{\tau\tau})\rvert$	1.1×10^{-20} GeV		
$\lvert\mathfrak{Im}(a_{11}^{ee})\rvert$	2.5×10^{-21} GeV		
$\lvert\mathfrak{Im}(a_{11}^{e\mu})\rvert$	2.5×10^{-21} GeV	8.5×10^{-20} GeV	[47]
$\lvert\mathfrak{Im}(a_{11}^{e\tau})\rvert$	1.7×10^{-21} GeV	1.3×10^{-19} GeV [*]	[97]
$\lvert\mathfrak{Im}(a_{11}^{\mu\mu})\rvert$	3.2×10^{-21} GeV	6.9×10^{-20} GeV [*]	[99]
$\lvert\mathfrak{Im}(a_{11}^{\mu\tau})\rvert$	3.1×10^{-21} GeV	8.8×10^{-23} GeV [*†]	[100]
$\lvert\mathfrak{Im}(a_{11}^{\tau\tau})\rvert$	1.2×10^{-20} GeV		

Table 7.4: Comparison to existing limits for a coefficients. All a's here are $a_{\text{eff}}^{(3)}$. All entries without a previous limit noted were not previously constrained. Entries marked [*] are technically set on the coefficient a_L, but for reasons discussed in section 3.3, these are probably good limits on a_{eff} as well. 95% CL limits are stated except for results marked † which are 3σ CL limits. Information collected from [44].

Coefficient	This Work	Previous Limit	Reference
$\lvert c_{00}^{ee}\rvert$	2.3×10^{-18}		
$\lvert c_{00}^{e\mu}\rvert$	2.5×10^{-18}	1.5×10^{-19}	[47]
$\lvert c_{00}^{e\tau}\rvert$	1.6×10^{-18}	1.4×10^{-16} [*]	[97]
$\lvert c_{00}^{\mu\mu}\rvert$	2.9×10^{-18}		
$\lvert c_{00}^{\mu\tau}\rvert$	2.7×10^{-18}		
$\lvert c_{00}^{\tau\tau}\rvert$	1.1×10^{-17}		
$\lvert c_{10}^{ee}\rvert$	3.9×10^{-19}		
$\lvert c_{10}^{e\mu}\rvert$	3.7×10^{-19}	1.2×10^{-19}	[47]
$\lvert c_{10}^{e\tau}\rvert$	2.5×10^{-19}		
$\lvert c_{10}^{\mu\mu}\rvert$	4.8×10^{-19}		
$\lvert c_{10}^{\mu\tau}\rvert$	4.5×10^{-19}		
$\lvert c_{10}^{\tau\tau}\rvert$	1.8×10^{-18}		
$\lvert\mathfrak{Re}(c_{11}^{ee})\rvert$	2.0×10^{-19}		
$\lvert\mathfrak{Re}(c_{11}^{e\mu})\rvert$	2.0×10^{-19}	1.3×10^{-19}	[47]
$\lvert\mathfrak{Re}(c_{11}^{e\tau})\rvert$	1.3×10^{-19}		
$\lvert\mathfrak{Re}(c_{11}^{\mu\mu})\rvert$	2.6×10^{-19}	1.3×10^{-20} [*]	[99]
$\lvert\mathfrak{Re}(c_{11}^{\mu\tau})\rvert$	2.5×10^{-19}	7.2×10^{-24} [*†]	[100]
$\lvert\mathfrak{Re}(c_{11}^{\tau\tau})\rvert$	9.8×10^{-19}		
$\lvert\mathfrak{Im}(c_{11}^{ee})\rvert$	2.2×10^{-19}		
$\lvert\mathfrak{Im}(c_{11}^{e\mu})\rvert$	2.2×10^{-19}	1.4×10^{-19}	[47]
$\lvert\mathfrak{Im}(c_{11}^{e\tau})\rvert$	1.5×10^{-19}		
$\lvert\mathfrak{Im}(c_{11}^{\mu\mu})\rvert$	2.8×10^{-19}	1.3×10^{-20} [*]	[99]
$\lvert\mathfrak{Im}(c_{11}^{\mu\tau})\rvert$	2.7×10^{-19}	1.3×10^{-22} [*†]	[100]
$\lvert\mathfrak{Im}(c_{11}^{\tau\tau})\rvert$	1.1×10^{-18}		

Table 7.5: Comparison to existing limits for c_{00}, c_{10}, and c_{11} coefficients. All c's here are $c_{\text{eff}}^{(4)}$. All entries without a previous limit noted were not previously constrained. Entries marked * are technically set on c_L, but for reasons discussed in section 3.3, we believe these to be applicable to c_{eff} as well. All results are stated at 95% CL except those marked † which are 3σ CLs. Data collected from [44].

Coefficient	This Work	Previous Limit	Reference
$\lvert c_{20}^{ee}\rvert$	1.1×10^{-18}		
$\lvert c_{20}^{e\mu}\rvert$	1.1×10^{-18}	2.0×10^{-19}	[47]
$\lvert c_{20}^{e\tau}\rvert$	7.4×10^{-19}	7.8×10^{-16} [*]	[97]
$\lvert c_{20}^{\mu\mu}\rvert$	1.4×10^{-18}		
$\lvert c_{20}^{\mu\tau}\rvert$	1.4×10^{-18}		
$\lvert c_{20}^{\tau\tau}\rvert$	5.4×10^{-18}		
$\lvert\mathfrak{Re}(c_{21}^{ee})\rvert$	6.1×10^{-19}		
$\lvert\mathfrak{Re}(c_{21}^{e\mu})\rvert$	6.1×10^{-19}	8.0×10^{-20}	[47]
$\lvert\mathfrak{Re}(c_{21}^{e\tau})\rvert$	4.0×10^{-19}		
$\lvert\mathfrak{Re}(c_{21}^{\mu\mu})\rvert$	7.7×10^{-19}	2.0×10^{-20} [*]	[99]
$\lvert\mathfrak{Re}(c_{21}^{\mu\tau})\rvert$	7.2×10^{-19}	4.5×10^{-24} [*†]	[100]
$\lvert\mathfrak{Re}(c_{21}^{\tau\tau})\rvert$	2.9×10^{-18}		
$\lvert\mathfrak{Im}(c_{21}^{ee})\rvert$	6.4×10^{-19}		
$\lvert\mathfrak{Im}(c_{21}^{e\mu})\rvert$	6.3×10^{-19}	8.5×10^{-20}	[47]
$\lvert\mathfrak{Im}(c_{21}^{e\tau})\rvert$	4.2×10^{-19}		
$\lvert\mathfrak{Im}(c_{21}^{\mu\mu})\rvert$	8.1×10^{-19}	2.0×10^{-20} [*]	[99]
$\lvert\mathfrak{Im}(c_{21}^{\mu\tau})\rvert$	7.7×10^{-19}	7.1×10^{-22} [*†]	[100]
$\lvert\mathfrak{Im}(c_{21}^{\tau\tau})\rvert$	3.1×10^{-18}		
$\lvert\mathfrak{Re}(c_{22}^{ee})\rvert$	2.5×10^{-19}		
$\lvert\mathfrak{Re}(c_{22}^{e\mu})\rvert$	2.4×10^{-19}	1.7×10^{-17}	[47]
$\lvert\mathfrak{Re}(c_{22}^{e\tau})\rvert$	1.6×10^{-19}	1.2×10^{-17} [*]	[97]
$\lvert\mathfrak{Re}(c_{22}^{\mu\mu})\rvert$	3.1×10^{-19}		
$\lvert\mathfrak{Re}(c_{22}^{\mu\tau})\rvert$	3.0×10^{-19}	7.8×10^{-24} [*†]	[100]
$\lvert\mathfrak{Re}(c_{22}^{\tau\tau})\rvert$	1.2×10^{-18}		
$\lvert\mathfrak{Im}(c_{22}^{ee})\rvert$	2.6×10^{-19}		
$\lvert\mathfrak{Im}(c_{22}^{e\mu})\rvert$	2.6×10^{-19}	1.7×10^{-17}	[47]
$\lvert\mathfrak{Im}(c_{22}^{e\tau})\rvert$	1.7×10^{-19}	1.2×10^{-17} [*]	[97]
$\lvert\mathfrak{Im}(c_{22}^{\mu\mu})\rvert$	3.3×10^{-19}		
$\lvert\mathfrak{Im}(c_{22}^{\mu\tau})\rvert$	3.1×10^{-19}	2.2×10^{-21} [*†]	[100]
$\lvert\mathfrak{Im}(c_{22}^{\tau\tau})\rvert$	1.2×10^{-18}		

Table 7.6: Comparison to existing limits for c_{20}, c_{21}, and c_{22} coefficients. All c's here are $c_{\text{eff}}^{(4)}$. All entries without a previous limit noted were not previously constrained. Entries marked * are technically limits set on c_L, but we believe these can be applied to c_{eff} for reasons discussed in section 3.3. All results are stated at 95% CL except those marked † which are stated at 3σ CLs. Data collected from [44].

Reaching this level of sensitivity does not rule out the possibility of Lorentz symmetry violations, of course. Besides a simple model with "unnaturally" small couplings, various models can be written to further suppress the level at which such effects would be expected. One such model category is known as countershaded models [101].

CHAPTER 8

CONCLUSION

In this dissertation, we described a search for violations of Lorentz symmetry in the neutrino sector using data from the SNO experiment. An understanding of the symmetries present in nature is critical to our understanding of both conservation laws and the kinds of models that might be useful in describing physical phenomena.

There is a long history of discovering violations of symmetries in particle physics, but in this case, no evidence of Lorentz symmetry violations was found in an analysis of the data from SNO. Limits on the size of any possible violations of Lorentz symmetry in the neutrino sector were established, 40 of them on operators previously unconstrained by experiment, and improved limits were set on an additional 15 parameters. This was made possible by the use of solar neutrinos, which undergo flavor changes in the Sun due to the matter effect. Since the limits are roughly at the level expected from new physics at the Planck scale, they should provide useful constraints on the possible kinds of beyond-Standard-Model physics that can be predicted by future theories.

APPENDIX A

IMPLEMENTATION OF SYSTEMATIC UNCERTAINTIES

In this appendix, we specify how we have implemented the various systematic shape perturbations to the pdfs. These follow the definitions used in reference [95], since we are using the same estimates of systematic uncertainty used there. The normalization uncertainties are applied by changing the number of events of each type expected. The time-related uncertainties are explained in the main text.

We summarize in Tables A.1 - A.5 the way in which we perturb the various observables when applying systematic corrections.

We have also allowed the mass squared differences, the mixing angles, and the matter potential of the Earth to vary. In each case, these perturbations were applied as a multiplicative change to the parameter of interest, e.g.,

$$\Delta m^{2\,\prime}_{12} = \Delta m^2_{12}(1 + \delta m_{12})\,. \tag{A.1}$$

Phase	Correction	Parameter	Name	Constraint
I	$\beta'_{14} = \beta_{14}(1 + b1)$	$b1$	β_{14} scale	0.0042
II	$\beta'_{14} = \beta_{14}(1 + b2_{e,n})$	$b2_e$	β_{14} scale (electrons)	0.0024
		$b2_n$	β_{14} scale (neutrons)	0.0038

Table A.1: Corrections to the β_{14} observable

Phase	Correction	Parameter	Name	Constraint
I	$E' = E(1 + e_{corr} + e1)$	e_{corr}	E Scale (3 phases)	0.0041
		$e1$	E Scale (D2O)	0.0039
II	$E' = E(1 + e_{corr} + e2)$	$e2$	E Scale (Salt)	0.0034
III	$E' = E(1 + e_{corr} + e3)$	$e3$	E Scale (NCD)	0.0081

Table A.2: Energy scale correction.

Phase	Correction	Parameter	Name	Constraint
I, II, III	$E'' = E' \left(1 + e_{nl} \frac{E - 5.05 \text{ MeV}}{13.95 \text{ MeV}}\right)$	e_{nl}	E Nonlinearity	0.0069

Table A.3: Energy nonlinearity correction, applied only to electron-type events.

Phase	Correction	Parameter	Name	Constraint
I	$E''' = E'' + \text{Gauss}(0, es1)$	$es1$	E Res. (D2O)	0.041
II	$E''' = E'' + \text{Gauss}(0, es2_{e,n})$	$es2_e$	E Res. (e, Salt)	0.041
		$es2_n$	E Res. (n, Salt)	0.018
III	$E''' = E'' + es3_e(E - E_{gen})$	$es3_e$	E Res. (e, NCD)	0.014
III	$E''' = E'' + es3_n(E - 5.646 \text{ MeV})$	$es3_n$	E Res. (n, NCD)	0.010

Table A.4: Energy resolution correction.

Phase	Correction	Parameter	Name	Constraint
I, II	$\cos\theta'_{\text{Sun}} = 1 + (1 + c1)(\cos\theta_{\text{Sun}} - 1)$	$c1$	Direction Scale	0.11
III	$\cos\theta'_{\text{Sun}} = 1 + (1 + c3)(\cos\theta_{\text{Sun}} - 1)$	$c3$	Direction Scale	0.12

Table A.5: Solar direction correction. If the corrected angle was outside the physical range of +1 to -1, it was replaced by a uniformy distributed random number from inside the physical range.

REFERENCES

[1] J. C. Maxwell. On physical lines of force. *Philosophical Magazine*, 90:11–23, 1861.

[2] A. A. Michelson and E. W. Morley. On the relative motion of the earth and the luminiferous ether. *Am. J. Sci.*, 34:333–345, 1887.

[3] J. Larmor. On a Dynamical Theory of the Electric and Luminiferous Medium, Part 3, Relations with material media. *Phil. Trans. Roy. Soc.*, 190:205–300, 1897.

[4] Henri Poincare. La theorie de Lorentz et le principe de reaction. *Archives neerlandaises des sciences exactes et naturelles*, 5:252–278, 1900.

[5] H. A. Lorentz. Electromagnetic phenomena in a system moving with any velocity smaller than that of light. *Proc. Acad. Sci. Amsterdam*, 6:809 – 831, 1904.

[6] A. Einstein. Zur elektrodynamik bewegter körper. *Ann. Phys.*, 17:891 – 921, 1905.

[7] Robert N. Cahn and Gerson Goldhaber. *The Experimental Foundations of Particle Physics*. Cambridge University Press, 1983.

[8] T. D. Lee and Chen-Ning Yang. Question of Parity Conservation in Weak Interactions. *Phys. Rev.*, 104:254–258, 1956.

[9] C. S. Wu, E. Ambler, R. W. Hayward, D. D. Hoppes, and R. P. Hudson. Experimental Test of Parity Conservation in Beta Decay. *Phys. Rev.*, 105:1413, 1957.

[10] J. H. Christenson, J. W. Cronin, V. L. Fitch, and R. Turlay. Evidence for the 2π Decay of the K_2^0 Meson. *Phys. Rev. Lett.*, 13:138, 1964.

[11] O. W. Greenberg. Cpt violation implies violation of lorentz invariance. *Phys. Rev. Lett.*, 89:231602, 2002.

[12] V. Alan Kostelecky. Gravity, Lorentz violation, and the standard model. *Phys. Rev.*, D69:105009, 2004.

[13] Don Colladay and V. Alan Kostelecky. CPT violation and the standard model. *Phys. Rev.*, D55:6760–6774, 1997.

[14] Don Colladay and V. Alan Kostelecky. Lorentz violating extension of the standard model. *Phys. Rev.*, D58:116002, 1998.

[15] Nick Jelley, Arthur B. McDonald, and R. G. Hamish Robertson. The Sudbury Neutrino Observatory. *Ann. Rev. Nucl. Part. Sci.*, 59:431–465, 2009.

[16] W. Pauli. On the earlier and more recent history of the neutrino. *Cambridge Monogr. Part. Phys. Nucl. Phys. Cosmol.*, 14:1–22, 2000.

[17] F. Reines et al. Detection of the free antineutrino. *Phys. Rev.*, 117:159 – 173, 1960.

[18] S. Schael et al. Precision electroweak measurements on the Z resonance. *Phys. Rept.*, 427:257–454, 2006.

[19] C. Patrignani and others (Particle Data Group). Review of particle physics. *Chinese Physics C*, 40:100001, 2016.

[20] Carlo Giunti and Chung W. Kim. *Fundamentals of Neutrino Physics and Astrophysics*. Oxford University Press, 2007.

[21] Kurt Riesselmann. The standard model of particle physics. *Symmetry*, 2015. https://www.symmetrymagazine.org/article/july-2015/standard-model.

[22] Ziro Maki, Masami Nakagawa, and Shoichi Sakata. Remarks on the unified model of elementary particles. *Progress of Theoretical Physics*, 28(5):870–880, 1962.

[23] B. Pontecorvo. Neutrino Experiments and the Problem of Conservation of Leptonic Charge. *Sov. Phys. JETP*, 26:984–988, 1968. [Zh. Eksp. Teor. Fiz.53,1717(1967)].

[24] J. J. Gomez-Cadenas, J. Martin-Albo, M. Mezzetto, F. Monrabal, and M. Sorel. The Search for neutrinoless double beta decay. *Riv. Nuovo Cim.*, 35:29–98, 2012.

[25] K. Abe et al. Solar Neutrino Measurements in Super-Kamiokande-IV. *Phys. Rev.*, D94(5):052010, 2016.

[26] A. Gando et al. Reactor On-Off Antineutrino Measurement with KamLAND. *Phys. Rev.*, D88(3):033001, 2013.

[27] F. P. An et al. New measurement of θ_{13} via neutron capture on hydrogen at Daya Bay. *Phys. Rev.*, D93(7):072011, 2016.

[28] Y. Abe et al. Measurement of $_{13}$ in Double Chooz using neutron captures on hydrogen with novel background rejection techniques. *JHEP*, 01:163, 2016.

[29] J. H. Choi et al. Observation of Energy and Baseline Dependent Reactor Antineutrino Disappearance in the RENO Experiment. *Phys. Rev. Lett.*, 116(21):211801, 2016.

[30] M. G. Aartsen et al. Measurement of the Atmospheric ν_e Spectrum with IceCube. *Phys. Rev.*, D91:122004, 2015.

[31] P. Adamson et al. First measurement of muon-neutrino disappearance in NOvA. *Phys. Rev.*, D93(5):051104, 2016.

[32] K. Abe et al. Precise Measurement of the Neutrino Mixing Parameter θ_{23} from Muon Neutrino Disappearance in an Off-Axis Beam. *Phys. Rev. Lett.*, 112(18):181801, 2014.

[33] P. Adamson et al. Combined analysis of ν_μ disappearance and $\nu_\mu \to \nu_e$ appearance in MINOS using accelerator and atmospheric neutrinos. *Phys. Rev. Lett.*, 112:191801, 2014.

[34] F. Capozzi, E. Lisi, A. Marrone, D. Montanino, and A. Palazzo. Neutrino masses and mixings: Status of known and unknown 3ν parameters. *Nucl. Phys.*, B908:218–234, 2016.

[35] B. Aharmim et al. A Search for Neutrinos from the Solar hep Reaction and the Diffuse Supernova Neutrino Background with the Sudbury Neutrino Observatory. *Astrophys. J.*, 653:1545–1551, 2006.

[36] V. Castellani, S. Degl'Innocenti, G. Fiorentini, M. Lissia, and B. Ricci. Solar neutrinos: Beyond standard solar models. *Phys. Rept.*, 281:309–398, 1997.

[37] John N. Bahcall, Aldo M. Serenelli, and Sarbani Basu. New solar opacities, abundances, helioseismology, and neutrino fluxes. *Astrophys. J.*, 621:L85–L88, 2005.

[38] Borexino Collaboration. Neutrinos from the primary proton-proton fusion process in the Sun. *Science*, 512:383–386, 2014.

[39] L. Wolfenstein. Neutrino Oscillations in Matter. *Phys Rev D*, 17:2369–2374, 1978.

[40] S. P. Mikheyev and A. Y. Smirnov. Resonant Amplification of ν Oscillations in Matter and Solar-Neutrino Spectroscopy. *Nuovo Cimento C*, 9:17–26, 1986.

[41] Paul Langacker and Jiang Liu. Standard Model contributions to the neutrino index of refraction in the early universe. *Phys. Rev.*, D46:4140–4160, 1992.

[42] J. D. Tasson. What do we know about lorentz invariance? *Rep. Prog. Phys.*, 77:062901, 2014.

[43] Robert DiSalle. Space and time: Inertial frames. In Edward N. Zalta, editor, *The Stanford Encyclopedia of Philosophy*. Metaphysics Research Lab, Stanford University, winter 2016 edition, 2016.

[44] V. Alan Kostelecky and Neil Russell. Data Tables for Lorentz and CPT Violation. *Rev. Mod. Phys.*, 83:11–31, 2011.

[45] Robert Bluhm, V. Alan Kostelecky, Charles D. Lane, and Neil Russell. Probing Lorentz and CPT violation with space based experiments. *Phys. Rev.*, D68:125008, 2003.

[46] V. Alan Kostelecky and Matthew Mewes. Lorentz and CPT violation in neutrinos. *Phys. Rev.*, D69:016005, 2004.

[47] Alan Kostelecky and Matthew Mewes. Neutrinos with Lorentz-violating operators of arbitrary dimension. *Phys. Rev.*, D85:096005, 2012.

[48] Jonah Bernhard. Lorentz-violation in solar-neutrino oscillations. 2011.

[49] Jorge S. Diaz, V. Alan Kostelecky, and Matthew Mewes. Perturbative Lorentz and CPT violation for neutrino and antineutrino oscillations. *Phys. Rev.*, D80:076007, 2009.

[50] Raymond Davis, Jr., Don S. Harmer, and Kenneth C. Hoffman. Search for neutrinos from the sun. *Phys. Rev. Lett.*, 20:1205–1209, 1968.

[51] John N. Bahcall, Neta A. Bahcall, and G. Shaviv. Present status of the theoretical predictions for the Cl-36 solar neutrino experiment. *Phys. Rev. Lett.*, 20:1209–1212, 1968.

[52] B. T. Cleveland et al. Measurement of the solar electron neutrino flux with the homestake chlorine detector. *Astrophys. J.*, 496:505 – 526, 1998.

[53] John N. Bahcall, M. H. Pinsonneault, and G. J. Wasserburg. Solar models with helium and heavy-element diffusion. *Rev. Mod. Phys.*, 67:781–808, Oct 1995.

[54] R. T. Rood. Review of non-standard models. *Proceedings of an Informal Conference on the Status and Future of Solar Neutrino Research, Upton, NY*, 1978.

[55] V. A. Lubimov et al. An Estimate of the ν_e mass from the β-spectrum of tritium in the valine molecule. *Phys Lett B*, 94:266, 1980.

[56] K. S. Hirata et al. Results from one thousand days of real-time, directional solar-neutrino data. *Phys. Rev. Lett.*, 65:1297–1300, Sep 1990.

[57] J. N. Abdurashitov et al. Results from SAGE. *Phys Lett B*, 328:234, 1994.

[58] GALLEX Collaboration. First results from the ^{51}Cr neutrino source experiment with the GALLEX detector. *Phys Lett B*, 342:440, 1995.

[59] Herbert H. Chen. Direct Approach to Resolve the Solar-Neutrino Problem. *Phys. Rev. Lett.*, 55:1534–1536, 1985.

[60] E. Pasierb, H. S. Gurr, J. Lathrop, F. Reines, and Sobel H. W. Detection of Weak Neutral Current Using Fission $\bar{\nu}_e$ on Deuterons. *Phys. Rev. Lett.*, 43:96–99, 1979.

[61] J. Boger et al. The Sudbury neutrino observatory. *Nucl. Instrum. Meth.*, A449:172–207, 2000.

[62] G. Doucas, N. A. Jelley, M. E. Moorhead, N. W. Tanner, S. Gil, L. McGarry, and C. E. Waltham. Light concentrators for the Sudbury Neutrino Observatory. *Nucl. Instrum. Meth.*, A370:579–596, 1996.

[63] H. Lee, R. Komar, S. Piechocinski, and H. B. Mak. Report on Magnetic Field Compensation Coil Calculations. *SNO-STR-91-61*, 1991.

[64] M. R. Dragowsky et al. The N-16 calibration source for the Sudbury Neutrino Observatory. *Nucl. Instrum. Meth.*, A481:284–296, 2002.

[65] N. J. Tagg, A. Hamer, B. Sur, E. D. Earle, R. L. Helmer, G. Jonkmans, B. A. Moffat, and J. J. Simpson. The Li-8 calibration source for the Sudbury Neutrino Observatory. *Nucl. Instrum. Meth.*, A489:178–188, 2002.

[66] Alan W. P. Poon, R. J. Komar, C. E. Waltham, M. C. Browne, R. G. H. Roberston, N. P. Kherani, and H. B. Mak. A Compact H-3(p,gamma)He-4 19.8-MeV gamma-ray source for energy calibration at the Sudbury Neutrino Observatory. *Nucl. Instrum. Meth.*, A452:115–129, 2000.

[67] J. J. Simpson. The Strength of the Strong Cf-Source and the Efficiency for Detecting Neutrons. *SNO-STR-2001-002*, 2001.

[68] B. A. Moffat, R. J. Ford, F. A. Duncan, K. Graham, A. L. Hallin, C. A. W. Hearns, J. Maneira, P. Skensved, and D. R. Grant. Optical calibration hardware for the sudbury neutrino observatory. *Nucl. Instrum. Meth.*, A554:255–265, 2005.

[69] Bryce Anton Moffat. The Optical Calibration of the Sudbury Neutrino Observatory. 2001.

[70] T. C. Andersen et al. A Radium assay technique using hydrous titanium oxide adsorbent for the Sudbury Neutrino Observatory. *Nucl. Instrum. Meth.*, A501:386–398, 2003.

[71] John F. Amsbaugh et al. An Array of low-background He-3 proportional counters for the Sudbury neutrino observatory. *Nucl. Instrum. Meth.*, A579:1054–1080, 2007.

[72] W. Ralph Nelson, H. Hirayama, and David W. O. Rogers. The Egs4 Code System. 1985.

[73] Judith F. Briesmeister. MCNP: A General Monte Carlo N-Particle Transport Code. 1993.

[74] A. E. G. Ingelman and J. Rathsman. LEPTO version 6.3 - The Lund Monte Carlo for Deep Inelastic Lepton-Nucleon Scattering. 1995.

[75] P. A. Aarnio, A. Fasso, G. R. Stevenson, J. M. Zazula, A. Ferrari, P. R. Sala, H. J. Mohring, and J. Ranft. FLUKA: Hadronic benchmarks and applications. In *International Conference on Monte Carlo Simulation in High-Energy and Nuclear Physics - MC 93 Tallahassee, Florida, February 22-26, 1993*, pages 88–99, 1993.

[76] C. Zeitnitz and T. A. Gabriel. The GEANT - CALOR interface and benchmark calculations of ZEUS test calorimeters. *Nucl. Instrum. Meth.*, A349:106–111, 1994.

[77] Stanley Reid Seibert. A Low Energy Measurement of the 8B Solar Neutrino Spectrum at the Sudbury Neutrino Observatory. 2008.

[78] Jorge S. Diaz and Alan Kostelecky. Lorentz- and CPT-violating models for neutrino oscillations. *Phys. Rev.*, D85:016013, 2012.

[79] S. S. Aleshin, O. G. Kharlanov, and A. E. Lobanov. Analytical treatment of long-term observations of the day-night asymmetry for solar neutrinos. *Phys. Rev.*, D87(4):045025, 2013.

[80] A. M. Dziewonski and D. L. Anderson. Preliminary reference earth model. *Phys. Earth Planet. Interiors*, 25:297–356, 1981.

[81] Oleg G. Kharlanov. Peculiar seasonal effects in the neutrino day-night asymmetry. 2015.

[82] P. K. Seidelmann. *Explanatory Supplement to the Astronomical Almanac*. University Science Books, 1992.

[83] Glen Cowan. *Statistical Data Analysis*. Oxford University Press, 1998.

[84] F. James and M. Roos. Minuit: A System for Function Minimization and Analysis of the Parameter Errors and Correlations. *Comput. Phys. Commun.*, 10:343–367, 1975.

[85] B. Aharmim et al. Combined Analysis of all Three Phases of Solar Neutrino Data from the Sudbury Neutrino Observatory. *Phys. Rev.*, C88:025501, 2013.

[86] B. Aharmim et al. Low Energy Threshold Analysis of the Phase I and Phase II Data Sets of the Sudbury Neutrino Observatory. *Phys. Rev.*, C81:055504, 2010.

[87] B. Aharmim et al. Measurement of the ν_e and Total ^{8}B Solar Neutrino Fluxes with the Sudbury Neutrino Observatory Phase-III Data Set. *Phys. Rev.*, C87(1):015502, 2013.

[88] Josh Klein and Mark Neubauer. Using Time and Angle Information in Reconstruction and the SNOMAN Path Fitter. *SNO-STR-2000-022*, 2001.

[89] Pierre-Luc Drouin. FTN: A Time Fitter for the NCD Phase. 2008.

[90] Tom Andersen et al. Snoman companion 5.03. 2002.

[91] LETA WG. Low Energy Threshold Analysis Unidoc. 2014.

[92] Joshua R. Klein. Tuning the High Level Cuts for LETA. *Technical Report, University of Texas*, 2006.

[93] Q. R. Ahmad et al. Direct evidence for neutrino flavor transformation from neutral current interactions in the Sudbury Neutrino Observatory. *Phys. Rev. Lett.*, 89:011301, 2002.

[94] B. Aharmim et al. Electron energy spectra, fluxes, and day-night asymmetries of B-8 solar neutrinos from measurements with NaCl dissolved in the heavy-water detector at the Sudbury Neutrino Observatory. *Phys. Rev.*, C72:055502, 2005.

[95] Pierre-Luc Drouin. Three-Phase Extraction of the Electron Neutrino Survival Probability at the Sudbury Neutrino Observatory. 2011.

[96] M. Honda, M. Sajjad Athar, T. Kajita, K. Kasahara, and S. Midorikawa. Atmospheric neutrino flux calculation using the NRLMSISE-00 atmospheric model. *Phys. Rev.*, D92(2):023004, 2015.

[97] Teppei Katori and Joshua Spitz. Testing Lorentz Symmetry with the Double Chooz Experiment. In *Proceedings, 6th Meeting on CPT and Lorentz Symmetry (CPT 13): Bloomington, Indiana, USA, June 17-21, 2013*, pages 9–12, 2014.

[98] Jorge S. Diaz. Correspondence between nonstandard interactions and CPT violation in neutrino oscillations. 2015.

[99] B. Quilain. Results of Lorentz- and CPT-Invariance Violation at T2K and Future Perspectives. In *Proceedings, 7th Meeting on CPT and Lorentz Symmetry (CPT 16): Bloomington, Indiana, USA, June 20-24, 2016*, pages 125–128, 2017.

[100] P. Adamson et al. Search for Lorentz invariance and CPT violation with muon antineutrinos in the MINOS Near Detector. *Phys. Rev.*, D85:031101, 2012.

[101] Jorge S. Diaz, Alan Kostelecky, and Ralf Lehnert. Relativity violations and beta decay. *Phys. Rev.*, D88(7):071902, 2013.